



Simulation and measurement of condensation and mixing effects in steam ejectors

A thesis submitted in fulfilment of the requirements of the degree of

Doctor of Philosophy

Submitted by

Kavous Ariafar

2016

Abstract

Vapour compression via ejectors has become a topic of interest for researchers in the field of air conditioning and refrigeration. Ejectors have the benefit of being extremely reliable with stable operation and no moving parts leading to essentially maintenance free operation. However, these devices typically have very low efficiencies due to the low entrained mass flow rate of the low pressure secondary stream relative to the high pressure primary stream mass flow rate. The entrainment of the secondary stream and mixing between the primary and secondary streams are therefore dominant features which require investigation. Entrainment and mixing typically occurs under conditions of compressible, turbulent flow with strong pressure gradients. Steam ejectors, which are the focus of the present work, have the added complexity of condensation effects which must be accommodated in modelling and simulation work. Condensation in the primary nozzle of steam ejectors alters the steam flow properties relative to properties derived from ideal gas modelling, which is sometimes used for steam ejector analysis work. By performing computational simulations for non-equilibrium wet steam flow in a representative primary nozzle, the altered steam jet properties that arise during the nozzle expansion process are demonstrated, via empirical correlations, to be of sufficient magnitude to affect the mixing rate, and thus the entrainment ratio, of steam ejectors. For the particular primary nozzle and flow conditions considered, it was estimated that these changes in steam properties would cause around 29% increase in the mixing layer growth rate for the wet steam case relative to the ideal gas case. To further explore the influence of wet steam mixing effects, the non-equilibrium wet steam computational simulation approach was then expanded to the case of a complete ejector. Under particular conditions for the choked flow ejector operation, results indicated that the non-equilibrium wet steam model simulates an entrainment ratio that is 10% higher than that for the ideal gas model. The non-equilibrium wet steam model also gives a higher critical back pressure by about 7% relative to the ideal gas model. Enhanced mixing layer growth, which arises due to steam condensation in the primary nozzle, was identified as the main reason for higher entrainment ratio of

the ejector simulations using the wet steam model. Higher pitot pressure of the mixture at the diffuser entrance for the wet steam simulation was also identified as the reason for higher critical back pressure for the ejector relative to the case of ideal gas simulation.

To estimate the relative significance of pressure-driven effects and mixing-driven effects on the secondary stream entrainment, ideal gas computational simulations were also performed. Under a fixed operating condition for the primary and discharge streams, the ejector entrainment ratio was more strongly influenced by the mixing effects at lower secondary pressure. For a particular ejector and associated operating conditions, about 35% of the ejector entrainment ratio was attributable to mixing effects when the secondary stream pressure lift ratio was 4.5, while this portion was reduced to about 22% when the secondary stream pressure lift ratio was 1.6. Given the significance of ejector mixing effects and the lack of consensus on the most appropriate model for turbulent mixing in steam ejectors, an experimental investigation was performed to provide direct data on the mixing of wet steam jets in steam ejectors for model development and validation of computational simulations. Pitot and cone-static pressures within a high pressure supersonic steam jet that mixed with low pressure co-flowing steam were obtained. Results from the non-equilibrium wet steam simulations were analysed to give values of pitot pressure and cone-static pressure values using both equilibrium and frozen-composition gas dynamic models. The equilibrium analysis appeared reasonable for the pitot pressure, whereas the frozen-composition analysis was a better approximation for the cone-static pressure. Differences between the experimental data and the wet steam computational simulations were in the vicinity of 25% at certain locations. The static pressures downstream of the nozzle exit were lower than the triple point, but energy exchanges associated with the transitions to and from the solid phase were not incorporated in the wet steam model. The development of such a model is required before definitive conclusions can be made regarding the accuracy of the turbulence modelling.

Certification of Dissertation

This thesis is entirely the work of *Kavous Ariafar* except where otherwise acknowledged. The work is original and has not previously been submitted for any other award, except where acknowledged.

Student and supervisors signatures of endorsement are held at USQ.

Acknowledgements

I would like to express my deepest gratitude to the following,

My Almighty God, for giving me good health, courage, knowledge and strength to complete my PhD study.

Professor David Buttsworth, my principal supervisor, for giving me the opportunity to do a PhD at the University of Southern Queensland. I owe him an unbelievable amount of gratitude for his patient guidance, encouragement and advice all throughout these years.

Dr Ray Malpress, my associate supervisor, who helped me a lot for the experimental part of this research study. His valuable comments and suggestions were essential in improving the quality of this research.

I have been extremely lucky to have such supervisors who cared so much about my work, and who responded to my questions and queries so promptly. They were always available and ready to help.

Dr Navid Sharifi and Mr Thomas Cochrane who generously shared their expertise which undoubtedly reduced the time I required to complete several tasks.

The staff in the USQ workshop who gave me good technical support, especially Mr Oliver Kinder, Mr Chris Galligan, and Mr Brett Richards.

My family and friends for their understanding, encouragement, and moral support that made me achieve this success.

Kavous Ariaifar

Statements of Contributions

The following paragraphs describe the relative contributions of the co-authors in the publications presented in this thesis.

- Ariafar, K., Buttsworth, D., Sharifi, N. and R. Malpress, *Ejector primary nozzle steam condensation: Area ratio effects and mixing layer development*. Applied Thermal Engineering, 2014. 71(1): p. 519-527.

Total overall contribution for this paper is KA 70%, DB 10%, NS 10% and RM 10%.

- Ariafar, K., Buttsworth, D., Al-Doori, G. and R. Malpress, *Effect of mixing on the performance of wet steam ejectors*. Energy, 2015. 93: p. 2030-2041.

Total overall contribution for this paper is KA 70%, DB 10%, GA 10% and RM 10%.

- Ariafar, K., Buttsworth, D., Al-Doori, G. and N. Sharifi, *Mixing layer effects on the entrainment ratio in steam ejectors through ideal gas computational simulations*. Energy, 2016. 95: p. 380-392.

Total overall contribution for this paper is KA 65%, DB 20%, GA 10% and NS 5%.

- Ariafar, K., Cochrane, T., Malpress, R. and D. Buttsworth, *Pitot and static pressure measurements in a co-flowing steam jet*. Prepared for submission.

Total overall contribution for this work is KA 70%, TC 10% RM 10% and DB 10%.

Table of Contents

Abstract.....	i
Certification of Dissertation.....	iii
Acknowledgements.....	iv
Statements of Contributions.....	v
Chapter 1 Introduction	1
1.1 Steam ejectors	1
1.1.1 Theory and applications.....	1
1.1.2 Steam condensation in the primary nozzle	6
1.1.3 Mixing layer development in the mixing chamber	9
1.2 Objectives of the dissertation	9
1.3 Overview of the dissertation.....	10
1.3.1 Chapter 2 Literature review	11
1.3.2 Chapter 3 Flow characteristics in the primary nozzle.....	11
1.3.3 Chapter 4 Effect of steam condensation of the ejector performance.....	12
1.3.4 Chapter 5 Effects of mixing on the ejector entrainment ratio	12
1.3.5 Chapter 6 Pitot and static pressure measurements in a co-flowing steam jet.....	12
1.3.6 Chapter 7 Conclusion	13
Chapter 2 Literature review.....	14
2.1 Steam ejector studies	14
2.1.1 Analytical works	14
2.1.2 Experimental works	17
2.2 Computational simulations of steam ejectors	23
2.2.1 Ideal gas simulations.....	24
2.2.2 Wet steam simulations	29
2.3 Steam nucleation theory in Laval nozzles	31
2.4 Steam condensation in turbines	32
2.5 Mixing layer and jet mixing studies	33
2.6 Conclusion.....	36
Chapter 3 Flow characteristics in the primary nozzle.....	39
Chapter 4 Effect of steam condensation on the ejector performance.....	45
Chapter 5 Effects of mixing on the ejector entrainment ratio	58
Chapter 6 Pitot and static pressure measurements in a co-flowing steam jet.....	72

Chapter 7 Conclusions	103
7.1 Summary	103
7.2 Effect of steam condensation on flow characteristics in the primary nozzle and mixing process	104
7.3 Effects of steam condensation on the ejector performance	104
7.4 Effect of mixing layer development of the ejector entrainment ratio	105
7.5 Measurement of steam mixing in a co-flowing steam jet	106
7.6 Areas for Future Research	107
References	108
Appendix A	113
A.1 Nozzle end plate	113
A.2 Exit end plate	115
A.3 Probes system.....	117

List of Figures

Figure 1-1: Schematic of a steam ejector refrigeration cycle.....	2
Figure 1-2: Schematic of steam ejector cycle in T-S diagram	3
Figure 1-3: Typical ejector cross-section illustrating the different zones.....	3
Figure 1-4: Illustrative performance characteristics of a steam ejector.....	6
Figure 1-5: Steam condensation in the primary nozzle with axial pressure distribution	8
Figure 1-6: h-s diagram of steam condensation in the primary nozzle	8
Figure 1-7: Schematic of the mixing layer development at the primary nozzle exit	9
Figure 2-1: Primary nozzle geometries used by Chang and Chen [26]	20
Figure 2-2: Configuration of the steam ejector designed by Ma et al. [16]	22
Figure 2-3: Different mixing chamber configuration used by Aphornratana et al. [34]; (a) constant area inlet, (b) convergent inlet.....	23
Figure 2-4: Contours of Mach number in the steam ejector [38].....	25
Figure 2-5: Effective area occurring in the ejector throat [39].....	25
Figure 2-6: Design concept for a lobed nozzle in order to increase the mixing process [49].....	28

Chapter 1 Introduction

1.1 Steam ejectors

1.1.1 Theory and applications

Supersonic steam ejectors are widely used in a large number of industries that require steam for heating or for a power-generating working fluid and are extensively used in power generation, nuclear, chemical processing industries, distillation, vacuum evaporation and drying (for instance, soap drying). They can be fabricated in wide range of sizes and can operate safely under hazardous conditions [1].

Ejectors are devices which utilize the energy of a high pressure fluid (known as the primary stream) to move a low pressure fluid (the secondary stream) and enable it to be compressed to a higher pressure. The action of ejectors is similar to a vacuum pump or compressor but ejectors do not use any moving components or electricity. They are known for simple construction, easy installation and low capital costs. Recently, ejectors have become of interest for researchers in air conditioning and refrigeration fields.

Figure 1-1 shows a block diagram of an ejector-based refrigeration system. Through comparison to a typical vapour-compression refrigeration cycle, it can be seen that the ejector, steam generator and pump are used to replace the compressor. Replacing one component (the compressor) in a vapour-compression cycle with three components (the ejector, pump and steam generator) in an ejector-based cycle appears to increase complexity. However, energy savings are possible if an otherwise wasted source of heat is used in the steam generator. Also, a pump working on the liquid phase (as in the case of the ejector cycle) requires substantially less energy to operate than a compressor working on the vapour phase (as in the case of the vapour-compression refrigeration cycle).

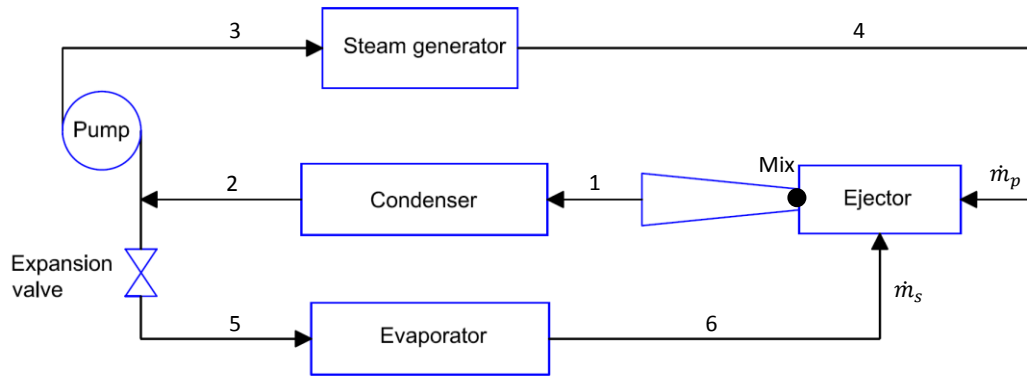


Figure 1-1: Schematic of a steam ejector refrigeration cycle

Cooling and heating systems typically use natural refrigerant fluids or artificial working fluids which can cause serious problems like depletion of the stratospheric ozone layer, production of large amounts of greenhouse gas emissions and global warming. Furthermore, refrigeration and air conditioning systems are normally driven by electricity, which increases the demand for electricity and the consumption of fossil fuel. An alternative solution for this problem is the application of low-grade waste energy or solar energy. There are a number of types of air conditioning systems potentially powered by such energy including absorption, adsorption and desiccant coolers. However, these systems are typically large and expensive. Evaporative coolers are another possibility but these have a high level of water consumption and may not be effective for all locations. Ejectors can also be driven by waste-energy or solar power and through an increasing use of waste or solar energy in refrigeration systems, the relative demand for electrical energy sources can be decreased.

Figure 1-2 shows T-S diagram of a steam ejector refrigeration cycle. Thermal power which is supplied at high pressure to the steam generator by the highest temperature thermal source, is partially converted into work to provide thermal power to the intermediate temperature thermal source throughout the condenser. The cooling cycle uses this work to produce the refrigerative effect at the evaporator, transferring thermal power from the low temperature thermal source to the intermediate temperature thermal sink. The evaporator-condenser loop of the steam ejector refrigeration cycle is similar to a standard vapour-compression refrigeration cycle with the exception that the ejector is

the device that transfers work to the refrigerant. The whole plant exchanges heat with the three thermal sources and requires a relatively small amount of external work to drive the water pump [2].

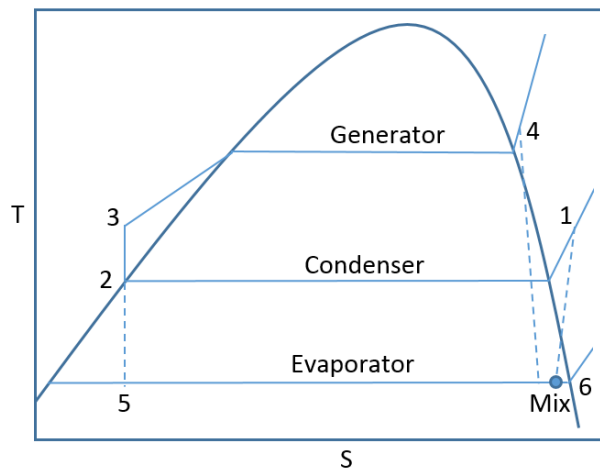


Figure 1-2: Schematic of steam ejector cycle in T-S diagram [2]

Steam ejectors typically consist of four main parts: a primary nozzle, a mixing chamber, a constant area zone and a diffuser. Figure 1-3 shows a schematic of a typical steam ejector illustrating the different parts. An idealized description of ejector operation is presented below.

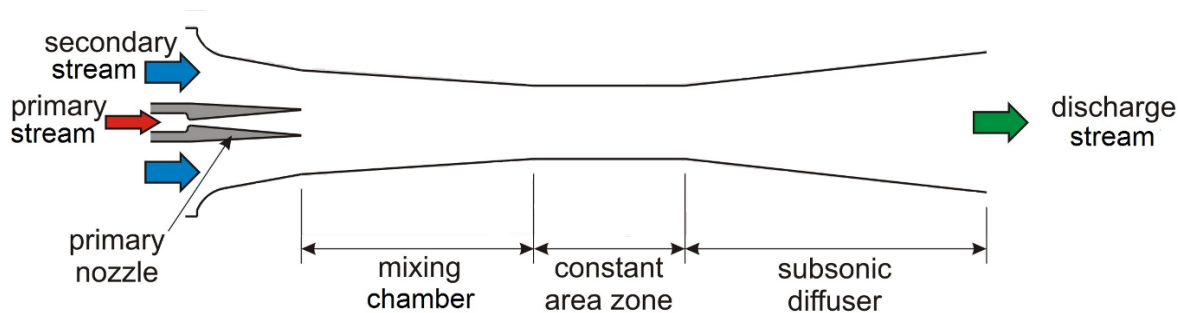


Figure 1-3: Typical ejector cross-section illustrating the different zones

The function of the primary nozzle is to convert the high pressure and low velocity steam (which is produced in the steam generator) into a very high velocity flow with a static pressure lower than that of the low pressure secondary stream. The velocity of steam as it enters the nozzle increases in the converging portion and reaches sonic velocity at the nozzle throat. Beyond the nozzle throat, the velocity of steam becomes supersonic and further increases until the end of the nozzle where a very

low pressure region is created. This vacuum region causes the secondary stream (from the evaporator) to enter the mixing chamber where it mixes with the primary jet leaving the nozzle.

Mixing of the primary and secondary streams continues and within the constant area zone, the mixture undergoes a pressure rise, typically through the action of one or more shock waves which decelerate the flow to a subsonic speed. Further deceleration occurs in the subsonic diffuser portion of the ejector until the fluid reaches the design outlet pressure at the condenser.

There are different parameters to describe the performance of steam ejectors. The most important parameters are the entrainment ratio and the compression ratio. The entrainment ratio or ER is defined as the ratio between the mass flow rates of the secondary stream \dot{m}_s and the primary stream \dot{m}_p , quantities which are denoted in Figure 1-1. The entrainment ratio is related to the energy efficiency of the ejectors and directly affects the coefficient of performance of ejector-based refrigeration cycles as explained in the following paragraph. The second parameter, the compression ratio or CR is the ratio between the discharge (condenser) pressure and the secondary stream's inlet pressure. Higher CR means that the low pressure secondary steam can be recovered to a higher pressure at the ejector discharge.

Ejector refrigeration systems are promising because of their relative simplicity and low capital cost and the fact that the system can be powered primarily by "low grade" energy (for example solar energy) instead of electricity. This means ejector-based refrigeration systems potentially have significant environmental benefits, especially when a renewable energy source such as solar energy can be used. The primary disadvantage with ejector-based refrigeration systems is the low coefficient of performance (COP). The COP of a refrigeration cycle is defined as the ratio between the generated refrigeration effect and the energy input to the cycle. If Q_e and Q_g are the heat exchange rates in the evaporator and generator and W_{mech} is mechanical power required by the cycle, the COP is then defined as:

$$COP = \frac{Q_e}{Q_g + W_{mech}} \quad (1)$$

If Δh_e and Δh_g are enthalpy differences in the evaporator and generator and \dot{m}_s and \dot{m}_p are the mass flow rates of the secondary and primary streams, respectively, then:

$$COP = \frac{\dot{m}_s \Delta h_e}{(\dot{m}_p \Delta h_g) + W_{mech}} \quad (2)$$

In the ejector refrigeration cycle, W_{mech} can normally be neglected compared with the energy required in the generator. Therefore, when incorporating the definition of the entrainment ratio, the COP of the ejector refrigeration cycle can be defined as:

$$COP = ER * \frac{\Delta h_e}{\Delta h_g} \quad (3)$$

Therefore, at given evaporator and generator operating conditions, the entrainment ratio is directly proportional to the COP, meaning that for given thermodynamic states of the system operation, an increase in the entrainment ratio will directly increase the COP [3].

A typical performance curve of an ejector can be categorized into three operating regions as illustrated in Figure 1-4: choked flow, unchoked flow and reversed flow. Choked flow occurs when the discharge pressure is lower than the critical pressure at discharge. When the ejector is operated at outlet pressures lower than the critical discharge pressure, the entrainment ratio remains constant. For the unchoked mode, the secondary stream is no longer choked and its mass flow rate decreases rapidly with increasing discharge pressure which reduces the entrainment ratio. Further increase in the discharge pressure above the break down pressure causes flow to reverse back to the secondary stream's inlet and ejector malfunction occurs.

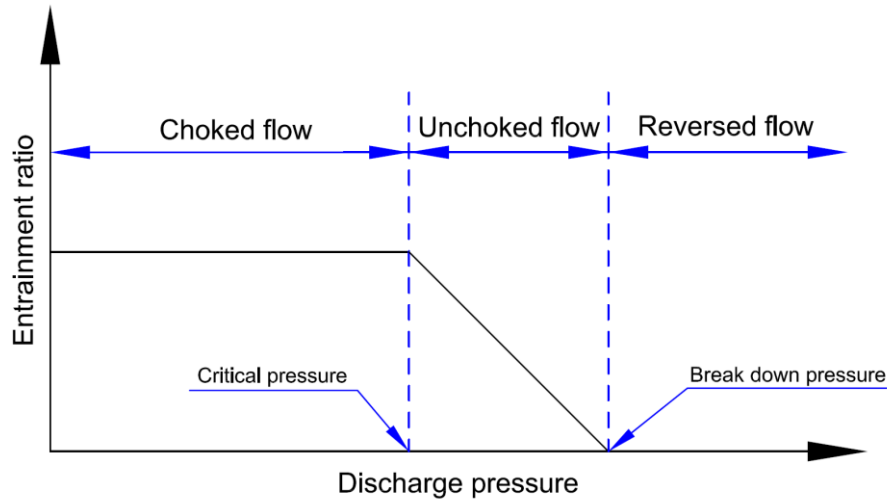


Figure 1-4: Illustrative performance characteristics of a steam ejector

1.1.2 Steam condensation in the primary nozzle

Figure 1-5 illustrates steam expansion from a slightly superheated condition at the inlet to a typical ejector primary nozzle. The expansion process is also presented on a h-s diagram in Figure 1-6. When the dry steam (only slightly superheated) enters the primary nozzle at point 1, it expands in a process which is almost isentropic and its pressure and temperature drops until it reaches the sonic condition at point 2, the throat of the nozzle. Further expansion of steam causes its state to cross the saturation line as shown in Figure 1-6. Depending on the operating conditions, the steam state may actually cross the saturation line before or after the throat and droplet nuclei begin to form and grow in the vapour. However, due to the high flow speed, the residence time of steam in the primary nozzle is small and there is not sufficient time at this stage for the formation of liquid droplets. Associated nucleation rates are so low that effectively the steam still continues to expand as a dry, single phase vapour. This phenomenon is known as supersaturation and the steam that exists in the wet region without containing any liquid is called supercooled or supersaturated steam. Supersaturation is a nonequilibrium or metastable state.

Once the temperature drops a sufficient amount below the saturation temperature at the local flow pressure, the nucleation rate rises significantly and reaches its maximum at point 4 where groups of

steam moisture droplets are formed. This area which is called the nucleation zone is followed by the Wilson point (the point of maximum supercooling or the point where condensation is initiated).

Downstream of point 4, the nucleation process stops and the number of droplets in the flow field remain constant. The steam then experiences a condensation front (often described as a condensation shock) and a sudden rise in its pressure occurs. The generated nuclei grow rapidly in size between the points 4 and 5 and the flow is restored to an almost-equilibrium thermodynamic state. Further expansion of flow after point 5 takes place under close-to-equilibrium conditions. However, following the point 4, entropy increases slightly because there will be some departure from the isentropic process, as shown in Figure 1-5 at the start of nucleation.

During the expansion of steam in the primary nozzle, flow properties including pressure, temperature and Mach number for a condensing wet steam are different at the end of the primary nozzle from those for the hypothetical dry steam due to the occurrence of condensation. The changes due to condensation affect the properties of the primary-secondary stream mixture in the mixing chamber and thus the ejector performance, characterised by the entrainment ratio and compression ratio, can be altered due to condensation effects.

There are different approaches to wet steam modelling: equilibrium and non-equilibrium. For equilibrium modelling, the fraction of fluid in the liquid phase can be determined from two independent thermodynamic variables such as the pressure and the enthalpy. However, for non-equilibrium modelling, the fraction of fluid in the liquid phase is dictated by droplet nucleation and growth or decay processes and may result in liquid fractions significantly different from the equilibrium liquid fraction. A non-equilibrium wet steam models has been used for all computational fluid dynamics simulations throughout this thesis, unless otherwise stated

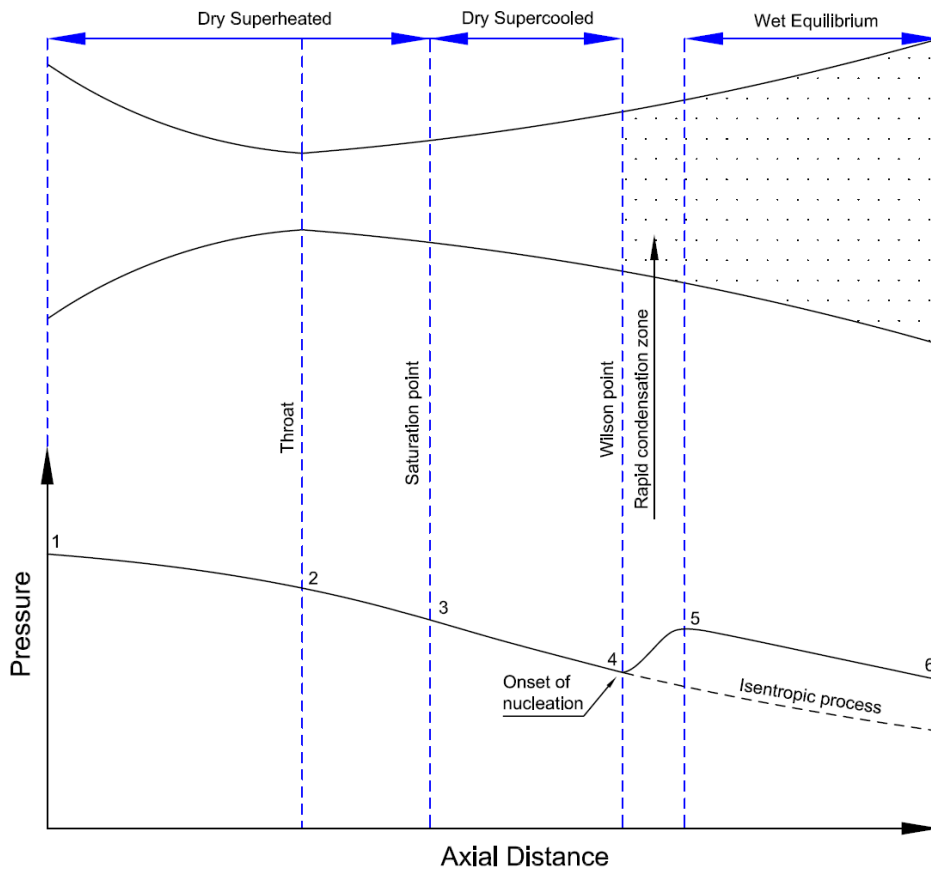


Figure 1-5: Steam condensation in the primary nozzle with axial pressure distribution

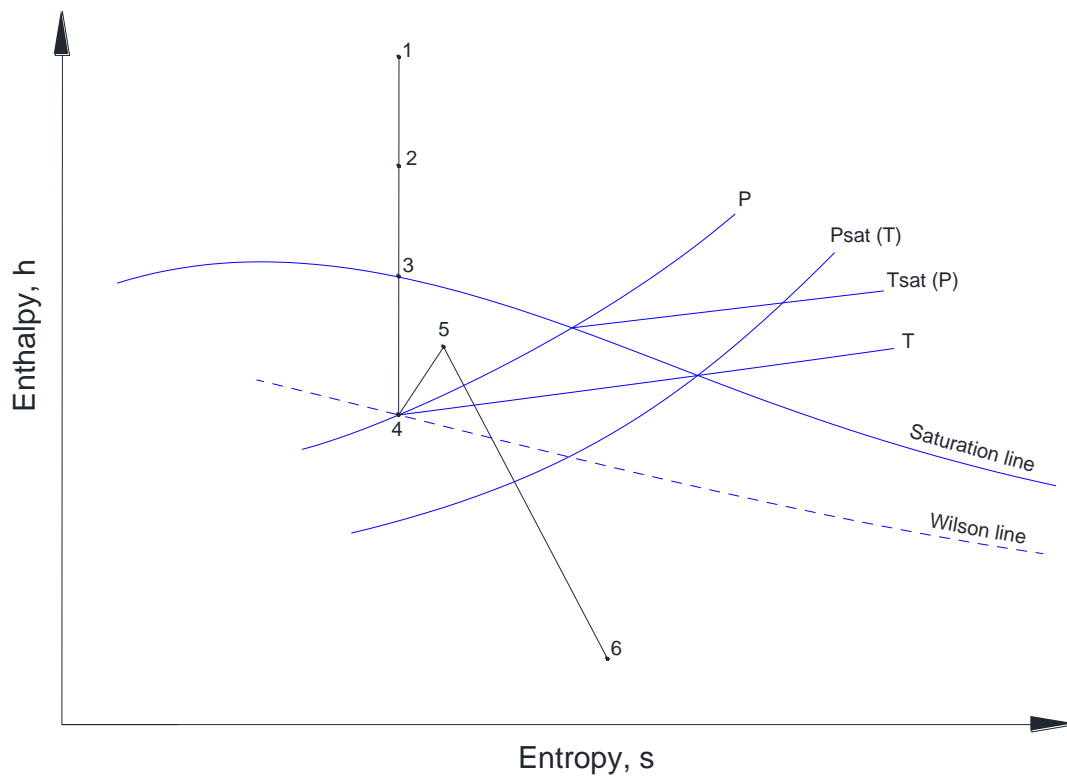


Figure 1-6: h - s diagram of steam condensation in the primary nozzle

1.1.3 Mixing layer development in the mixing chamber

Figure 1-7 shows a schematic of the mixing of the primary and secondary streams at the end of the primary nozzle. As illustrated, when these assumed uniform and nearly parallel streams with different values of velocity start to mix, a free shear layer (also known as a mixing layer) forms at their interface. The thickness of a fully-developed mixing layer δ increases linearly with streamwise distance x , and therefore the growth rate of the mixing layer δ' which is defined as $\frac{d\delta}{dx}$ remains constant [85].

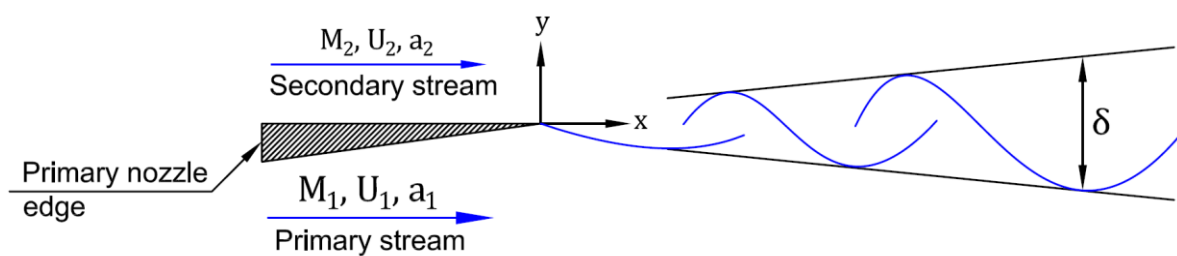


Figure 1-7: Schematic of the mixing layer development at the primary nozzle exit

The growth rate of the mixing layer is an important parameter affecting the ejector entrainment ratio. A more rapidly growing mixing layer implies additional mass entrainment of the secondary stream into the mixing layer which leads to a higher entrainment ratio for the ejector. Steam properties at the end of the primary nozzle, where the primary and secondary streams first meet, also play an important role in the mixing layer growth rate. These properties can change with the change of the ejector operating condition and steam condensation in the primary nozzle also plays an important role in determining these flow conditions.

1.2 Objectives of the dissertation

The aim of the present work is to study the effect of steam condensation on flow properties in the primary nozzle and also on the ejector performance including entrainment ratio and compression ratio. Ejector entrainment and compression ratios are related to the mixing between the primary and secondary streams so the work also aims to investigate the role which condensing steam plays on the

mixing layer growth between the primary and secondary stream. The main objectives of this study can be described in the following items.

1. Nozzle flow characterization: effects of steam condensation on primary nozzle flow and deduction of possible impact on the ejector performance with the aid of computational simulations validated with existing experimental data from other researchers.
2. Ejector flow investigation downstream of the primary nozzle: effect of steam condensation on the mixture properties, mixing process and the ejector entrainment ratio using the computational simulations validated with available experimental data for the particular steam ejector apparatus in the USQ research facility. Mixing characterization in the co-flowing steam jet apparatus: investigation of the mixing process between the primary and secondary streams with calculation of the mixing layer thickness and growth rate using the experimental data obtained from the pitot pressure probe together with the computational simulations.
3. Flow investigation downstream of the primary nozzle in a co-flowing steam jet apparatus: measuring the properties of the mixed stream including static and total pressure using pitot and static pressure probes designed for this work.

1.3 Overview of the dissertation

This thesis first introduces the research theme, and then presents a review of related literature. Four major studies which address the main objectives of this research are then presented. A conclusion that summarises the general findings and contributions of this study, and some recommendations for future works is also presented. The major studies are presented as four papers: three published in the archival journals and one prepared for submission. The published journal manuscripts that resulted from this research are the following:

- Paper I: Ariaifar, K., Buttsworth, D., Sharifi, N. and R. Malpress, *Ejector primary nozzle steam condensation: Area ratio effects and mixing layer development*. Applied Thermal Engineering, 2014. 71(1): p. 519-527.
- Paper II: Ariaifar, K., Buttsworth, D., Al-Doori, G. and R. Malpress, *Effect of mixing on the performance of wet steam ejectors*. Energy, 2015. 93: p. 2030-2041.
- Paper III: Ariaifar, K., Buttsworth, D., Al-Doori, G. and N. Sharifi, *Mixing layer effects on the entrainment ratio in steam ejectors through ideal gas computational simulations*. Energy, 2016. 95: p. 380-392.

1.3.1 Chapter 2 Literature review

The literature review is presented in four main sections: the first section discusses main works performed in the field of steam ejectors, including both analytical and experimental works. The second section discusses the computational simulations and investigations of steam ejectors using the ideal gas and wet steam models, while the third section reviews the literature of steam nucleation in Laval nozzles. The last section of this chapter is allocated to an overview of the mixing process of two parallel streams and parameters that have been used to define the growth rate of compressible mixing layers.

1.3.2 Chapter 3 Flow characteristics in the primary nozzle

This chapter consists of the published paper that studies flow characteristics in the ejector primary nozzle. It presents a computational simulation to study the effects of steam condensation on flow properties in the nozzle. The wet steam model adopted herein predicted the location of steam condensation in the nozzle and defined the number of liquid droplets which form due to condensation at a particular operating condition. The numerical method was validated with three different sets experimental data reported in the literature.

1.3.3 Chapter 4 Effect of steam condensation of the ejector performance

This chapter contains the published paper that discusses the effects of steam condensation on the ejector entrainment ratio and compression ratio. A wet steam model was used to simulate steam behaviour in a particular steam ejector. The numerical results were compared with the previously-obtained experimental data on an ejector which was designed and operated at USQ for prior research work. The effects of steam condensation on the mixing layer growth rate in the ejector are also investigated through this chapter.

1.3.4 Chapter 5 Effects of mixing on the ejector entrainment ratio

The published paper that investigates the mixing layer effects on the ejector entrainment ratio forms the basis of Chapter 5. A numerical approach is presented in which flow in a representative steam ejector is examined in order to specify the contribution of pressure-driven effects and the mixing-driven effects to the overall ejector entrainment ratio. The turbulent mixing model for calculation of the mixing layer thickness and growth rate was validated by using experimental data for compressible mixing layers available in the literature.

1.3.5 Chapter 6 Pitot and static pressure measurements in a co-flowing steam jet

This chapter is allocated to the experimental part of the research study. It describes a co-flowing steam jet apparatus and probe systems used to measure the pitot and static pressures of a steam jet. Design details of the components and parts of the apparatus are presented in Appendix A. The development of the mixing jet was examined using measurements from a pitot pressure probe. A supersonic static pressure probe was designed for measuring the static pressure of the supersonic region of the mixing jet, while a subsonic static pressure probe was applied in the subsonic region. Computational simulations were also performed to assess the effectiveness of wet steam and Reynolds-averaged Navier-Stokes modelling in the numerical simulation of the experimental data.

1.3.6 Chapter 7 Conclusion

The last chapter presents the overall conclusions and outcomes of this research study and recommendations for future works.

Chapter 2 Literature review

A large number of investigations have been carried out in order to improve the performance and optimise the design of steam ejectors. Analytical methods have provided an important framework for early development of the ejector design. Many recent studies have used a combination of experimental data and computational simulations. Such studies have been performed to provide a better understanding of flow characteristics within ejectors. However, the existing literature does not:

1. Describe the effect of steam condensation on flow properties at the primary nozzle exit and how these affect the mixing layer growth rate;
2. Probe the origins of the effects of steam condensation on the ejector performance;
3. Examine the effect of the mixing layer development on the ejector entrainment ratio; nor
4. Provide detailed measurement of steam mixing in a co-flowing steam jet suitable for validation of steam ejector modelling.

Each of the above topics is addressed in the papers presented in the chapters following this literature review chapter. Each paper contains its own introduction and review which contextualises the scope of each paper's research contributions.

2.1 Steam ejector studies

2.1.1 Analytical works

In 1910 Le Blanc and Parson [4] introduced a cycle having a vapour jet ejector. This arrangement allowed the production of a refrigeration effect by utilizing low grade energy steam. However, the design was based primarily on empirical results. Keenan and Neumann [5] were the first to establish a theory of ejector operation based on one dimensional gas dynamics and this theory formed a basis for the design of ejectors. This theory was then modified to include loss coefficients in different parts

of the ejector by Eames et al. [6]. Eames [7] modified Keenan's constant pressure model and proposed a new method based on a constant rate of momentum change prescription for the variation of the ejector cross sectional area. This new model aimed to overcome the sudden fall in total pressure through the thermodynamic shock in the conventional ejector diffuser. Defrate and Hoerl [8] developed a computer code for the performance evaluation of an ejector system operating with ideal gas using Keenan's theory.

Munday and Bagster [9] proposed a theory in which the existence of an aerodynamic throat was assumed for the secondary stream and Huang et al. [10] continued this approach, assuming the secondary stream throat location is within the constant area section of the ejector. Such a gas dynamic modelling approach was extended by Zhu et al. [11] to accommodate a variation in the axial velocity across the primary and secondary streams. According to such gas dynamic modelling, which is based on the assumption of ideal gas behaviour, the static pressure at the exit of the primary nozzle is of critical importance because it dictates the cross-sectional area available for the choked secondary stream.

Sherif et al. [12] presented a model for a two phase ejector to describe the flow of two-phase primary fluid inducing a secondary liquid (saturated or subcooled) into the ejector mixing chamber. The working fluid was R-134a but the analysis could be applied to other refrigerants such as R-22 and R-113. The model was capable of accounting for phase transformations due to compression, expansion, and mixing. A computer code was proposed by Cizungu et al. [13] to analyse the performance of an ejector refrigeration system operating with different environment-friendly pure refrigerants R123, R134a, R152a and R717. They found R134a and R152a to be appropriate for heat sources at 70 to 80 °C and R717 for temperatures higher than 90 °C.

Aidoun and Ouzzane [14] developed a 1-D model, based on a forward marching solution technique to study ejector operation and performance for refrigerant R-141b. They found that internal superheating of the working fluid occurred because of the mixing of the flow streams in the mixing

chamber and the normal shock wave inside the constant section zone. The internal superheat generation increased for off-design operation due to inefficient mixing and because the normal shock waves generated in the mixing chamber became stronger at off-design conditions, leading to high losses and superheating of the working fluid. They also concluded that some degree of superheating for the primary fluid (around 5 °C) was required to prevent condensation in the primary nozzle of the ejector. Selvaraju and Mani [15] included the effect of friction within the constant area mixing chamber and changes in the specific heat of the working fluid in a computer code to obtain a better performance for different ejector operating conditions and different area ratios. Yapici and Ersoy [16] performed a theoretical analysis of the ejector refrigeration system based on a constant area ejector analysis and presented the optimised results for R-123. Their model showed a better entrainment ratio compared with a similar model suggested by Sun and Eames [17] under the same operating conditions.

Chou et al. [18] analysed the occurrence of flow choking in an ejector of a refrigeration system and developed a model for predicting the maximum entrainment ratio. They used a multi-parameter equation to calculate the entrainment ratio which took into account the performance of the primary nozzle, flow entrainment and mixing at different operating conditions. They validated the model with refrigerants R113, R141b and steam using reported experimental data. It was shown that the presented model provided a better accuracy compared with results obtained from the existing 1-D ejector theory.

2.1.2 Experimental works

2.1.2.1 Operating conditions

Ejector operating conditions affect the ejector performance as defined by the entrainment ratio and the compression ratio. Many experiments have been performed to investigate the effects of operating conditions on the ejector entrainment ratio and compression ratio.

According to experimental studies [6, 19, 20] carried out on steam ejectors, the pressure of the boiler (primary stream), evaporator (secondary stream), and condenser (diffuser exit) has an important influence on the value of entrainment ratio. Increasing values of condenser pressure (diffuser exit pressure) cause the ejector to transition from the choked flow operating zone into the unchoked flow operating zone and ultimately into the reversed flow regions of the performance map. With such increases in the condenser pressure, the entrainment ratio changes from a positive and constant value (in choked flow region) to a reducing value (in unchoked flow region) and a negative value (in reversed flow region).

Sun [21] studied the characteristics of an experimental ejector in a steam refrigeration system over a range of operating conditions. The experimental results showed that increasing the boiler temperature caused the entrainment ratio to first increase and then decrease. Sun found that the choking phenomena in the secondary stream played an important role in the ejector performance as it leads the ejector to operate in a constant capacity in the choked flow region.

Chunnanond and Aphornratana [22] performed an experimental investigation to measure the static pressure along the ejector duct at various operating conditions and explained the flow characteristics through the steam ejector. They concluded that the performance of a steam ejector was affected by the amount of secondary flow passing through the mixing chamber and the momentum of the mixed stream. Reduction of boiler pressure decreased the primary stream mass flow rate and increased the

ejector entrainment ratio. On the other hand, an increase in evaporator pressure, caused an increase in the secondary stream mass flow rate and increased the entrainment ratio.

Bartosiewicz et al. [23] conducted an experiment on a model supersonic ejector to measure static pressure along the ejector centreline using a capillary probe located on the ejector axis. They used different operating conditions in the experiment ranging from choked flow to unchoked flow operation. They used CFD for ejector analysis and evaluated the performance of six well-known turbulence models against experimental data. It was concluded that the $k - \omega SST$ turbulence model agrees best with experiments.

Yapici and Yetisen [24] designed and constructed an ejector refrigeration system to operate using R11 as the working fluid. The objective was to investigate the effects of main operating parameters on the system performance. They concluded that if a higher cooling capacity and lower evaporator temperature is desired from the system, the boiler temperature should be increased significantly.

Sankarlal and Mani [25] designed a vapour ejector refrigeration system to operate with ammonia and studied the effect of non-dimensional parameters including compression ratio, expansion ratio (pressure ratio of boiler to evaporator) and ejector area ratio (the ratio between the area of the ejector constant area zone and the area of the primary nozzle throat) on the system performance. Their experimental results showed that the entrainment ratio increased with: (1) increase in ejector area ratio; (2) increases in the expansion ratio; and (3) decrease in compression ratio.

Chen et al. [26] carried out an experimental study on an ejector in a refrigeration system using different refrigerants. They determined the critical choking conditions for variation in operating conditions and compared the performance of the ejector for different refrigerants. They suggested that external superheating of the primary stream before delivery to the ejector eliminates small droplets formed at the nozzle exit which could reduce the effective area available for the secondary stream.

Pounds et al. [27] conducted an experimental study of an ejector refrigeration system to determine the effect of high-temperature evaporator (HTE) conditions in which temperatures ranged from 120 to 135 °C, low-temperature evaporator (LTE) conditions in which temperatures ranged from 5 to 15 °C and condenser temperatures of 7 to 30 °C. They found that the system could achieve an entrainment ratio of 1.7, higher than that typically reported in the literature but at the expense of reduced critical back pressure.

2.1.2.2 Geometric parameters

There are different geometric parameters which affect the performance of steam ejectors, including primary nozzle geometry, nozzle exit position (NXP), ejector area ratio and mixing chamber geometry. A number of experiments have been performed to investigate the influence of each parameter on the performance of steam ejectors.

Ruangtrakoon et al. [28] studied the effect of primary nozzle geometry on the system performance of a steam jet refrigeration cycle. They used primary nozzles with different geometries to investigate the effect of nozzle throat diameter and nozzle exit Mach number on entrainment ratio. Their experimental results showed that for a fixed boiler and evaporator saturation temperature, the nozzle with larger throat diameter (which increases the primary fluid mass flow rate and the jet core of the primary fluid and decreases the effective flow area for the secondary fluid) entrained less secondary fluid to the mixing chamber which resulted in a lower ejector entrainment ratio. Moreover, there was no effect on entrainment ratio using nozzles with different exit Mach numbers, unless the nozzle which produced a higher exit Mach number helped the ejector to operate at a higher critical condenser pressure.

Chang and Chen [29] applied a petal nozzle (shown in Figure 2-1) in an effort to increase the performance of a steam jet refrigeration system. They also investigated the characteristics of this novel application under different ejector operating conditions. They found that the ejector

compression and entrainment ratios could be enhanced if the petal nozzle was used in an ejector with larger area ratio. Their results also showed that for an ejector with the petal nozzle, there was an optimum value for area ratio under which a maximum compression ratio could be achieved.

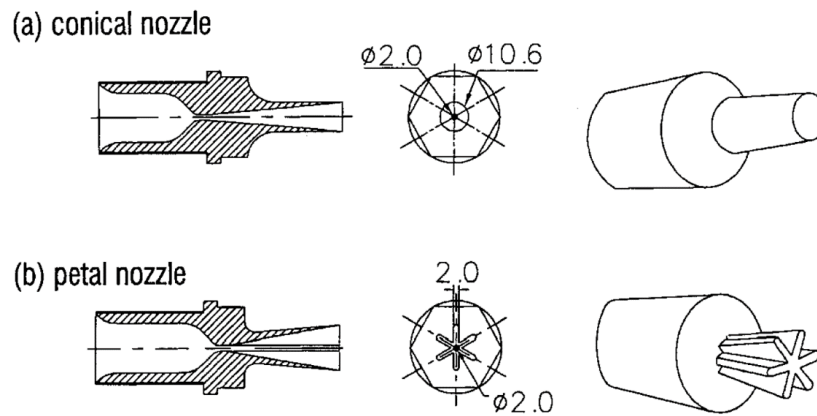


Figure 2-1: Primary nozzle geometries used by Chang and Chen [29]

Chaiwongsa and Wongwises [30] investigated the effect of primary nozzle exit diameter on the performance of the refrigeration cycle using a two-phase ejector driven by the working fluid R-134a. They tested nozzles having three different outlet diameters in the range of 2 – 3 mm and found that the nozzle with smallest outlet diameter produced a higher ER.

Similar experiments were carried out by Chen and Sun [3] on a steam ejector refrigeration system. They designed three different primary nozzles with different outlet plane diameters and investigated the effect of the primary nozzle exit Mach number on the ejector critical back pressure and entrainment ratio. They determined that excessively increasing the nozzle exit Mach number was unnecessary and there existed a moderate value of nozzle exit Mach number (in the range of 2.7 to 5) for practical operation of a steam ejector refrigeration system.

Nozzle exit position (NXP) is typically defined as the distance between the primary nozzle exit plane and the mixing chamber inlet plane. Chunnanond and Aphornratana [22] found that retracting the primary nozzle out of the mixing chamber (negative NXP) could increase the ejector entrainment ratio,

but it caused the ejector to operate at a lower critical condenser pressure. Dong et al. [31] developed a steam ejector refrigeration system with a moveable primary nozzle in order to determine the effect of nozzle exit position on the entrainment ratio ER. The NXP was adjusted from -19 mm to +176 mm relative to the entrance of the mixing chamber. Their experimental results showed that under a constant primary and secondary operating conditions, the highest values for ER was achieved with NXP between +56 mm and +86 mm, and for highest critical back pressure between +76 mm and +116 mm.

Eames et al. [32] performed an experimental investigation on a ejector refrigeration system to assess the performance of R245f as a refrigerant. The ejector used in this system was designed with the method of constant momentum rate change (CMRC). They found that NXP had strong influence on system entrainment ratio. At a nozzle exit position of 5 mm upstream from the entrance of the mixing chamber (NXP = -5 mm) the ER could increase by as much as 40%. A similar result was also obtained by Yapici [33] who carried out an experimental investigation on an ejector with a moveable primary nozzle and concluded that the NXP should actually be located at 5 mm downstream of the mixing chamber inlet plane to maximise the entrainment ratio.

The effects of area ratio on an ejector refrigeration system using R123 as the working fluid was studied by Yapici et al. [34]. They selected six configurations for the ejector over a range of area ratios and determined the condenser pressure so that the secondary flow choking occurred even for the ejector with the smallest area ratio. It was concluded that the optimum area ratio increased approximately linearly with boiler temperature.

Ma et al. [19] developed a novel steam ejector for a refrigeration system. They used a spindle located in front of the primary nozzle inlet to control the value of primary fluid mass flow rate (Figure 2-2). Their investigations showed that the cooling capacity decreased when the spindle moved toward the nozzle due to decrease in the primary flow mass flow rate. It was also demonstrated that the critical back pressure rose when the spindle was moved towards the nozzle.

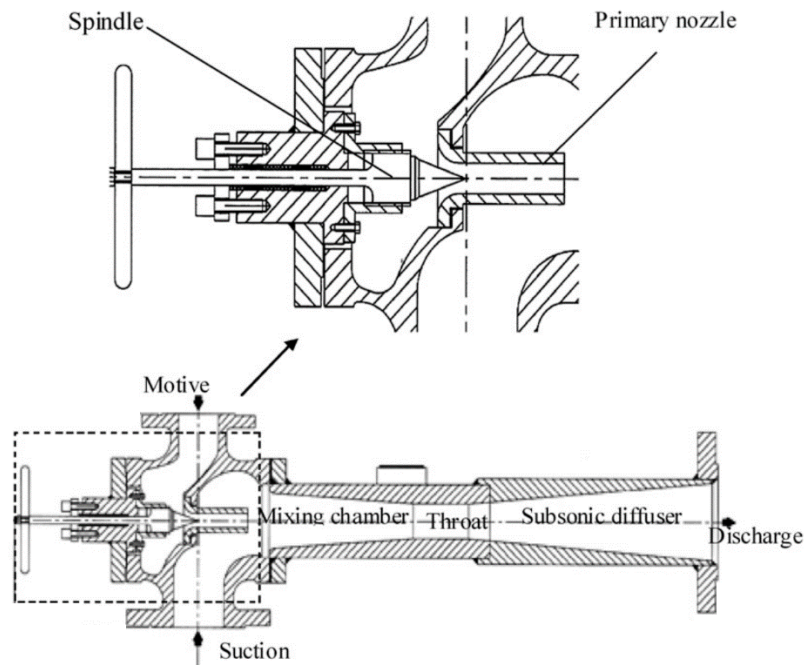


Figure 2-2: Configuration of the steam ejector designed by Ma et al. [19]

A similar experiment with the spindle application was performed by Varga et al. [35] on a steam ejector. They found that the primary flow rate could be adjusted by the spindle where the spindle tip position varied in front of the primary nozzle. A maximum in the entrainment ratio for the ejector was achieved by spindle adjustment when the ejector was operated under fixed conditions of pressure and temperature for the primary, secondary, and diffuser outlet.

Aphornratana et al. [36] performed an experimental study on an ejector refrigeration system using R11 as the working fluid. They used two different mixing chambers with constant area inlet and convergent inlet, both with the same constant area section diameter (Figure 2-3). It was concluded that under a specific range of operating conditions the choking of the fluid always happened with the use of constant area inlet mixing chamber but not for the convergent inlet chamber.

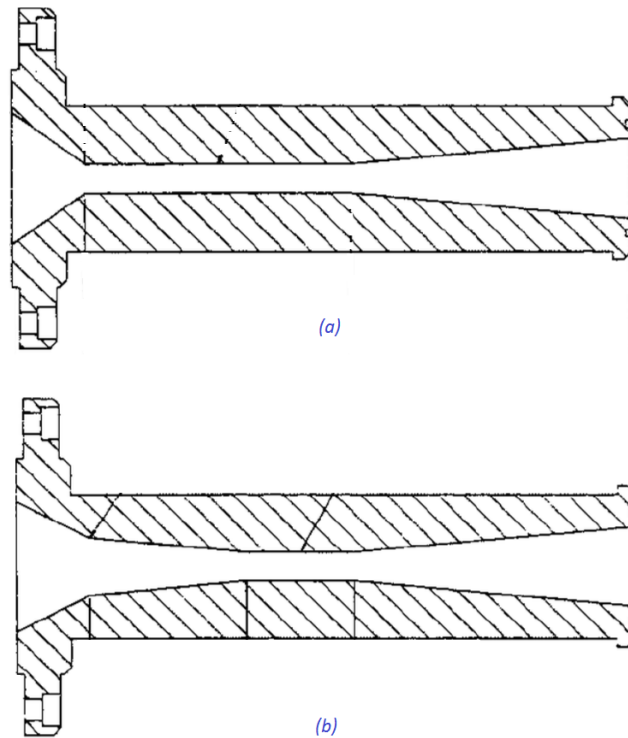


Figure 2-3: Different mixing chamber configuration used by Aphornratana et al. [36]; (a) constant area inlet, (b) convergent inlet

Shah et al. [37] developed an experiment on a steam ejector using a transparent mixing chamber for flow visualization. They investigated the effects of mixing section length on the transport process in the steam ejector using three different lengths for the mixing section (110, 130 and 150 mm) and observed a better performance (entrainment and compression ratio) for the ejector when using the mixing section with the shorter length.

2.2 Computational simulations of steam ejectors

Recently, computational fluid dynamics (CFD) has been applied to the design and optimization of ejectors because of the ability of CFD to simulate the flow field inside complex geometries. CFD modelling can provide simulations of the ejector that offer good agreement with experimental results. A number of computational simulation works performed on ejector refrigeration systems and published in the literature are reviewed in this section.

2.2.1 Ideal gas simulations

For ejector applications where the operating pressures are relatively low and where the working fluid state does not reach saturation conditions, an ideal gas assumption for the working fluid is an acceptable assumption and provides similar results to a real gas model.

2.2.1.1 Investigation on operating conditions and flow physics

Ouzzane and Aidoun [38] developed a model and computer programs for design and detailed simulation of ejectors for refrigeration systems. Their analysis focussed on refrigerant R142b and compared results from experiments with this CFD model and a theoretical 1-D model. They concluded that simulations from the CFD model provided a better agreement with experimental results (differences were typically less than 16%) than the 1-D model.

Bartosiewicz et al. [23] compared pressure distribution data along the ejector axis obtained from experiments with different turbulence models and concluded that the $k - \omega$ SST turbulence model agreed best with experiments. The $k - \omega$ model and the RNG model were found the best suited in prediction of shock waves and pressure recovery but the $k - \omega$ SST was found to perform better compared to RNG model regarding the stream mixing. Later Bartosiewicz et al. developed their work on a supersonic ejector for refrigeration applications [39] and simulated the ejector model using R142b as the working fluid with consideration of shock-boundary layer interactions. The aim was understanding the local flow structure and the important role of the secondary nozzle for the mixing rate performance.

Sriveerakul et al. [40] studied the effect of operating pressures on flow structure and mixing process inside a model of a steam ejector. They found that there are two series of oblique shock waves in their ejector simulations. The first series were formed immediately after the primary stream leaves the primary nozzle and the second series formed at the beginning of the diffuser section (Figure 2-4).

Increasing condenser pressure causes the shock position to move upstream into the ejector throat and affects the mixing process if the ejector operates within the choked flow region.

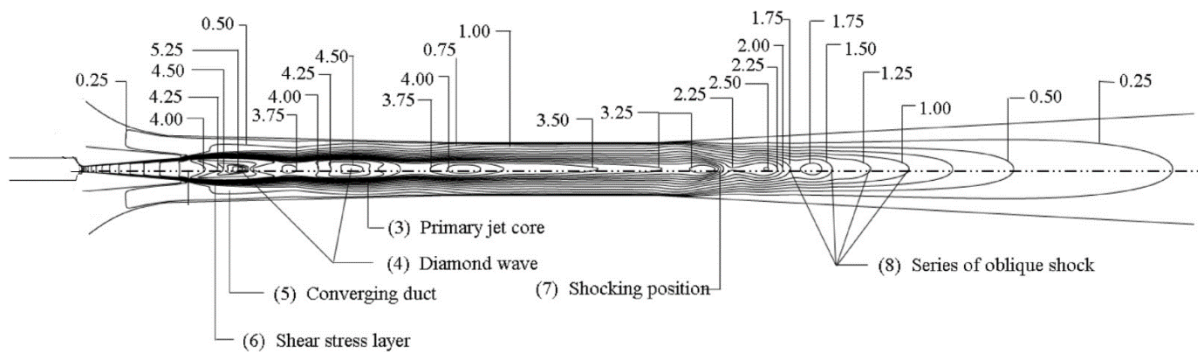


Figure 2-4: Contours of Mach number in the steam ejector [40]

Pianthong et al. [41] performed a CFD investigation to study the effect of operating conditions on flow phenomena and performance of a model steam ejector. The simulation results revealed that CFD is able to predict the effect of operating conditions on the effective area and sizes of the jet core in the mixing chamber (Figure 2-5). Increasing the jet core size by an increase in the boiler pressure or by a decrease in the evaporator pressure, caused a reduction in the effective area in the mixing chamber which resulted in the reduction of entrainment ratio.

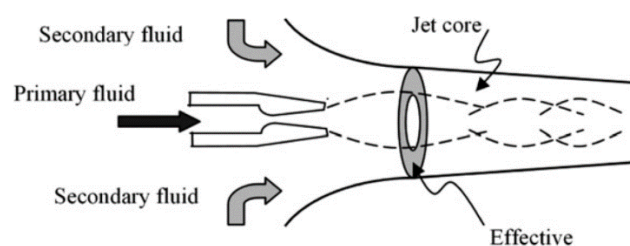


Figure 2-5: Effective area occurring in the ejector throat [41]

Hemidi et al. [42] conducted a CFD analysis on a supersonic air ejector based on the $k - \varepsilon$ turbulence model and the $k - \omega SST$ model and compared the predicted entrainment ratio from both models with experimental data. Over a range of operating conditions, the CFD results showed that the overall

deviation was below 10% for the $k - \varepsilon$ model, while the results for the $k - \omega$ SST model did not offer as good agreement. They also found that the different turbulence models predicted distinctly different local flow structures.

Wang and Dong [43] used the realizable $k - \varepsilon$ turbulence model to investigate the mixing behaviour of the primary and secondary streams in a model steam ejector. They found that when the discharge pressure was higher than critical back pressure, a swirling effect was associated with the separation of the secondary stream near the wall and the reduction of the secondary stream velocity caused the entrainment ratio to reduce rapidly.

Sharifi and Boroomand [44] investigated the flow pattern inside a conventional model of an ejector using the realizable $k - \varepsilon$ turbulence model. They applied two numerical schemes on the basis of axisymmetric and three dimensional assumptions to analyse the performance parameters and compared the results with experimental measurements obtained from an industrial desalination unit. It was shown that the axisymmetric model was capable of predicting similar results to the 3-D model and both achieved agreement with experimental data to within about 10%.

2.2.1.2 Investigation of geometry

Riffat and Omer [45] performed a CFD analysis of an ejector refrigeration system using methanol as the working fluid. They studied the effect of the relative position of the primary nozzle exit within the mixing chamber on the simulated ejector performance. CFD results demonstrated that if the nozzle exit was located at least 2.5 mm (equivalent to 0.21 times the length of the constant area section diameter) downstream of the mixing chamber inlet, a higher entrainment ratio would be achieved relative to positioning it in the mixing chamber.

Rusly et al. [46] simulated different ejector designs to determine the flow dynamics in R141b ejectors using a real gas model and analysed the simulated performance of ejectors relative to a range of experimental data. It was found that the maximum entrainment ratio could be achieved in the ejector

just before the occurrence of a shock in the diffuser section of the ejector. The primary nozzle position was also an important parameter in the ejector design.

Sriveerakul et al. [20] performed a CFD analysis of the effect of ejector geometries on the flow structure and shock position inside a model of a steam ejector. The results showed that when using a larger diameter primary nozzle, a larger jet core with a higher momentum was produced but this resulted in the entrainment of less secondary fluid into the mixing chamber but a higher critical back pressure was achieved. The length of the constant area section had almost no effect on the flow structure inside the ejector but higher critical back pressure could be achieved with longer lengths of the constant area section.

Zhu et al. [47] employed the CFD technique to study the effects of the primary nozzle exit position and the mixing chamber converging angle on the ejector performance. They found that the optimum NXP was not only proportional to the mixing chamber throat diameter, but also increased as the boiler pressure rose. The entrainment ratio varied by as much as 26.6% with changes in the convergent angle and to maximize the ejector performance, a large contraction angle was required when the primary flow pressure increased.

Varga et al. [48] performed a numerical assessment of the effect of geometry on the performance of a model steam ejector. They considered three parameters: the ejector area ratio, nozzle exit position and constant area section length. The results showed that there was an optimal area ratio depending on operating conditions when a spindle was used to tune the primary flow rate. NXP affected both entrainment ratio and critical back pressure and the constant area section length had little influence on entrainment ratio but a longer length produced a higher critical back pressure. Later, Varga et al. estimated different efficiencies for the primary nozzle, suction region, mixing region and diffuser using the results of a CFD model [49]. The results demonstrated that the primary nozzle efficiency was independent of the operating conditions and it only changed with throat diameter. Suction efficiency also remained constant for the majority of operating conditions but decreased when the discharge

pressure was higher than the critical back pressure. Diffuser efficiency was a function of condenser pressure and an increase in discharge pressure increased the diffuser efficiency.

Ji et al. [50] conducted a CFD investigation of a model steam ejector and studied the effects of ejector geometry on the flow structure and the ejector performance. They considered the effect of the converging angle of the mixing chamber within the range from 0 to 4.5° and concluded that under a specific operating condition, the ejector with a converging duct angle of 1° had the best performance.

Opgenorth et al. [51] employed a novel design for the ejector primary nozzle in an effort to improve the ejector performance by increasing the mixing of the streams through adding lobes at the nozzle exit plane (Figure 2-6). They determined the effect of aspect ratio and perimeter of the lobes on system pressure recovery and entrainment ratio. They achieved a pressure recovery ratio of 6.4 relative to a ratio of 4 for the baseline geometry with a 30 mm perimeter value. Beyond this value, the recovered pressure decreased due to frictional losses.

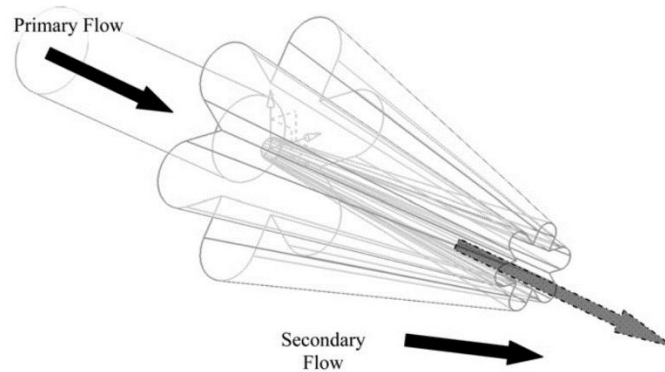


Figure 2-6: Design concept for a lobed nozzle in order to increase the mixing process [51]

Yang et al. [52] numerically investigated the effects of five different nozzle geometries on the performance of a model steam ejector. They clarified the characteristics of the mixing process based on the simulation results of the streamwise vortex and spanwise vortex distributions in the mixing chamber and the internal energy variations along the streamwise distance. It was concluded that interaction of vortices and the mixing chamber wall at an early stage in the ejector increased the

kinetic energy loss and reduced the effective area for secondary flow to pass through, resulting in a reduction of entrainment ratio and critical back pressure.

Ruangtrakoon et al. [53] performed a CFD simulation to determine the effect of primary nozzle geometry on the performance of an ejector used in a steam refrigeration system. They selected eight different primary nozzles with fixed mixing chamber geometry and found that the position of the shock in the mixed stream and the expansion angle of the primary stream leaving the nozzle exit plane both played important roles in the ejector performance. It was also shown that $k - \omega SST$ turbulence model provided more accurate results than the realizable $k - \varepsilon$ model, compared with experimental data.

Lin et al. [54] used the CFD technique to investigate the optimum geometry of an adjustable ejector to maximise the pressure recovery in a refrigeration system using R134a as the working fluid. It was demonstrated that the pressure recovery ratio was very sensitive to the nozzle diverging angle and the length of the mixing chamber. They compared the results of three turbulence models with experimental data and concluded that $k - \omega SST$ model agreed best with experiments.

2.2.2 Wet steam simulations

The conditions under which water vapour flows begin to condense are already quite well understood and such conditions often occur in steam ejectors. Droplet nucleation and the subsequent development of condensation result in a number of energy transfers which cannot be accurately simulated by assuming that the steam behaves as an ideal gas.

Therefore, recent CFD simulations of steam ejectors have incorporated droplet nucleation and condensation models. Some valuable numerical assessments of ejectors have been completed to study nucleation phenomenon and to investigate steam flow behaviour while taking steam condensation into consideration.

Yang and Shen [55] simulated the spontaneous condensation of steam in a 2-D model of a Laval nozzle based on the classical nucleation theory and the Virial style equation of state. The results revealed the physical features associated with the condensation front (shock) and the effect of the condensation front on the nucleation process and the droplet size distribution.

Wang et al. [56] proposed a mathematical model for transonic flow to investigate the flow behaviour of the flow in the primary nozzle of a steam ejector. It was shown that spontaneous condensation occurred as the steam passed through the nozzle. They concluded that the efficiency of the primary nozzle decreases as steam condensation reduces the supersonic expansion process in the nozzle, with a consequent effect on the steam ejector performance.

Grazzini et al. [57] fabricated an experimental refrigeration system based on a two-stage steam ejector using the ideal gas model for the design process. They compared this model with two other models including a saturated vapour model and a metastable vapour model to check the validity of the ideal gas assumption. They found that the classical nucleation theory indicated that the Wilson line was crossed at the nozzle throat. Steam condensation produced a significant difference in the conditions at the nozzle outlet plane.

Sharifi et al. [58, 59] performed a numerical simulation of a steam ejector under the assumption of homogenous nucleation. They developed a code for wet steam simulation linked to a computational fluid dynamic solver to calculate wet steam related variables. The simulation results showed that steam condensation in the primary nozzle reduced the value of the flow Mach number throughout the ejector and increased entrainment ratio and critical back pressure compared to the ideal gas assumption. Similar results were also obtained by Wang et al. [60], Zheng et al. [61] and Cai and He [62].

Wang et al. [63] investigated the effects of primary steam superheating on steam condensation in the primary nozzle and the performance of steam ejectors. The results indicated that superheating of the

primary stream could weaken the intensity of the spontaneous condensation and postpone its occurrence in the primary nozzle. They concluded that a higher entrainment ratio could be achieved by superheating the primary stream due to an improved mixing process between the primary and secondary streams with superheating level less than 20 K.

2.3 Steam nucleation theory in Laval nozzles

The theory of steam nucleation in converging-diverging nozzles has been studied for several decades. Some valuable documents which have been published in the literature are reviewed below.

Moore et al. [64] measured the pressure distribution along the axis of Laval nozzles with five different geometries and compared the experimental results obtained with a theoretical analysis of wet steam flow. Moore et al. [64] also measured the fog droplets diameter using a light scattering method and compared measured values with theoretical results at the position of the optical axis in the nozzles.

Bakhtar and Zidi [65] conducted an experimental investigation of supersaturation in high pressure steam in three convergent-divergent nozzles with different geometries and nominal rates of expansion. They focused mainly on pressure distributions along the centreline of the nozzles, but they also obtained some droplet measurements. Later Bakhtar and Zidi used their experimental results to compare with results obtained from a one dimensional theoretical investigation of steam nucleation in flowing high pressure steam [66]. They found good agreement between the theoretical results and the measured pressure distributions, but some significant differences were observed for the case of the measured and simulated droplet sizes. They introduced some correlations to calculate the saturation and supercooled thermodynamic properties of water as a function of temperature.

The spontaneous condensation of steam in supersonic nozzles was also studied by Young [67]. Later, Young proposed a complete set of conservation equations for vapour droplets in multiphase steam flows [68, 69]. Young also developed two and quasi three dimensional calculation methods for

nonequilibrium steady flows of wet steam in turbine cascades [70] to compute all types of wet steam flow including those involving secondary nucleation.

A numerical investigation of two dimensional flows of nucleating and wet steam was carried out by Bakhtar and Tochai [71] using a time marching method. They compared the numerical results with two sets of experimental data and presented some predictions of two phase effects in turbine blade cascades.

White and Young [72] proposed a two dimensional time marching technique to predict unsteady phenomena in condensing steam flows. They used an Eulerian method for solving the conservation equations while nucleation and droplet growth calculations were performed in a Lagrangian framework. They presented and validated the results for flows in nozzles for which experimental data were available.

Gerber [73] developed an Eulerian-Lagrangian two phase model for nucleating steam based on classical nucleation theory with a new approach for the interaction between the droplets and vapour phases. This method included the droplet heat, mass and momentum transfer models along with nucleation within complex flow systems such as in low pressure steam turbines.

Kermani and Gerber [74] presented a numerical model to calculate thermodynamic and aerodynamic losses in nucleating steam flows in a series of Laval nozzles with and without shock waves. It was shown that thermodynamic loss was slightly affected by shock strength while the aerodynamic losses are of the same magnitude as the thermodynamic loss in the case of very weak shocks.

2.4 Steam condensation in turbines

Steam condensation also happens in steam turbines, especially in the cascades and turbine blades in the last stage of the low pressure (LP) turbine. It affects the flow field of turbines due to mechanical and thermodynamics effects and leads to additional loss. Moore and Sieverding [75] showed that an increase in absolute wetness level of about 1% will reduce the turbine efficiency by about 0.5%

compared with dry steam operation. Therefore, many researches have conducted an analysis of condensation phenomena and corresponding losses occurring in steam turbines either by experiments or numerical simulations. Some selected works which are based on CFD simulations are mentioned here.

Yamamoto et al. [76-78] presented CFD studies of condensing steam flows through multistage stator and rotor cascade channels in a LP steam turbine using both non-equilibrium and equilibrium condensation models. They suggested that the unsteady flow calculation with the inlet wetness will achieve the most realistic flow field, simulating features observed in actual steam-turbine cascade channels.

Starzmann et al. [79, 80] presented numerical results for wet steam flow within a three stage LP steam turbine test rig; the performance of different theoretical models for nucleation and droplet growth were examined. It was shown that heterogeneous condensation is highly dependent on steam quality and for a turbine with high quality steam, a homogeneous theory appears to be the best choice. They also studied the effect of droplet size on the deposition characteristics of the last stage stator blade and the effect of inter-phase friction on the flow field. Their results showed that for small fog droplets, turbulent diffusion is the main deposition mechanism and if the droplets size is increased, inertial effects become more important.

In general, the nucleation phenomena and steam condensation process in steam turbines are similar to those which happens in steam ejectors. However, for the case in which condensation occurs on the turbine blade, results are more sensitive to turbulence modelling, conditions near the wall and in the wake region.

2.5 Mixing layer and jet mixing studies

An important process which affects the performance of ejectors is the mixing of the primary and secondary streams. When two uniform and nearly parallel streams with different velocities start to

mix, a mixing layer (also known as a free shear layer) forms at their interface. Growth of the mixing layer leads to the mass entrainment of the stream with lower velocity into the mixing layer. Parameters which affect the mixing layer growth rate include the velocity ratio of the two streams, the density ratio, compressibility effects and Reynolds number. Several investigations have been completed to study the effect of these parameters on the mixing layer spreading rate.

Brown and Roshko [81] performed experiments for plane turbulent mixing between two streams of different gases with large density differences. It was found that large changes of the density ratio across the mixing layer had a relatively small effect on the spreading angle. The strong changes in the growth of the mixing layer which were when one of the stream was supersonic were due to compressibility effects, not density effects. They provided a good assessment of mixing layer growth rate for density ratios between 1/7 and 7 and for velocity ratios between 0 and $\sqrt{1/7}$.

Dimotakis [82, 83] investigated spatial growth of mixing layers and highlighted the fact that a spatially growing shear layer generally entrains an unequal amount of fluid from each of the streams. With the aid of geometric and similarity considerations, he studied the role of large-scale flow structures in the entrainment of streams in the mixing layer and proposed a correlating equation for the spatial spreading of an incompressible mixing layer.

The effect of compressibility on the growth rate of mixing layers was first studied by Bogdanoff [84]. Papamoschou and Roshko [85] subsequently introduced convective Mach number (M_c) to correlate compressibility effects on mixing layer growth rate when it is normalized by its equivalent incompressible mixing layer growth rate. The convective Mach number is a Mach number with respect to a frame of reference travelling with the large scale structures in the flow. They concluded that the normalized mixing layer growth rate decreases with increase of convective Mach number due to the compressibility effects of the high speed flow.

Elliot and Samimy [86, 87] showed that not only did growth rate decrease with an increase in the convective Mach number, but turbulence quantities also decreased. They also conducted experiments to measure shear layer growth rate for M_c higher than those used in experiments reported in earlier literature. They demonstrated that the rates of both small scale and large scale mixing were reduced with increasing convective Mach number.

Slessor et al. [88] proposed a new shear layer growth rate compressibility parameter as an alternative to the convective Mach number. This parameter was different from the previously employed convective Mach number especially at extreme free stream density and speed of sound ratios. It was observed experimentally that shear layer growth rates were well represented by this new scaling parameter.

Among the works performed on constant pressure, worth mentioning are high speed (supersonic) axisymmetric jet mixing experiments carried out by Cutler and White [89], Cutler et al. [90, 91] and Clifton and Cutler [92]. The purpose of their studies was to provide data for validation of computational simulation tools. Their results showed the need for improvement of computational simulation capabilities, particularly for locations where the ratio of downstream distance from the nozzle exit and the nozzle exit diameter were higher than 4 ($x / D > 4$).

The case of axisymmetric, supersonic jet mixing is similar to the case in steam ejectors where the mixing occurs under turbulent and highly compressible conditions. Steam condensation in the primary nozzle makes the mixing process more complicated in ejectors due to the creation of two phased flow conditions. The strong pressure gradients in ejectors further complicates the configuration relative to that of supersonic jet mixing under nearly constant pressure conditions.

Al-Doori and Buttsworth [93] conducted an experiment and demonstrated the application of pitot pressure surveying to define the development of an axisymmetric steam jet. For this experimental work, there was no co-flowing secondary stream mixed with the steam jet and jet mixing took place

at approximately constant pressure. The free shear layer growth rate they calculated from the pitot pressure measurements was consistent with empirical results for compressible and planar mixing layers.

2.6 Conclusion

Many efforts have been made to investigate the physics of the complicated, supersonic fluid flow inside steam ejectors, to achieve a better performance and an optimum design for steam ejectors. From the published literature, it is concluded that operating conditions and geometric details of steam ejectors significantly affect the ejector performance as characterised by the entrainment ratio and compression ratio.

There are some general trends of improving entrainment ratio with increasing evaporator pressure and decreasing boiler pressure under choked mode operation, but definitive performance predictors have not been established. CFD shows potential to contribute, but models using wet steam are not understood well enough to be reliably used in all circumstances.

Steam ejector computational simulations using wet steam models can provide useful information on steam condensation and nucleation phenomenon in the primary nozzle. Such simulations can also be used to study the effect of wet steam flow behaviour on the ejector performance. However, further investigations need to be performed to explore the mixing of the primary and secondary streams under wet steam conditions.

Researchers have conducted experiments to investigate the jet mixing process and mixing layer growth rate using different techniques, but mostly this has been performed in planar configurations. In order to connect the conclusions to steam ejector applications, more contributions need to be made to study these parameters in a relevant axisymmetric geometry, that of a co-flowing steam jet.

Ejector primary nozzle simulations using the wet steam model which are presented in the literature, investigated the effect of steam condensation on flow characteristics along the nozzle centreline. The

simulations show that condensation phenomenon changes steam properties at the nozzle exit relative to ideal gas simulations. However, no research particularly explored the effect that condensation has on the mixing layer growth rate which affects the ejector entrainment ratio. The values of static pressure and momentum flux which changes at the end of the primary nozzle due to steam condensation play important roles in mixing layer development. The published paper presented in Chapter 3 discusses these issues for the first time.

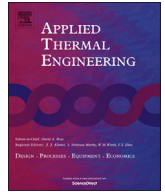
Wet steam simulations of ejectors in the literature give a higher entrainment ratio and higher critical back pressure compared with ideal gas simulations. However, the reasons for the higher performance parameters in the wet steam case are not clearly explained in the prior literature. A research study was performed to clarify why simulations using wet steam modelling yield higher ejector performance relative to ideal gas modelling. The published paper presented in Chapter 4 discusses the origins of the higher simulated performance under wet steam assumptions.

Ejector entrainment ratios are influenced by two factors: pressure driven effects and the mixing process between the primary and secondary streams. In the reviewed literature, there was no work that identified the relative significance of each factor. A computational simulation study was carried out on a representative steam ejector to specify the contribution of mixing and pressure driven effects to the ejector entrainment ratio under different operating conditions. Results from this study are presented in Chapter 5 in the format of a published paper.

Turbulent mixing plays a pivotal role in the performance of ejectors but there is no consensus in the existing literature on the most accurate turbulence model to use for ejector simulations. Furthermore, the experimental results available in the literature do not provide direct data on the mixing of wet steam jets in steam ejectors. An experimental investigation was therefore conducted to measure the pitot and static pressures within a supersonic steam jet which mixes with a low pressure co-flowing secondary stream. The purpose of this work is to provide data that can be used for validation of computational simulations or other modelling of ejectors. Chapter 6 describes these experimental

results and also presents some preliminary computational simulations using the $k - \omega$ turbulence model.

Chapter 3 Flow characteristics in the primary nozzle



Ejector primary nozzle steam condensation: Area ratio effects and mixing layer development



Kavous Ariafar^{a,*}, David Buttsworth^a, Navid Sharifi^b, Ray Malpress^a

^a School of Mechanical and Electrical Engineering, University of Southern Queensland, Australia

^b Department of Aerospace Engineering, Amirkabir University of Technology, Tehran, Iran

HIGHLIGHTS

- Primary nozzle momentum flux is virtually the same for ideal gas and wet steam models.
- Higher nozzle exit velocities but lower Mach numbers result from the wet steam model.
- Mixing layer growth correlations can be applied to primary nozzle exit flow.
- Increased entrainment simulated for wet steam ejectors is explained by mixing rates.

ARTICLE INFO

Article history:

Received 4 January 2014

Accepted 16 June 2014

Available online 26 June 2014

Keywords:

Steam ejector

Nozzle

Steam condensation

Nucleation

CFD

Mixing

ABSTRACT

Recent ejector simulations based on wet steam modeling give significantly different performance figures relative to ideal gas modeling, but the origins of such differences are not clear. This paper presents a numerical investigation of flow in the primary nozzle of a steam ejector to further explore the differences between ideal gas and wet steam analysis of ejector flows. The wet steam modeling was first validated using primary nozzle surface pressure data from three experiments reported in the literature. Ejector primary nozzles with area ratios (AR) of 11, 18 and 25 were then simulated using wet steam and ideal gas models. The wet steam simulations show that nozzle static pressures are higher than those for ideal gas model, and in the AR = 25 case, the static pressure is larger by a factor of approximately 1.7. In contrast, no significant difference exists between the nozzle momentum flux for both ideal gas and wet steam models, except the vicinity of the nozzle throat where nucleation occurs. Enhanced mixing between primary and secondary streams, which arises because primary stream condensation reduces compressibility in the mixing layer, is proposed as an explanation of the increased entrainment ratio observed in recent wet steam ejector simulations.

© 2014 Elsevier Ltd. All rights reserved.

1. Introduction

Supersonic steam ejectors are widely used in a large number of industries that use steam as their heating medium or as a power generating utility. They are devices which utilize the energy of a high pressure fluid (the primary stream) to move a low pressure fluid (the secondary stream) and enable it to be compressed to a higher pressure. Their action is akin to a vacuum pump but without using any moving parts. They are known for simple construction, easy installation and low capital costs. Steam ejectors essentially consist of four main parts: a primary nozzle, a mixing chamber, a

constant area and a diffuser. Fig. 1 shows a schematic of a steam ejector illustrating the different parts, and an idealized description of ejector operation is presented below.

The function of the nozzle is to convert the high pressure and low velocity steam delivered to the nozzle into a very high velocity flow with a static pressure lower than that of the low pressure secondary stream. The velocity of steam as it enters the nozzle increases in the converging portion and reaches sonic velocity at the nozzle throat. Beyond the nozzle throat, the velocity of steam becomes supersonic and further increases until the end of the nozzle where a very low pressure region is created. This vacuum region causes the secondary stream to enter the mixing chamber where it mixes with the primary jet leaving the nozzle. Mixing of the primary and secondary streams continues and within the constant area, the mixture undergoes a sudden pressure rise through the action of one or more shock waves which decelerate

* Corresponding author.

E-mail addresses: Kavous.ariafar@usq.edu.au, kavous.ariafar@gmail.com (K. Ariafar).

Nomenclature

Latin letters

A	stream-wise cross-sectional area of the nozzle, m^2
A_t	cross-sectional area of the nozzle throat, m^2
a	speed of sound, m/s
B	virial coefficients, m^3/kg
b	nozzle throat diameter, m
C	virial coefficients, m^6/kg^2
C_μ	viscosity related constant
c_p	isobaric heat capacity, $J/kg\ K$
E	total energy, J
h_{lv}	specific enthalpy of vaporization, J/kg
I	nucleation rate, # droplets/ $m^3.s$
K_b	Boltzmann constant 1.3807×10^{-23} , J/K
k	turbulent kinetic energy, J/kg
M	molecular mass, kg/mol
M_c	convective Mach number
P	pressure, Pa
P_0	nozzle inlet static pressure, Pa
q_c	condensation coefficient
R	gas constant, $J/kg\ K$
r	critical droplet radius, m
\bar{r}	droplet average radius, m
S	x stream-wise distance measured from the nozzle throat, m
Src	source term

s	super saturation ratio
sgn	sign function
T	static temperature, K
T_d	droplet temperature, K
u	velocity, m/s
V_d	average droplet volume, m^3
w	nozzle width, m

Greek letters

α	thermal conductivity, $W/m\ K$
β	liquid mass fraction
Γ	mass generation rate, $kg/m^3\ s$
γ	ratio of specific heats
δ	growth rate of mixing layer
ϵ	turbulent dissipation rate, $J/kg\ s$
η	droplet number density, $1/m^3$
θ	non-isothermal correction factor
μ	dynamic viscosity, $N\ s/m^2$
μ_t	turbulent viscosity, $N\ s/m^2$
Π_c	compressibility parameter
ρ, ρ_l, ρ_v	mixture density, liquid density, vapor density, kg/m^3
σ	droplet surface tension, N/m
τ_{ij}	stress tensor
ϕ	velocity ratio
ψ	turbulent Prandtl number
Ω	density ratio

the flow to a subsonic speed. Further deceleration occurs in the subsonic diffuser portion of the ejector and at the exit of the diffuser, the fluid reaches the design outlet pressure.

Keenan and Neumann were the first to establish a theory of ejector operation based on one dimensional gas dynamics as a basis for the design of ejectors [1]. This theory was then modified to include loss coefficients in different parts of the ejector by Eames et al. [2]. Munday and Bagster [3] proposed a theory in which the existence of an aerodynamic throat was assumed for the secondary stream and Huang et al. [4] continued this approach, assuming the secondary stream throat location is within the constant area section of the ejector. Such a gas dynamic modeling approach was extended by Zhu et al. [5] to accommodate a variation in the axial velocity across the primary and secondary streams. According to such gas dynamic modeling, which is based on the assumption of ideal gas behavior, the static pressure at the exit of the primary nozzle is of critical importance because it dictates the cross-sectional area available for the choked secondary stream.

Recently, computational fluid dynamics (CFD) has been applied to the design and optimization of ejectors because of the ability of CFD to accurately simulate the flow field inside complex geometries. For example, Riffat and Omer [6] and Da-Wen and Eames [7] studied the effect of nozzle position on ejector performance based on both constant pressure and constant area ejector designs. They

found that the performance of the ejector was determined by the distance at which the primary and secondary streams become completely mixed. The distribution of static pressure along ejectors was studied numerically and experimentally by Sreevirakul et al. [8,9]. The ideal gas assumption was invoked for these CFD simulations of ejectors, even in the studies which considered water vapor as the working fluid.

The conditions under which water vapor flows begin to condense is already quite well established and such conditions often occur in steam ejectors. Droplet nucleation and the subsequent development of condensation result in a number of energy transfers which cannot be accurately simulated by assuming that the steam behaves as a perfect gas. Therefore, recent CFD simulations of steam ejector performance have incorporated droplet nucleation and condensation models. Yang and Shen [10] simulated the spontaneous condensation of steam in a 2-D model of a Laval nozzle based on the classical nucleation theory and the Virial-style equation of state and observed the physical features associated with the condensation front. Wang et al. [11,12] investigated condensation in the nozzle of the ejector and its effects on the ejector performance, comparing simulations with the experimental ejector data available in the literature, concluding that wet steam modeling offers improved simulation of ejector performance. Sharifi et al. [13] also simulated steam ejector operation using a model for homogenous nucleation and observed that the primary flow mass flow rate was almost the same as for the case of the ideal gas simulations, but the ejector entrains more secondary flow and increases the critical pressure of the ejector relative to the ideal gas simulations.

In an effort to explain why simulations using wet steam modeling yield better ejector performance relative to ideal gas modeling, this paper presents results from the numerical simulation of three different area ratio nozzles, representative of primary nozzles used in steam ejectors. The axial distribution of key primary stream parameters such as the static pressure and momentum flux which affect ejector performance are discussed to

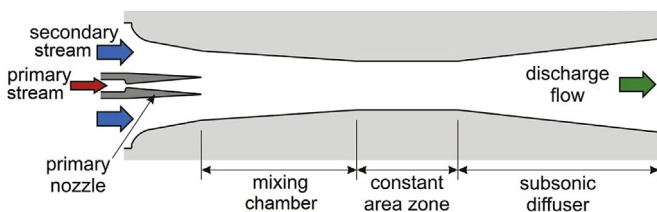


Fig. 1. Ejector cross-section illustrating the different zones.

emphasize the role which condensation plays in ejector performance.

2. Mathematical model

In the present study, the steam behavior is governed by the Eulerian–Eulerian approach and two phase flow is modeled using the compressible Navier–Stokes conservation equations together with two additional transport governing equations available in the wet steam model in FLUENT for the liquid phase mass fraction (β) and the number of liquid droplets per unit volume (η). To reduce the complexity of the two phase flow model, assumptions of no slip between the phases, and negligible volume of the condensed liquid are used since droplet sizes are typically very small and negligible interaction between the droplets is expected.

2.1. Governing equations

The governing equations can be written in compact Cartesian form according to the laws of conservation of mass, momentum and energy:

$$\frac{\partial \rho}{\partial t} + \frac{\partial}{\partial x_i}(\rho u_i) = 0 \quad (1)$$

$$\frac{\partial}{\partial t}(\rho u_i) + \frac{\partial}{\partial x_j}(\rho u_i u_j) = -\frac{\partial P}{\partial x_i} + \frac{\partial \tau_{ij}}{\partial x_j} \quad (2)$$

$$\frac{\partial}{\partial t}(\rho E) + \frac{\partial}{\partial x_i}(u_i(\rho E + P)) = \vec{\nabla} \cdot \left(\alpha_{\text{eff}} \frac{\partial T}{\partial x_i} + u_j(\tau_{ij}) \right) \quad (3)$$

with

$$\tau_{ij} = \mu_{\text{eff}} \left(\frac{\partial u_i}{\partial x_j} + \frac{\partial u_j}{\partial x_i} \right) - \frac{2}{3} \mu_{\text{eff}} \frac{\partial u_k}{\partial x_k} \delta_{ij} \quad (4)$$

2.2. Liquid phase mass fraction transport equation

The first additional transport equation governing the mass fraction of the condensed liquid phase is written as [14]:

$$\frac{\partial(\beta \rho)}{\partial t} + \nabla \cdot (\rho \beta \vec{u}) = \Gamma \quad (5)$$

where Γ is the mass generation rate due to condensation and evaporation, which is correlated with the nucleation rate I (number of new droplets per unit volume per second) and the growth or demise of these droplets [14]:

$$\Gamma = \frac{4}{3} \pi \rho_l I r^{*3} + 4 \pi \rho_l \eta \bar{r}^2 \frac{\partial \bar{r}}{\partial t} \quad (6)$$

In the above expression, r^* is the critical droplet radius; above this value the droplet will grow and below this value, the droplet will evaporate. The critical droplet radius is written as [15]:

$$r^* = \frac{2\sigma}{\rho_l R T \ln(s)} \quad (7)$$

Where s is the super saturation ratio and is defined as the ratio of vapor pressure to the equilibrium saturation pressure:

$$s = \frac{P}{P_{\text{sat}}(T)} \quad (8)$$

2.3. Nucleation rate equation

In this model, the homogeneous nucleation theory explains the creation of a liquid phase in the form of droplets from a superheated phase in the absence of foreign particles. The estimation of the size of created droplets during the nucleation in wet steam flow is very difficult. The classical theory of nucleation to calculate the number of liquid droplets is written as [15]:

$$I = \frac{q_c}{(1 + \theta)} \left(\frac{\rho_v^2}{\rho_l} \right) \sqrt{\frac{2\sigma}{M^3 \pi}} \exp\left(-\frac{4\pi r^{*2} \sigma}{3K_b T} \right) \quad (9)$$

The term q_c is the condensation coefficient which was thought to have a value around 0.02–0.03 based on early experiments [16], but it is now believed that this coefficient takes a value close to unity [17] and this is the case in the FLUENT implementation. The term θ is a non-isothermal correction factor and is written as [15]:

$$\theta = \frac{2(\gamma - 1)}{\gamma + 1} \left(\frac{h_{lv}}{RT} \right) \left(\frac{h_{lv}}{RT} - 0.5 \right) \quad (10)$$

where γ is the ratio of specific heats which is taken as 1.32.

The wet steam density can be determined from the vapor density ρ_v and liquid phase mass fraction β :

$$\rho = \frac{\rho_v}{1 - \beta} \quad (11)$$

2.4. Droplet growth rate

The size of droplets is affected by two mechanisms: the transfer of mass from the vapor to the droplets and the transfer of heat from the droplets to the vapor due to the latent heat. The droplet growth rate can be written as [14]:

$$\frac{\partial \bar{r}}{\partial t} = \frac{P}{h_{lv} \rho_l \sqrt{2\pi RT}} \frac{\gamma + 1}{2\gamma} c_p (T_d - T) \quad (12)$$

2.5. Droplet density transport equation

The second additional transport equation estimates the growth of droplet numbers per unit volume of steam and is described as [14]:

$$\frac{\partial(\rho \eta)}{\partial t} + \nabla \cdot (\rho \eta \vec{u}) = \rho I \quad (13)$$

In this equation η is the number of droplets per unit volume and can be written as:

$$\eta = \frac{\beta}{(1 - \beta) V_d (\rho_l / \rho_v)} \quad (14)$$

with V_d being the average droplet volume which is assumed to be sphere with average radius of \bar{r} .

2.6. Equation of state

The steam equation of state which relates the pressure to the vapor density and the temperature is given by Ref. [18]:

$$P = \rho_v R T \left(1 + B \rho_v + C \rho_v^2 \right) \quad (15)$$

where B and C are the second and the third Virial coefficients given by the function of temperature. This Virial formulation is claimed to

be reliable for both high and low pressure conditions ranging from 0.01 to 100 bar and temperature range of 273.15–1000 K [10].

2.7. Turbulence model

A two equation turbulence model was applied to the whole flow domain based on the $k-\varepsilon$ turbulence hypothesis. The main governing equations for the realizable $k-\varepsilon$ model used in this work are described by Ref. [19]:

$$\frac{\partial}{\partial t}(\rho k) + \frac{\partial}{\partial x_i}(\rho k u_i) = \frac{\partial}{\partial x_j} \left[\left(\mu + \frac{\mu_t}{\psi_k} \right) \frac{\partial k}{\partial x_j} \right] + Src_k \quad (16)$$

$$\frac{\partial}{\partial t}(\rho \varepsilon) + \frac{\partial}{\partial x_i}(\rho \varepsilon u_i) = \frac{\partial}{\partial x_j} \left[\left(\mu + \frac{\mu_t}{\psi_\varepsilon} \right) \frac{\partial \varepsilon}{\partial x_j} \right] + Src_\varepsilon \quad (17)$$

where k is the turbulent kinetic energy, ε is the turbulent dissipation rate, Src is the source term, ψ is the turbulent Prandtl number and μ_t is the turbulent viscosity in the form of:

$$\mu_t = \rho C_\mu \frac{k^2}{\varepsilon} \quad (18)$$

where C_μ is a viscosity-related constant with a value between 0.0845 and 0.09. A benefit of this model compared to the standard $k-\varepsilon$ model is that it more accurately predicts the spreading rate of both planar and round jets [19] which will be important for future work which aims to examine the mixing downstream of the primary nozzle exit.

2.8. Numerical solution procedure

The governing equations were solved numerically using a commercial CFD code, FLUENT 14.5 which is based on the control volume method to approximate the governing equations as algebraic equations. A second order upwind scheme was selected to achieve a high order of accuracy at cell faces through a Taylor series expansion of the cell centered solution. The nonlinear governing equations were solved using the coupled implicit solver and the standard wall function was applied near the walls. Convergence of the solution was assumed when two criteria were satisfied:

- the relative difference of mass flow rate between the inlet and outlet boundaries of less than 10⁻⁷; and
- every type of calculated residual error must be less than 10⁻⁶.

3. Validation of the numerical method

To validate the wet steam simulation method, pressure measurements from two experiments reported by Moore et al. [20] and one experiment reported by Bakhtar et al. [21] are considered. Values of absolute pressure are reported throughout the present work. From the Moore et al. [20] work, the geometries of nozzles A and B were used, with the specified inlet boundary conditions: stagnation pressure of 25 kPa and stagnation temperature of 354.6 K for nozzle A, and 357.6 K for nozzle B. The saturation temperature at this pressure is 338.14 K. From the work of Bakhtar et al. [21], the third specified geometry was simulated with the specified inlet boundary conditions: Stagnation pressure of 87 kPa and stagnation temperature of 385 K and the saturation temperature at this pressure is 368.9 K. Since all the nozzles were rectangular in cross section, a 2-D solver was selected for simulation. For each case, three different mesh densities were trialed to confirm

results were mesh independent. Geometrical details of these nozzles are presented in Fig. 2 and Table 1.

In the experiments of Moore et al. [20] and Bakhtar et al. [21], static pressure was measured at various points along the nozzle axis. Simulations of the nozzle static pressures from the present work are compared with their respective experimental results in Fig. 3. As it can be observed the simulated static pressures for all cases along the nozzle centerline are in a good agreement with the experimental data. Upstream of the nozzle throat, the results of the wet steam simulations shown in Fig. 3 closely follow simulations using an ideal gas model.

At each nozzle location, the difference between the simulated and measured static pressures, normalized by the measured static pressure has been identified and defined as the relative error and Table 2 shows the average and maximum values. Across the three simulated cases, the average relative error is -8.2% with the largest error magnitude being 19%. In all three cases, the relative errors are negative, indicating that the simulations consistently underestimate the measured static pressures, as observed in Fig. 3. Note however, that in the simulation of the Bakhtar et al. [21] case, the pressures in the subsonic contraction region closely match the experimental data, and yet in the supersonic portion of the nozzle, the static pressures are still underestimated by the simulations.

Systematic errors may have arisen due to: (1) simulation of the nozzles using a 2D planar arrangement whereas the actual experimental configurations were of finite width; (2) development of boundary layers from zero thickness at the start of the nozzle in the simulations whereas finite thickness boundary layers would have been present at the nozzle inlet in the experiments; (3) possible errors in static pressure or flow temperature measurements in the experiments; and (4) wet steam modeling approximations.

The fact that simulations of the static pressures in these experiments are within about 10% of the measured data on average indicates that in the following work, where comparisons are made between wet steam and ideal gas simulations, effects relating to static pressure differences larger than 10% can be considered reliable.

4. Geometry and boundary conditions

The dimensions of a particular ejector's primary nozzle are presented in Fig. 4(a) with the grid configuration of the mesh elements used in the present simulations shown in Fig. 4(b). The simulations in the present work were axisymmetric (the mesh illustrated in Fig. 4(b) has been reflected about the axis for the purpose of presentation).

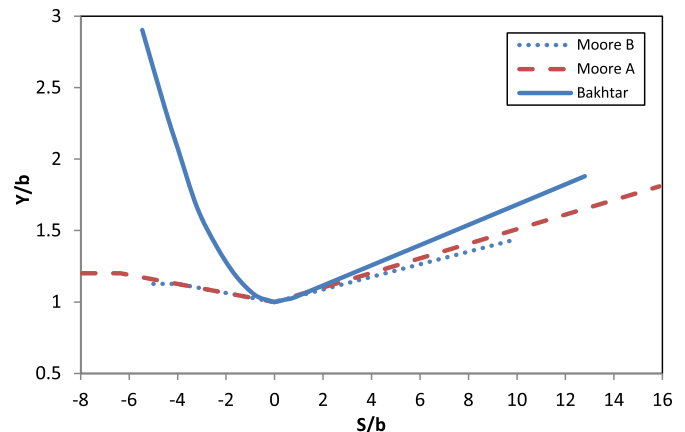


Fig. 2. Geometry of nozzles simulated in validation work.

Table 1
Geometry of nozzles simulated in validation work.

Moore A	S/b	−7.94	−6.35	0	15.87				
$b = 31.5$ mm	Y/b	1.201	1.201	1	1.809				
width = 152 mm									
Moore B	S/b	−5	−4	0	10				
$b = 50$ mm	Y/b	1.127	1.127	1	1.44				
width = 152 mm									
Bakhtar	S/b	−5.456	−4	−3.2	−2.4	−1.6	0	0.824	12.8
$b = 12.5$ mm	Y/b	2.904	2.08	1.664	1.392	1.184	1	1.032	1.88
width = 12.5 mm									

In order to check the sensitivity of the results to the mesh density, three different mesh densities were produced: the coarse mesh density with 4550 elements, the medium with 6510 and the fine with 10440 elements. The simulation results were very similar

for medium and fine level (7% difference for nozzle exit Mach number), hence the medium mesh was selected with consideration of the CPU cost and simulation time. At the simulated nozzle inlet, a pressure inlet boundary condition was specified with a value of 270 kPa, and a temperature of 403 K, corresponding to saturated vapor conditions. At the exit plane, an extrapolate outlet boundary condition was selected with an initial pressure of 1.6 kPa, equal the pressure of the secondary stream, although FLUENT ultimately calculates the necessary pressure through an extrapolation.

The area ratio for geometry shown in Fig. 4 is 18 and in order to investigate the effect of area ratio on flow characteristics, two more nozzles with area ratios (ARs) of 11 and 25 were selected for simulation. Since the purpose of the present work is to investigate primary stream parameters such as static pressure, momentum flux and Mach number at the nozzle exit, different values of these parameters are investigated by changing the area ratio within sensible limits that could be achieved in practice, considering the prevention of over- and under-expansion issue at the nozzle exit. Table 3 specifies the geometry of each simulated nozzle. The convergent portion of each nozzle was identical. Nozzle flow simulations were performed using the wet steam model, and for comparison, an ideal gas model for steam was also used.

5. Results and discussion

5.1. Wet steam characteristics

Fig. 5 shows the variation of subcooling level and nucleation rate I along the nozzle centerline for the nozzle with AR 25. Subcooling is defined as the difference between the local vapor and saturation temperature at the same pressure meaning that the subcooling temperature difference is $\Delta T = T_{\text{sat}}(P) - T_g$. Nucleation of liquid droplets starts at an axial location upstream of the nozzle throat and reaches its maximum at axial location of 0.067. At this location significant liquid droplet generation occurs, approximately 10^{24} droplets per second per unit volume. The vapor phase starts to condense after significant subcooling occurs (around 13 K). In these simulations, the maximum subcooling reached is about 34 K. After the nucleation peak, the subcooling level decreases rapidly to near equilibrium conditions. It can be seen the highest value of nucleation happens at the same axial location as the maximum subcooling level.

Fig. 6 shows the distribution of liquid mass fraction or wetness fraction (β) and liquid mass generation rate (I) along the nozzle axis. The liquid phase generation starts at the point of nucleation and the sharp rise in wetness fraction at this location reflects the rapid growth of the droplets after the nucleation point. It is also evident that the wetness fraction smoothly increases along the nozzle axis. As the expansion of steam through the nozzle proceeds, the subcooling rises smoothly while the steam remains dry (zero value for wetness fraction), but when nucleation is initiated (the nucleation rate I is non-zero), the liquid mass generation rate increases rapidly and the liquid mass fraction grows from zero.

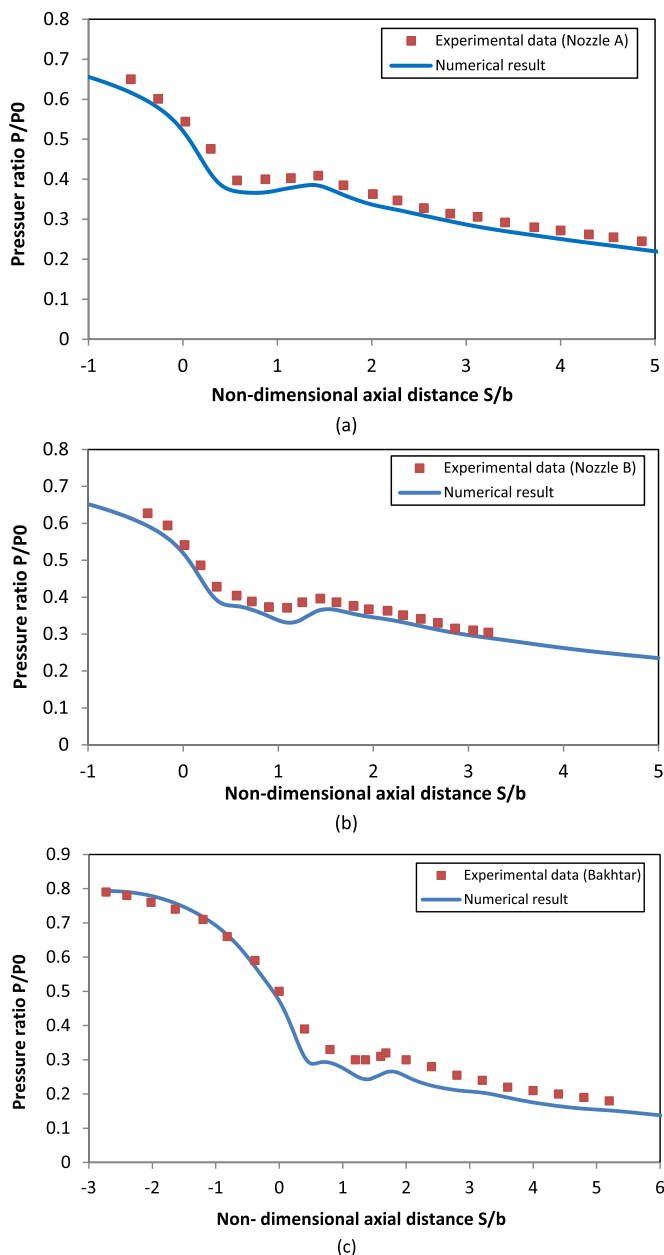


Fig. 3. Comparisons between simulation results and experimental data: (a) Moore et al. [20] Nozzle A (b) Moore et al. [20] Nozzle B; (c) Bakhtar et al. [21] third configuration.

Table 2
Representative errors in the simulation of measured pressures.

Experiments	$\left(\frac{\Delta P_{\text{meas}}}{P}\right)_{\text{average}}$	$\left(\frac{\Delta P_{\text{meas}}}{P}\right)_{\text{max}}$
Nozzle A, Moore et al. [20]	−7.0%	−12.0%
Nozzle B, Moore et al. [20]	−6.5%	−11.9%
Bakhtar et al. [21]	−11.1%	−19.0%
Average relative error	−8.2%	−14.3%

5.2. Pressure distribution

Fig. 7 shows the pressure distribution along the axis of the nozzle for the ideal gas model for the area ratio (AR) of 25 and the wet steam model for selected area ratios. It is observed that after the nucleation peak (indicated by vertical dashed line), the static pressure values for the wet steam model are higher than those for the ideal gas model. The release of latent heat associated with the condensation process tends to maintain the static pressure at an elevated value relative to the ideal gas case, and this effect continues until the end of the nozzle. For AR of 25, the values of static pressure at the outlet of the nozzle for ideal gas and wet steam models are 999.33 Pa and 1711.73 Pa, respectively, and this is a very significant difference, given the validation work indicated relative errors of around 10%. Fig. 7 also demonstrates that the pressures within the different nozzles are essentially a function of area ratio as the results collapse onto virtually the same line when plotted on the area ratio axis.

For the wet steam model, the AR 25 nozzle produces the lowest static pressure at the outlet, as is the case for the ideal gas analysis. Lower nozzle exit static pressures at a given primary nozzle area ratio are advantageous, according to the common ideal gas modeling of ejectors [3–5], because lower nozzle exit static pressures cause higher secondary stream flow rates. This is because choking of the secondary stream can be achieved with less additional expansion of the primary flow downstream of the nozzle exit, allowing additional flow cross-sectional area for the secondary stream. However, lower nozzle exit pressures are not essential for the generation of higher entrainment ratios as demonstrated by recent ejector simulations using wet steam modeling [12,13].

5.3. Temperature distribution

Fig. 8 shows the static temperature profile along the nozzle axis for the ideal gas model and the wet steam modeling of the three nozzles. After the nucleation point, the vapor static temperature rapidly increases for the wet steam model because of the release of

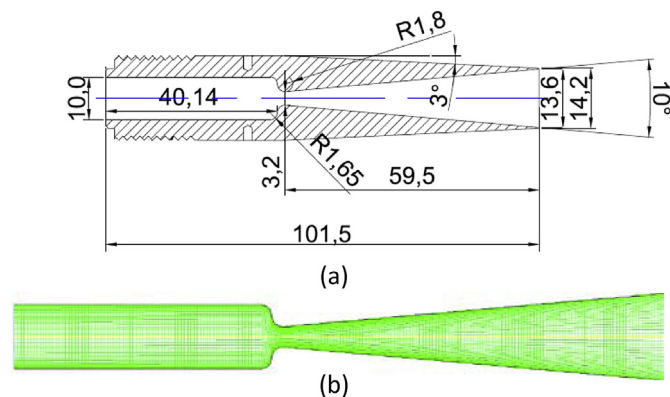


Fig. 4. (a) Primary nozzle geometry [22]; (b) computational grid.

Table 3
Geometry of the simulated nozzles.

	Divergent length (mm)	Nozzle throat diameter (mm)	Exit diameter (mm)	Area ratio
Case 1	59.5	3.2	10.6	11
Case 2	59.5	3.2	13.6	18
Case 3	59.5	3.2	16	25

latent heat associated with the growth of the droplets. The rise in the temperature after the condensation front is made more visible using an inset in Fig. 8. After the development of this condensation front, the difference between temperature values for the ideal gas and wet steam models continues to increase, with the static temperature in the wet steam simulations decreasing more gradually than in the ideal gas simulation. For the AR of 25, the steam temperature at the outlet of the nozzle is 111.61 K based on the ideal gas model which is not realistic, whereas the nozzle outlet static temperature for the same AR is 281 K for the wet steam model.

5.4. Mach number distribution

The Mach number variation along the centerline of the nozzle is presented in Fig. 9 for both ideal gas and wet steam modeling cases. For AR of 25, the ideal gas steam flow smoothly accelerates within the converging part of the nozzle and passes the sonic condition at the nozzle throat, and continues accelerating up to $M = 4.19$ at the nozzle outlet. According to the wet steam model, nucleation peaks at $M \approx 1.5$, just downstream of the nozzle throat. The release of latent heat follows the development of the liquid mass fraction (as illustrated in Fig. 6), and increases the local static temperature (Fig. 8) and thus, the speed of sound, causing substantially lower Mach numbers along the length of the nozzle in each of the wet steam cases. At the end of the AR 25 nozzle, $M = 3.304$, substantially lower than in the ideal gas case.

5.5. Momentum flux distribution

Fig. 10 presents the momentum flux distribution along the nozzle axis for both ideal gas and wet steam models. In the present work, the term “momentum flux” describes the quantity ρu^2 . It can be seen that for the AR 25 nozzle, there is no significant difference in the momentum flux profile between ideal gas and wet steam models: the peak which occurs just downstream of the nozzle throat has only a slightly higher value for the ideal gas model, and the nozzle exit values are virtually identical for both ideal gas and wet steam cases (their values are 22739.8 and 22659.3 Pa for ideal gas and wet steam, respectively). The momentum flux of the primary stream affects the capacity of an ejector to operate with

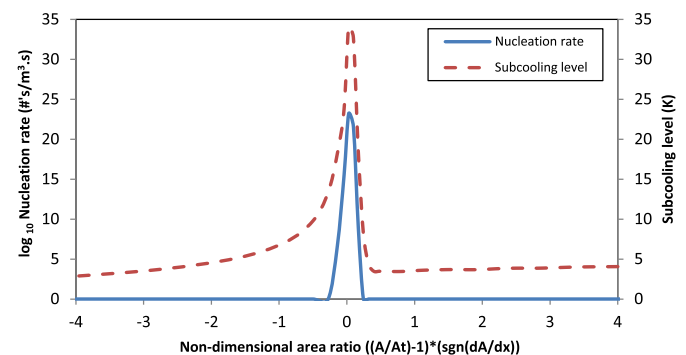


Fig. 5. Variations of nucleation rate I and subcooling level.

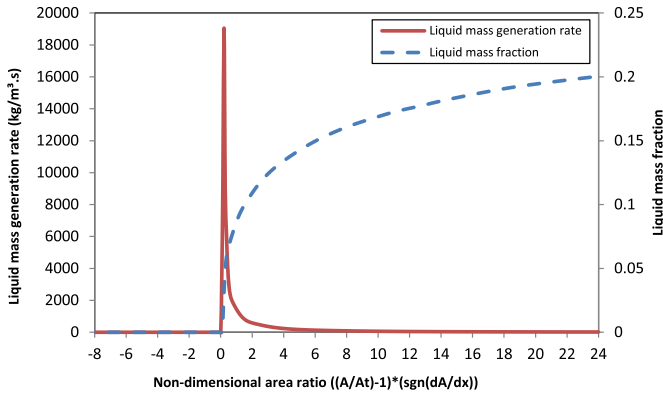


Fig. 6. Values for Liquid mass fraction (β) and liquid mass generation rate (Γ).

elevated back pressures. Of the three nozzles, the AR 11 nozzle has the highest value of momentum flux of 47486.8 Pa, suggesting the best back-pressure performance, but perhaps at the expense of entrainment ratio since the static pressures will be highest in this case.

5.6. Velocity and speed of sound distributions

Fig. 11 shows the velocity and speed of sound distributions along the nozzle axis for both ideal gas and wet steam models. After the nozzle throat, both velocity and speed of sound are larger for the wet steam model when compared to the ideal gas case. The increase of the speed of sound is due to the rise in the steam temperature because of the release of latent heat. The relative increase for the speed of sound is higher than that for the velocity and this fact results in the reduction of Mach number for the wet steam model relative to the ideal gas case, as shown in Fig. 9. For AR of 25, the values of velocity and speed of sound at the nozzle outlet for the ideal gas model are 1083.17 m/s and 258.63 m/s, respectively which gives a Mach number of 4.19 (Fig. 9). The corresponding values of velocity and speed of sound for the wet steam model are 1167.52 m/s and 353.3 m/s, resulting in a lower Mach number of 3.3 at the nozzle outlet.

6. Discussion

The present work demonstrates that the simulated wet steam nozzle exit static pressures are substantially higher than the ideal gas values and recent ejector simulations using a similar wet steam

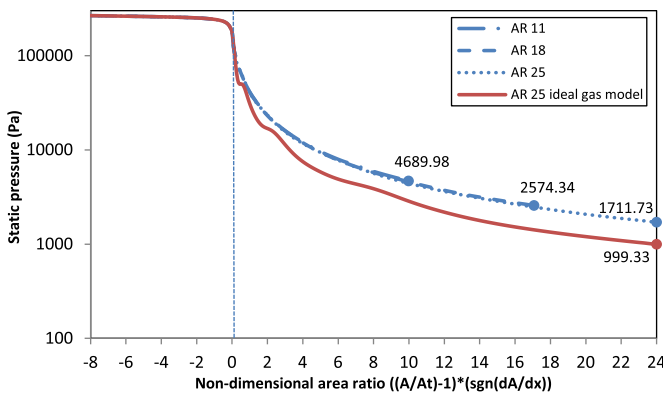


Fig. 7. Static pressure distributions along the axis of the nozzles obtained using ideal gas and wet steam models. Terminal static pressure values for the three wet steam nozzle simulations are indicated by the numbers on the graph. The location of the nucleation peak is indicated by the vertical broken line.

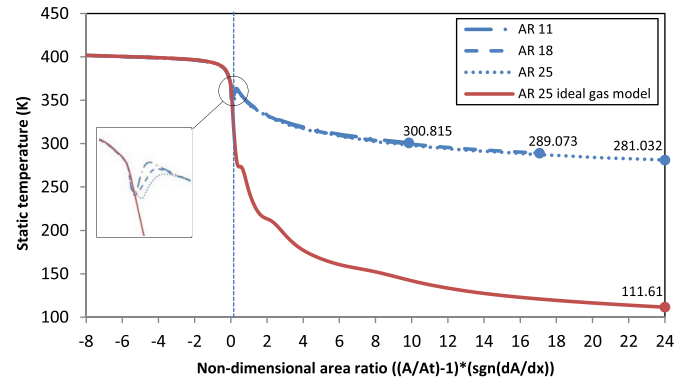


Fig. 8. Static temperature distributions along the axis of the nozzles obtained using ideal gas and wet steam models. Terminal static temperature values for the three wet steam nozzle simulations are indicated by the numbers on the graph. The location of the nucleation peak is indicated by the vertical broken line.

model [12,13] indicate higher entrainment ratios than in the ideal gas case. However, conventional gas-dynamic models for ejector operation [3,4,5] indicate reduced entrainment of the secondary stream should occur when the primary nozzle exit static pressure increases. Although such ideal gas models have successfully simulated ejector performance in a number of cases, the static pressure is not the only parameter affecting entrainment of the secondary stream into the ejector duct. The following concepts, which offer an explanation for the higher entrainment ratio obtained in the simulation of ejectors using a wet steam model, has not previously been presented in the literature.

On the assumption that computational simulations calculate the mixing rates correctly under the compressible flow conditions, the difference between the simulated entrainment ratio for ejectors based on ideal gas and wet steam models can be explained by empirical correlations for the mixing rates. The nozzle exit conditions for the ideal gas and wet steam models are sufficiently different to generate detectably different rates of mixing which can affect an ejector's capacity to entrain the secondary stream.

As illustrated in Fig. 12, the mixing of primary and secondary streams starts at the nozzle exit, where they first meet, and leads to the development of a mixing layer with thickness δ . Any change in the values of primary stream's parameters at the nozzle exit such as Mach number, velocity and speed of sound can affect the mixing

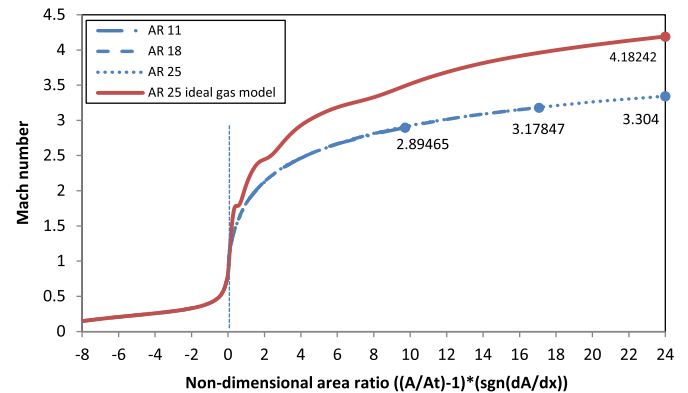


Fig. 9. Mach number distributions along the axis of the nozzles obtained using ideal gas and wet steam models. Terminal Mach number values for the three wet steam nozzle simulations are indicated by the numbers on the graph. The location of the nucleation peak is indicated by the vertical broken line.

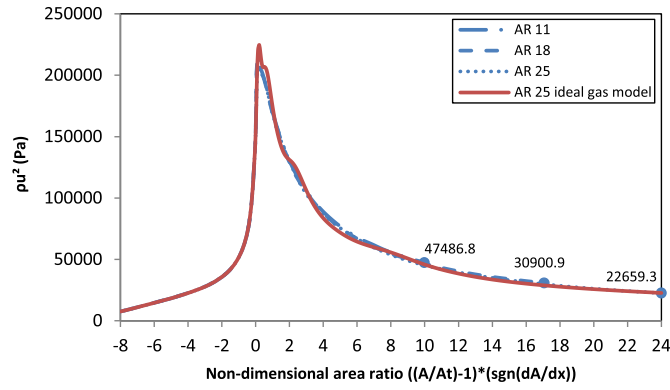


Fig. 10. Momentum flux distributions along the axis of the nozzles obtained using ideal gas and wet steam models. Terminal momentum flux values for the three wet steam nozzle simulations are indicated by the numbers on the graph.

rate which can lead to a change in the value of the entrainment ratio.

Compressibility effects in turbulent mixing shear layers act to reduce the mixing rate of two streams relative to equivalent incompressible cases and these effects have been correlated using the convective Mach number [23],

$$M_c = \frac{\Delta u}{a_1 + a_2} \tag{19}$$

where Δu is the velocity difference of two streams across the mixing layer and a_1 and a_2 are the speeds of sound on either side of the mixing layer. Another correlating parameter was suggested by Slessor et al. [24]

$$\Pi_c = \max \left[\frac{\sqrt{\gamma_i - 1}}{a_i} \right] \Delta u \tag{20}$$

where i refers to either primary or secondary stream. Compressibility effects on the growth rate of the mixing layer was correlated [24] using the expression

$$\frac{\delta'}{\delta_0} = \left(1 + \alpha_0 \Pi_c^2 \right)^{-\beta_0} \tag{21}$$

The width of a fully-developed mixing layer δ increases linearly with streamwise distance (Fig. 12) so the growth rate of the

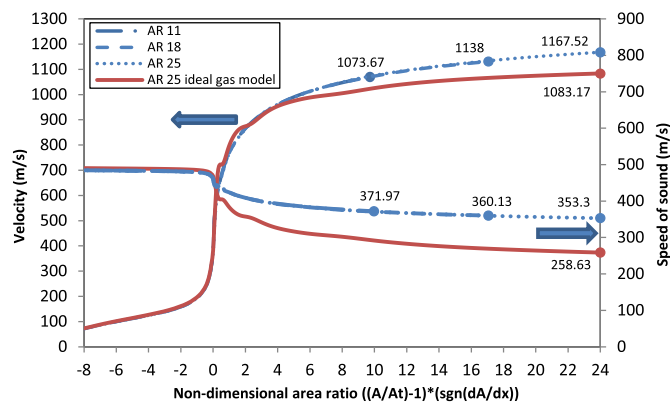


Fig. 11. Velocity and speed of sound distributions along the axis of the nozzles obtained using ideal gas and wet steam models. Terminal values are indicated by the numbers on the graph.

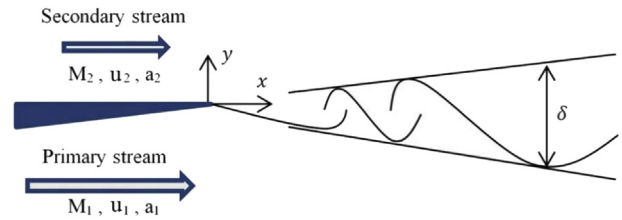


Fig. 12. Schematic of the mixing layer development.

compressible mixing layer δ' (which is defined as $d\delta/dx$) is constant. In the above expression, δ_0 is the growth rate of an incompressible mixing layer with the same density ratio and velocity ratio as the compressible case, and α_0 and β_0 are correlating parameters with approximate values of $\alpha_0 = 4$ and $\beta_0 = 0.5$.

The growth rate of the equivalent incompressible mixing layer δ_0 is a function of the density ratio $\Omega = \rho_2/\rho_1$ and velocity ratio $\phi = u_2/u_1$ across the mixing layer given by Ref. [25]

$$\delta_0' = C_\delta \frac{(1 - \phi)(1 + \Omega^{1/2})}{2(1 + \Omega^{1/2}\phi)} \left\{ 1 - \frac{(1 - \Omega^{1/2})/(1 + \Omega^{1/2})}{1 + 2.9(1 + \phi)/(1 - \phi)} \right\} \tag{22}$$

where C_δ is a constant with a value of around 0.35.

The latent heat released into the wet steam mixture during condensation causes higher static temperatures in the primary nozzle flow than in the equivalent ideal gas case, as illustrated in Fig. 8. The Mach number is lower in the wet steam case than in the equivalent ideal gas case, Fig. 9 and this is because the relative increase in the speed of sound is higher than the relative increase in velocity, Fig. 11.

Mixing of the primary nozzle flow with the secondary stream begins at the nozzle exit, and compressibility effects within the mixing layer will be reduced due to condensation because of the higher value of the speed of sound which appears on the denominator of the correlating compressibility parameter (either M_c as indicated in Eq. (19), or Π_c as indicated in Eq. (20)).

To illustrate the effects of the different nozzle exit conditions on the development of mixing downstream, the flow produced by a nozzle with an exit area ratio of 25 for ideal gas and wet steam models is considered based on the results presented in Figs. 10 and 11. Velocity and speed of sound values can be taken directly from Fig. 11 and density values can then be calculated from Fig. 10.

Representative values for secondary stream density of 0.00774 kg/m³ and secondary stream speed of sound of 414 m/s have been adopted based on saturated conditions at a pressure of 1000 Pa (similar to conditions observed in actual ejector experiments). The secondary stream velocity will be changing in the vicinity of the primary nozzle exit, but for the purpose of illustration, a value of 300 m/s has been assumed for further calculations.

Based on these assumptions, the density ratio and velocity ratio are calculated as given in Table 4. Substituting these values in Eq. (22), the growth rate of incompressible mixing layer δ_0' is calculated with the values of 0.169 and 0.180 for ideal gas and wet steam models respectively. Using Eq. (21) with calculated values of Π_c , the growth rate of compressible mixing layer δ' is calculated with the values of 0.0468 and 0.0602 for ideal gas and wet steam models, respectively. The difference in the mixing layer growth rates between the ideal gas and wet steam models is 29%, indicating a significantly faster mixing layer growth rate for the wet steam model. It is therefore postulated that increased entrainment ejector

Table 4
Illustrative parameters for mixing layer development.

	u_1 (m/s)	ρ_1 (kg/m)	Ω	φ	δ'_0	Π_c	δ'
Ideal gas model	1080	0.0194	0.399	0.277	0.169	1.74	0.0468
Wet steam model	1170	0.0166	0.466	0.257	0.180	1.41	0.0602

performance observed in recent ejector simulations using the wet steam model [12,13] arises through augmentation of mixing effects.

Wet steam simulations have also shown higher critical back pressures can be achieved relative to ideal gas simulations of the same ejectors [12,13]. This can be explained by the wet steam simulations producing essentially the same nozzle exit momentum flux but at a higher static pressure and lower Mach number relative to the equivalent ideal gas case. If the secondary stream static pressure and momentum flux at the ejector inlet is the same in both wet steam and ideal gas cases, then at the location where the primary and secondary flows have fully mixed, the static pressure of the mixture will be higher in the case of the wet steam model. Also, the average Mach number of the fully mixed flow in the wet steam simulations will be lower than the equivalent ideal gas case because of the addition of latent heat through the condensation process. Therefore, there will be a greater recovery of total pressure through the shock compression process within the constant area section or the diffuser section in the case of the wet steam model.

7. Conclusions

Recent wet steam simulations of ejectors have yielded higher entrainment ratios and higher critical back pressures than in the case of ideal gas simulations. Existing gas dynamic models of ejector performance fail to explain the origin the higher entrainment ratio in the case of the wet steam simulations. Condensation within steam ejectors is initiated within the primary nozzle and has a profound effect on the flow conditions downstream. Therefore, the present work has focused on the simulation of condensation effects in representative ejector nozzles.

The wet steam simulation method used in this work is first validated using nozzle static pressure data from three experiments available in the literature. The simulations consistently underestimate the static pressure within the nozzles by approximately 10%. The changes in nozzle exit static pressure due to condensation effects are around 70%, so the present simulation method is regarded as being sufficiently accurate for at least a qualitative assessment of condensation effects.

Wet steam flow within three different nozzles with overall area ratios (AR) of 11, 18 and 25 has been simulated for inlet flow stagnation conditions of 275 kPa and 403 K. Results from each nozzle are observed to collapse onto essentially the same curve when plotted as a function of the nozzle area ratio. After the initiation of condensation, higher nozzle static pressures and temperatures result for the wet steam model than in the case of the ideal gas model. Lower Mach numbers are observed in the case of the wet steam model, but there is no significant difference for momentum flux profile when using ideal gas and wet steam models.

Existing gas dynamic models for ejector performance dictate that higher nozzle exit static pressures will reduce the entrainment of the secondary stream, but wet steam simulations of ejector performance yield a higher secondary stream mass flow rate and

yet have higher nozzle exit static pressures than in equivalent ideal gas simulations. The increased speed of sound in primary stream due to the release of latent heat in the condensation process reduces compressibility effects in the mixing layer leading to an augmented mixing rate relative to the ideal gas case. Increased mixing of the primary and secondary streams is proposed as an explanation of the improved entrainment ratio of ejectors simulated with the wet steam model.

References

- [1] J.H. Keenan, E.P. Neumann, A simple air ejector, *ASME J. Appl. Mech.* 64 (1942) 75–81.
- [2] I.W. Eames, S. Aphornratana, H. Haider, A theoretical and experimental study of a small-scale steam jet refrigerator, *Int. J. Refrig.* 18 (6) (1995) 378–386.
- [3] J.T. Munday, D.F. Bagster, A new ejector theory applied to steam jet refrigeration, *Ind. Eng. Chem. Process Des. Dev.* 16 (4) (1997) 442–449.
- [4] B.J. Huang, J.M. Chang, C.P. Wang, V.A. Petrenko, A 1-D analysis of ejector performance, *Int. J. Refrig.* 22 (1999) 354–364.
- [5] Y. Zhu, W. Cai, C. Wen, Y. Li, Shock circle model for ejector performance evaluation, *Energy Convers. Manag.* 48 (2007) 2533–2541.
- [6] S.B. Riffat, S.A. Omer, CFD modeling and experimental investigation of an ejector refrigeration system using methanol as the working fluid, *Int. J. Energy Res.* 25 (2000) 115–128.
- [7] D.W. Sun, I.W. Eames, Recent developments in the design theories and applications of ejectors, *J. Inst. Energy* 68 (1995) 65–79.
- [8] T. Sriveerakul, S. Aphornratana, K. Chunnanond, Performance prediction of steam ejector using computational fluid dynamics: Part 1. Validation of the CFD results, *Int. J. Therm. Sci.* 46 (2007) 812–822.
- [9] T. Sriveerakul, S. Aphornratana, K. Chunnanond, Performance prediction of steam ejector using computational fluid dynamics: Part 2. Flow structure of a steam ejector influenced by operating pressures and geometries, *Int. J. Therm. Sci.* 46 (2007) 823–833.
- [10] Y. Yang, S. Shen, Numerical simulation on non-equilibrium spontaneous condensation in supersonic steam flow, *Int. Commun. Heat. Mass Transf.* 36 (2009) 902–907.
- [11] X. Wang, J. Dong, T. Wang, J. Tu, Numerical analysis of spontaneously condensing phenomena in nozzle of steam-jet vacuum pump, *Vacuum* 86 (2012) 861–866.
- [12] X. Wang, H. Lei, J. Dong, J. Tu, The spontaneously condensing phenomena in a steam-jet pump and its influence on the numerical simulation accuracy, *Int. J. Heat. Mass Transf.* 55 (2012) 4682–4687.
- [13] N. Sharifi, M. Boroomand, M. Sharifi, Numerical assessment of steam nucleation on thermodynamic performance of steam ejectors, *Appl. Therm. Eng.* 52 (2013) 449–459.
- [14] K. Ishazaki, T. Ikohagi, H.A. Daiguji, High-resolution numerical method for transonic non-equilibrium condensation flows through a steam turbine cascade, *Proc. 6th Int. Symp. Comput. Fluid Dyn.* 1 (1995) 479–484.
- [15] J.B. Young, Two-dimensional, nonequilibrium, wet-steam calculations for nozzles and turbine cascades, *J. Turbomach.* 114 (7) (1992) 569–579.
- [16] A.J. White, J.B. Young, Time marching method for the prediction of two dimensional unsteady flows of condensing steam, *J. Propuls. Power* 9 (4) (1993) 579–587.
- [17] A.G. Gerber, M.J. Kermani, A pressure based Eulerian–Eulerian multi-phase model for non-equilibrium condensation in transonic steam flow, *Int. J. Heat. Mass Transf.* 47 (2004) 2217–2231.
- [18] J.B. Young, An equation of state for steam for turbomachinery and other flow calculations, *J. Eng. Gas. Turbines Power* 110 (1) (1988) 1–7.
- [19] ANSYS-FLUENT 14.5 User's Guide.
- [20] M.J. Moore, P.T. Walters, R.I. Crane, B.J. Davidson, Predicting the fog drop size in wet steam turbines, in: *Wet Steam 4 Conference*, Institute of Mechanical Engineers (UK), University of Warwick, 1973. Paper C37/73.
- [21] F. Bakhtar, M. Tochai, An investigation of two-dimensional flows of nucleating and wet steam by the time marching method, *Int. J. Heat. Fluid Flow.* 2 (1980) 5–18.
- [22] G. Al-Doori, Investigation of Refrigeration System Steam Ejector Performance Through Experiments and Computational Simulations, PhD thesis, University of Southern Queensland, 2013.
- [23] D. Papamoschou, A. Roshko, The compressible turbulent shear layer: an experimental study, *J. Fluid Mech.* 197 (1988) 453–477.
- [24] M.D. Slessor, M. Zhuang, P.E. Dimotakis, Turbulent shear-layer mixing: growth-rate compressibility scaling, *J. Fluid Mech.* 414 (2000) 35–45.
- [25] P.E. Dimotakis, Two-dimensional shear-layer entrainment, *AIAA J.* 24 (1986) 1791–1796.

Chapter 4 Effect of steam condensation on the ejector performance



Effect of mixing on the performance of wet steam ejectors



Kavous Ariaifar^{a,*}, David Buttsworth^a, Ghassan Al-Doori^{a,b}, Ray Malpress^a

^a University of Southern Queensland, Australia

^b Tikrit University, Iraq

ARTICLE INFO

Article history:

Received 3 June 2015

Received in revised form

23 September 2015

Accepted 21 October 2015

Available online 19 November 2015

Keywords:

Steam ejector

Entrainment ratio

Condensation

Shear layer mixing

Pitot pressure

CFD (computational fluid dynamics)

ABSTRACT

Steam ejector computational simulations using a wet steam model give higher entrainment ratios and higher critical back pressures for the ejector compared with the ideal gas model. This paper identifies the origin of these differences. Simulation results show that the wet steam model predicts an entrainment ratio for the choked flow ejector operation that is 10% higher than that for the ideal gas model. The wet steam model also gives a higher critical back pressure by about 7% relative to the ideal gas model with a closer agreement to experimental data for the unchoked ejector operation. Enhanced mixing layer growth which arises due to steam condensation in the primary nozzle is identified as the main reason for higher entrainment ratio of the ejector simulations using the wet steam model. The difference in the mixing layer growth rate between ideal gas and wet steam simulations is 21%, indicating enhanced entrainment for the wet steam model. Furthermore, the mixture at the start of the diffuser is shown to have a higher pitot pressure than in the ideal gas simulations and these elevated pitot pressures allow the ejector to operate in a choked mode to a higher critical back pressure.

© 2015 Elsevier Ltd. All rights reserved.

1. Introduction

Supersonic steam ejectors are widely used in a large number of industries that require steam for heating or a power generating medium. Ejectors are devices which utilize the energy of a high pressure fluid (the primary stream) to move a low pressure fluid (the secondary stream) and enable it to be compressed to a higher pressure. Their action is similar to a vacuum pump or compressor but ejectors do not use any moving components or electricity for the compression process. They are known for simple construction, easy installation and low capital costs. Steam ejectors essentially consist of four main parts: a primary nozzle, a mixing chamber, a constant area section and a diffuser. Fig. 1(a) shows a schematic of a typical steam ejector illustrating the different parts.

A typical performance curve of an ejector can be categorized into three operating regions as illustrated in Fig. 1(b): choked flow, unchoked flow and reversed flow. Choked flow occurs when the discharge pressure is lower than the critical back pressure. For the unchoked mode, the secondary stream is no longer choked and its mass flow rate decreases rapidly with increasing discharge pressure which reduces the ER (entrainment ratio). Further increase in

the discharge pressure causes flow to reverse back to the secondary stream's inlet and ejector malfunction occurs.

There are different parameters affecting the ejector performance including the operating conditions, the geometry of the primary nozzle and its exit position in the mixing chamber, the diameter of the nozzle throat and that of the constant area section. Works from several authors are available in the literature investigating such parameters using CFD (computational fluid dynamics) methods which appear to accurately simulate the flow field inside ejectors [1–6].

Ji et al. [5] and Sreevirakul et al. [7] used CFD methods to investigate the flow structure inside ejectors. They analyzed flow behavior and mixing processes inside steam ejectors and identified the formation of shock waves and how these affect the ejector performance. Yang et al. [8] performed a numerical study on the mixing process in a steam ejector using different nozzle structures. From their investigations, characteristics of the mixing process were explained based on the simulation of streamwise and spanwise vortex distribution in the mixing chamber and their effects on the ejector performance. The ideal gas assumption was employed for these CFD simulations of ejectors, even in the studies which considered water vapor as the working fluid.

The conditions under which water vapor flows begin to condense are already quite well understood and such conditions often occur in steam ejectors. Droplet nucleation and the

* Corresponding author.

E-mail address: Kavous.ariafar@usq.edu.au (K. Ariaifar).

Nomenclature		U	velocity, m/s
		x	streamwise distance, m
<i>English letters</i>		<i>Greek letters</i>	
a	speed of sound, m/s	β	liquid mass fraction
b	nozzle throat diameter, m	Γ	mass generation rate, kg/m ³ s
E	total energy, J	γ	ratio of specific heats
I	nucleation rate, # droplets/m ³ .s	γ_e	equilibrium specific heat ratio
k	turbulent kinetic energy, J/kg	δ	mixing layer thickness, m
M	Mach number	δ'	growth rate of mixing layer thickness
M_c	convective Mach number	δ'_0	growth rate of equivalent incompressible mixing layer
M_e	equilibrium Mach number	η	droplet number density, 1/m ³
P	static pressure, Pa	μ	dynamic viscosity, N s/m ²
P_0	total pressure, Pa	μ_t	turbulent viscosity, N s/m ²
P_{pitot}	pitot pressure, Pa	Π_c	compressibility parameter
r	radial distance, m	ρ	mixture density, kg/m ³
S	streamwise distance measured from the nozzle throat, m	τ_{ij}	stress tensor
T	static temperature, K	ϕ	velocity ratio
T_s	saturation temperature, K	χ	steam quality
t	time, s	Ω	density ratio
		ω	specific dissipation rate, 1/s

subsequent development of condensation result in a number of energy transfers which cannot be accurately simulated by assuming that the steam behaves as a perfect gas. Therefore, recent CFD simulations of steam ejector performance have incorporated droplet nucleation and condensation models. Some valuable numerical assessments of ejectors have been completed to study

nucleation phenomenon and to investigate condensing steam flow behavior [9–12]. These studies concluded that the wet steam simulation yields a higher entrainment ratio and critical back pressure compared with ideal gas or dry steam simulations.

An important process which affects the performance of ejectors is the mixing of the primary and secondary streams. When two

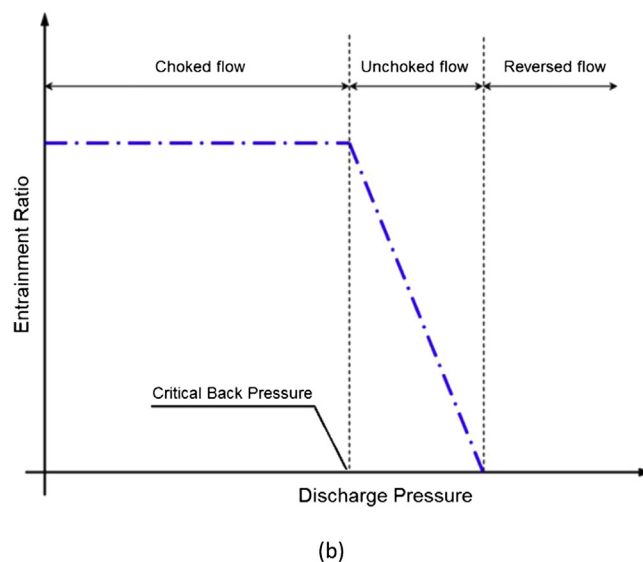
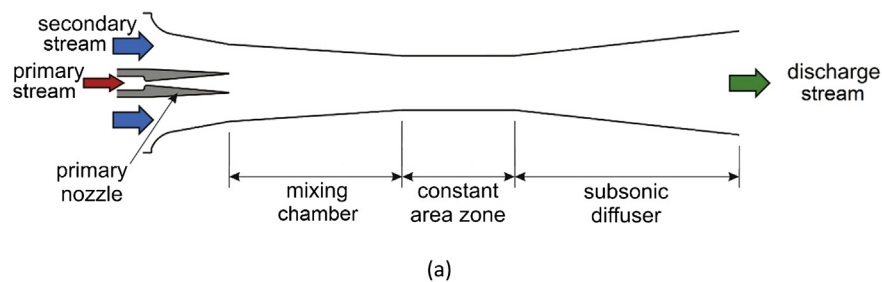


Fig. 1. (a) Schematic showing a typical ejector cross-section illustrating the different zones, (b) Illustrative performance curve of the ejector.

uniform and nearly parallel streams with different velocities start to mix, a mixing layer forms at their interface. Growth of the mixing layer is associated with the entrainment of mass into the mixing layer. Parameters which affect the mixing layer growth rate include the velocity ratio of the two streams, the density ratio, compressibility effects and Reynolds number. Several investigations have been completed on the effect of these parameters on the mixing layer growth rate.

Brown and Roshko [13] performed experiments for incompressible mixing layers with combinations of different gases with large density differences. The effect of compressibility on the growth rate of mixing layers was studied by Bogdanoff [14], and Papamoschou and Roshko [15] subsequently introduced the convective Mach number (M_c) to correlate compressibility effects on mixing layer growth rate. The convective Mach number is a Mach number with respect to a frame of reference traveling with the large scale structures in the flow. Papamoschou and Roshko [16] concluded that the compressible mixing layer growth rate normalized using an equivalent incompressible mixing layer growth rate decreases with increases of the convective Mach number. Elliot and Samimy [16] showed that not only does the normalized growth rate decrease with an increase in the convective Mach number, but turbulence quantities also decrease.

In the existing wet steam ejector simulation literature [9–12] it is concluded that using a wet steam model gives a higher entrainment ratio and higher critical back pressure relative to ejector simulations using the ideal gas model, but the reasons for the higher performance parameters in the wet steam case have not previously been defined. To explain why simulations using wet steam modeling yield higher ejector performance relative to ideal gas modeling, this paper presents results from the numerical simulation of an experimental steam ejector. The ejector is simulated using both ideal gas and wet steam models to define the role which condensation and mixing plays on the ejector performance.

2. Mixing layer empirical model

Compressibility effects in turbulent mixing layers reduce the mixing rate of the two streams relative to equivalent incompressible cases having the same velocity and density ratio across the mixing layer. The attenuated mixing effect has been correlated using the convective Mach number [15,17] which is defined as:

$$M_c = \frac{\Delta U}{a_1 + a_2} \quad (1)$$

where ΔU is the velocity difference between the two streams on either side of the mixing layer, and a_1 and a_2 are the speeds of sound on either side of the mixing layer. Slessor et al. [18]

subsequently introduced another correlating parameter for compressibility effects:

$$\Pi_c = \max \left[\frac{\sqrt{\gamma_i - 1}}{a_i} \right] \Delta U \quad (2)$$

where i refers to either of the streams. These dimensionless numbers characterize compressibility in terms of the difference between the speeds of two layers relative to a representative speed of sound within the layer.

Compressibility effects on the growth rate of the mixing layer have been correlated using the expression [18]:

$$\frac{\delta'}{\delta'_0} = \left(1 + \alpha_0 \Pi_c^2 \right)^{-\beta_0} \quad (3)$$

where δ'/δ'_0 is the normalized growth rate of the mixing layer. The width of a fully-developed mixing layer δ increases linearly with streamwise distance (Fig. 2), so the growth rate of the compressible mixing layer δ' (which is defined as $d\delta/dx$ where x is streamwise distance) is constant. In the above expression, δ'_0 is the growth rate of an incompressible mixing layer with the same density ratio and velocity ratio as the compressible case, and α_0 and β_0 are correlating parameters with approximate values of $\alpha_0 = 4$ and $\beta_0 = 0.5$.

The growth rate of the equivalent incompressible mixing layer δ'_0 is a function of density ratio $\Omega = \rho_2/\rho_1$ and velocity ratio $\phi = U_2/U_1$ across the mixing layer. A correlation for δ'_0 was obtained by Dimotakis [19]:

$$\delta'_0 = C_\delta \frac{(1 - \phi)(1 + \Omega^{1/2})}{2(1 + \Omega^{1/2}\phi)} \left\{ 1 - \frac{(1 - \Omega^{1/2})/(1 + \Omega^{1/2})}{1 + 2.9(1 + \phi)/(1 - \phi)} \right\} \quad (4)$$

where C_δ is a constant with a value of around 0.35.

There are different possible definitions of the mixing layer thickness. The most commonly used are δ_{10} , δ_{pit} and δ_ω [20]. In the δ_{10} definition, which was adopted in the present work, the mixing layer thickness is defined as the distance between two points in the velocity profile where the local velocity is equal to $U_1 - 0.1\Delta U$ and $U_2 + 0.1\Delta U$ (Fig. 2). This mixing layer thickness, which is also described as the velocity 10% thickness, was used by Samimy and Elliott [21] and Goebel and Dutton [22]. The mixing layer thickness based on δ_{pit} is defined as the width of the pitot pressure profile from 5% to 95% of the difference of the free stream values. Papamoschou and Roshko [15], Clemens and Mungal [23] and Slessor [24] used this definition in their work. The last definition δ_ω or the vorticity thickness, is defined to be the distance given by the ratio of the velocity difference ΔU across the layer divided by the maximum slope of the velocity profile $[\partial U/\partial y]_{max}$. For an error function

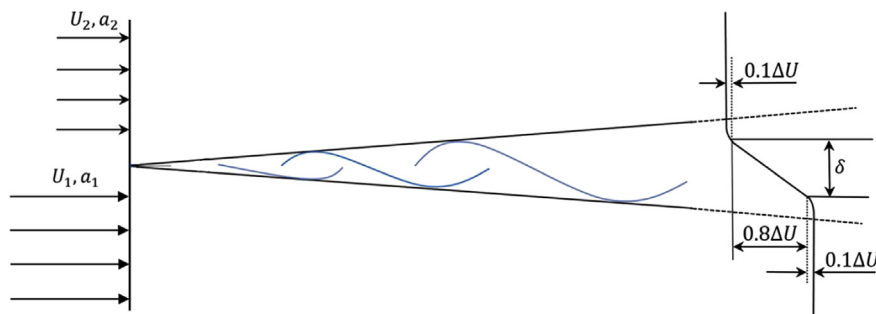


Fig. 2. Schematic of the mixing layer development downstream of the primary nozzle and the δ_{10} definition.

velocity profile, it has been shown that $\delta_w = 1.02\delta_{10}$ [20,22]. A less commonly used definition for the mixing layer thickness is the Stanford thickness δ_s which is defined by the distance between two points where the local velocity is $U_2 + \sqrt{0.1}\Delta U$ and $U_2 + \sqrt{0.9}\Delta U$ [25]. Chinzei et al. [26] and Barre et al. [27] applied this definition in their works.

3. Computational model

3.1. Governing equations

The laws of conservation of mass, momentum and energy which have been solved in this present work through computational simulation are:

$$\frac{\partial \rho}{\partial t} + \frac{\partial}{\partial x_i} (\rho U_i) = 0 \quad (5)$$

$$\frac{\partial}{\partial t} (\rho U_i) + \frac{\partial}{\partial x_j} (\rho U_i U_j) = -\frac{\partial P}{\partial x_i} + \frac{\partial \tau_{ij}}{\partial x_j} \quad (6)$$

$$\frac{\partial}{\partial t} (\rho E) + \frac{\partial}{\partial x_i} (U_i (\rho E + P)) = \bar{\nabla} \cdot \left(\alpha_{eff} \frac{\partial T}{\partial x_i} + U_j (\tau_{ij}) \right) \quad (7)$$

with

$$\tau_{ij} = \mu_{eff} \left(\frac{\partial U_i}{\partial x_j} + \frac{\partial U_j}{\partial x_i} \right) - \frac{2}{3} \mu_{eff} \frac{\partial U_k}{\partial x_k} \delta_{ij} \quad (8)$$

3.2. Turbulence model

In order to simulate mixing layer development and the particular ejector configuration considered in this work, a two equation turbulence model was applied to the whole flow domain based on the $k - \omega$ SST (Shear Stress Transport). A benefit of this model is the capacity to simulate free shear flow spreading rates which agrees with measurements for far wakes, mixing layers, round and radial jets and therefore it is applicable to both wall-bounded flows and free flows [28]. The main governing equations for this model are described by Ref. [28]:

$$\frac{\partial(\rho k)}{\partial t} + \frac{\partial}{\partial x_i} (\rho k U_i) = \frac{\partial}{\partial x_j} \left[\left(\mu + \frac{\mu_t}{\sigma_k} \right) \frac{\partial k}{\partial x_j} \right] + G_k - Y_k + S_k \quad (9)$$

$$\frac{\partial(\rho \omega)}{\partial t} + \frac{\partial}{\partial x_i} (\rho \omega U_i) = \frac{\partial}{\partial x_j} \left[\left(\mu + \frac{\mu_t}{\sigma_\omega} \right) \frac{\partial \omega}{\partial x_j} \right] + G_\omega - Y_\omega + D_\omega + S_\omega \quad (10)$$

where k and ω are the turbulent kinetic energy and the specific dissipation rate, respectively. Definitions of the terms G , Y , S and D can be found in Ref. [28].

3.3. Wet steam model

The steam behavior is treated using the Eulerian–Eulerian approach and the two phase flow is modeled using the compressible Navier–Stokes conservation equations together with two additional transport governing equations available in the wet steam model in FLUENT for the liquid phase mass fraction (β) and the number of liquid droplets per unit volume (η). To reduce the complexity of the two phase flow model, assumptions of no slip

between the phases and negligible volume of the condensed liquid are used since droplet sizes are typically very small and negligible interaction between the droplets is expected. The first additional transport equation governing the mass fraction of the condensed liquid phase is written as [29]:

$$\frac{\partial(\beta \rho)}{\partial t} + \nabla \cdot (\rho \beta \vec{U}) = \Gamma \quad (11)$$

where Γ is the mass generation rate due to condensation and evaporation, which is correlated with the nucleation rate I (number of new droplets per unit volume per second) and the growth or demise of these droplets.

The second additional transport equation estimates the growth of droplet numbers per unit volume of steam and is described as:

$$\frac{\partial(\rho \eta)}{\partial t} + \nabla \cdot (\rho \eta \vec{U}) = \rho I \quad (12)$$

In this model, the homogeneous nucleation theory explains the creation of a liquid phase in the form of droplets from a superheated phase in the absence of foreign particles. The estimation of the size of created droplets during the nucleation in wet steam flow is very difficult. The classical theory of nucleation is used to calculate the number of liquid droplets. More information about the wet steam theory and the equations used in the present approach can be obtained from Ref. [30].

3.4. Numerical solution procedure

The governing equations were solved numerically using a commercial CFD code, FLUENT 14.5 which is based on the control volume method to approximate the governing equations as algebraic equations. The convection terms were discretized with the second order upwind scheme to achieve a high order of accuracy at cell faces through a Taylor series expansion of the cell centered solution. The nonlinear governing equations were solved using the coupled implicit solver using the density-based method and the standard wall function was applied near the walls. Convergence of the solution was assumed when two criteria were satisfied:

- the relative difference of mass flow rate between the inlet and outlet boundaries of less than 10^{-7} ; and
- every type of calculated residual error was less than 10^{-6} .

4. Validation of the numerical method

The two key aspects of the computational simulations upon which subsequent arguments in this paper rely are: (1) the wet steam model; and (2) the model for turbulent mixing. Therefore, particular attention has been given to the validation of these aspects. This validation work has been described in detail elsewhere [30,31], but a summary of the key conclusions is included herein for completeness.

4.1. Wet steam model

For the wet steam validation work, pressure measurements from two experiments reported by Moore et al. [32] (nozzle A and B cases) and one experiment reported by Bakhtar et al. [33] were considered for simulation. In these experiments, static pressure was measured at various points along the nozzle axis. Detailed information about the geometry and boundary condition for each nozzle is presented in Ref. [30]. Fig. 3 shows a representative case of the validation work for the nozzle A case. As it can be observed, the simulated static pressure along the nozzle centerline are in a good

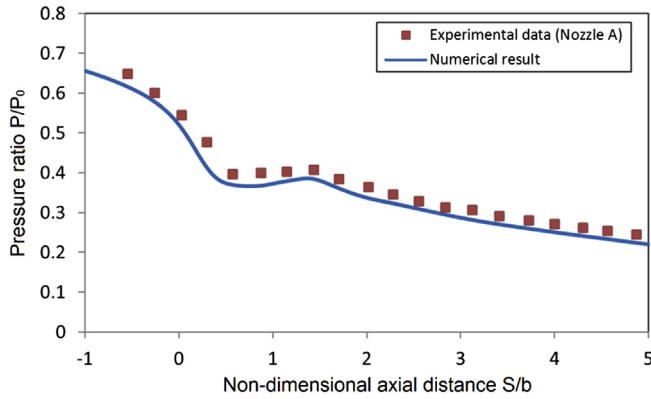


Fig. 3. Comparisons between simulation results and experimental data: Moore et al. [32], nozzle A case.

agreement with the experimental data and the location of condensation front (shock) downstream of the nozzle throat is predicted well.

This particular simulation was performed with a stagnation pressure and temperature of 25 kPa and 354.6 K, respectively. The saturation temperature at this pressure is 338.14 K. A 2-D solver was selected for simulation as the experimental model was rectangular in cross section. The average relative error between the simulation results and experimental data for this case was -7% while it was about -8% across the three simulated cases [30]. Negative relative error indicates that the simulation results underestimate the measured static pressures.

4.2. Turbulent mixing model

Validation of the simulation methods for conditions of compressible turbulent mixing is achieved by investigating the variation of normalized growth rate of the mixing layer (δ'/δ'_0) with the convective Mach number (M_c). Two parallel streams of air (similar to the arrangement shown in Fig. 2) were arranged to enter a 2-D planar domain in the simulations. The values of velocity and temperature for each stream were selected so different values of M_c ranging from 0.6 to 1.8 were obtained. This range of M_c values was

selected based on ejector simulations; immediately downstream of the primary nozzle exit M_c values are higher than 0.6, as discussed in Section 7. More information about the values of velocity and temperature for each simulation case, plus the geometry and specified boundary conditions can be found in Ref. [31].

Velocity profiles at seven streamwise distances were extracted from the simulation results for each case to determine the mixing layer thickness δ based on the definition of 80% of the velocity difference as illustrated in Fig. 2. The growth rate of the mixing layer thickness δ' was determined from the slope of the fitted line for the mixing layer thickness as a function of the streamwise distance. The growth rate of the equivalent incompressible mixing layer δ'_0 was calculated using the flow properties for each case using the correlation given in Eq. (4). Normalized growth rate of the mixing layer was then calculated using the values of δ' and δ'_0 for each M_c case. For additional details on the methods for determining δ' and δ'_0 , readers are referred to Ref. [31].

Fig. 4 shows the comparison between simulation results and available experimental data reported in the literature for the variation of the normalized growth rate of the mixing layer with the convective Mach number. As observed in Fig. 4, the computational simulation results are in reasonable agreement with experimental data. The application of different definitions for the calculation of the mixing layer thickness contributes to the significant scatter observed in the experimental results. The standard deviation between the experimental data and the CFD simulation over this range of convective Mach numbers is about 11% [31] and thus the CFD is confirmed as an adequate approach in simulating the mixing layer development in the present steam ejector applications.

5. Ejector geometry and boundary conditions

The main dimensions of the particular steam ejector considered for the present simulation are summarized in Table 1. The computations were done using an axisymmetric solver in order to reduce the CPU cost and simulation time.

Fig. 5 shows the computational element configuration with a magnified view of the mesh elements near the nozzle throat, at the end of the primary nozzle and at the start of the mixing chamber and within the constant area zone. Structured quadrilateral elements were used. To check the sensitivity of the results to the mesh density, three different mesh densities were generated: the coarse

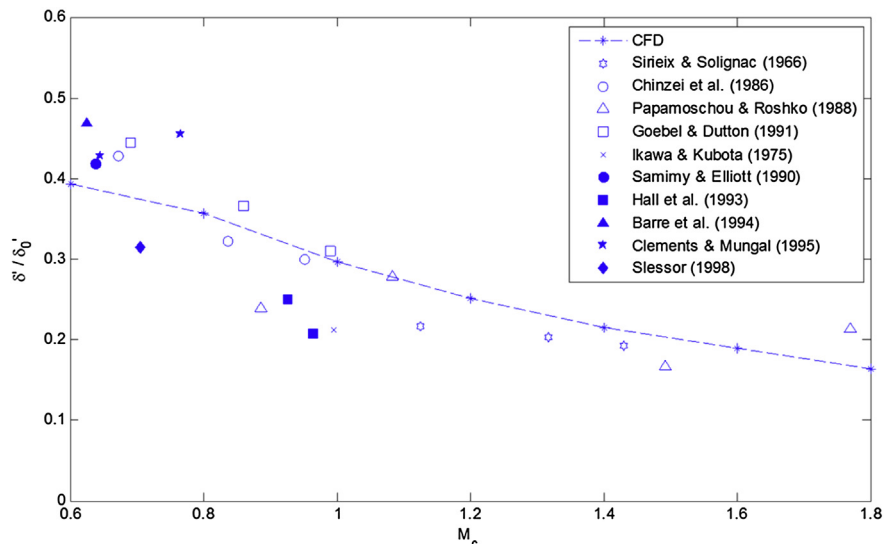


Fig. 4. Comparison between simulation results and experimental data for the growth rate of compressible mixing layers as presented in Ref. [31].

Table 1
Geometric details of the steam ejector [34].

Geometric parameters	Size (mm)
Primary nozzle inlet diameter	10
Primary nozzle throat diameter	3.2
Primary nozzle outlet diameter	13.6
Primary nozzle divergent length	59.5
Mixing chamber inlet diameter	37
Mixing chamber length	155
Constant area zone diameter	25.4
Constant area zone length	75
Subsonic diffuser length	210
Subsonic diffuser outlet diameter	50

mesh density with 14,400 elements, the medium with 42,900 and the fine with 78,500 elements. The mesh adaption was performed in FLUENT and for the regions of downstream of the primary nozzle exit in the mixing chamber where the mixing of two steams starts and near the ejector wall. The results (obtained with the ejector operating conditions presented in Table 2) showed that the difference in the net mass flow rate between the medium and fine levels was 0.55%, hence the medium mesh was selected with consideration of the computational costs while providing sufficient cells in the mixing chamber. A resolution of 4 cells per mm in the transverse direction is required where mixing of the primary and secondary streams occurs, in order to reliably calculate the growth rate of mixing layer using the approach outlined in Section 4.2.

In CFD simulations with turbulent wall-bounded flows, the size of nearest cell to the wall (y^+) is very important. The required value for this dimensionless parameter depends on the selected turbulence model. For the case of the $k-\omega$ turbulence model, the first cell to the wall needs to be at no more than $y^+ = 1$ in order for there to be at least one cell in the viscous sublayer. In the mesh generation for the particular ejector model, the value of y^+ for the coarse mesh was around 2.2 but it was about 0.7 and 0.3 for the medium and fine mesh densities, respectively.

For the ejector boundary conditions, pressure inlet boundaries were selected for the primary and secondary streams entering the ejector and a pressure outlet was used for the discharge stream leaving the ejector. Inlet boundary conditions were set based on the saturation conditions to match experimental operating conditions reported by Al-Doori [34]. The values for pressure and temperature at different boundaries of the domain are presented in Table 2. Note that although a single value of discharge pressure is specified in Table 2, a range of discharge pressures between 4.2 and 7.6 kPa were used when simulating ejector performance variations with condenser pressure.

6. Results

Flow characteristics in the simulated steam ejector based on the ideal gas and wet steam models is presented in this section.

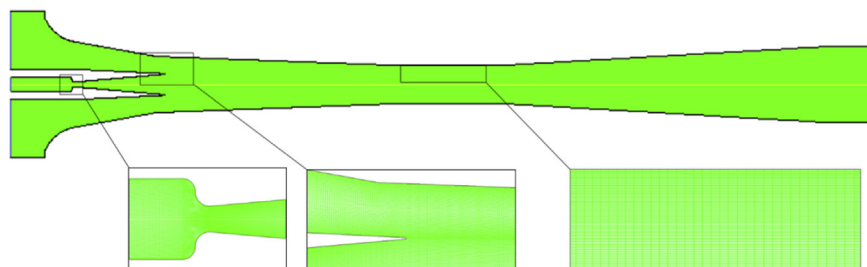


Fig. 5. Computational elements for ejector simulations, medium mesh density.

6.1. Static pressure distribution along the ejector wall

Fig. 6 shows the static pressure distribution along the simulated ejector wall based on the ideal gas and wet steam simulations compared with experimental data reported by Al-Doori [34]. The comparison is based on the boundary conditions presented in Table 2 for the primary and secondary streams and a discharge pressure of 6.1 kPa. For this data, the primary nozzle exit was positioned 6 mm inside the start of the mixing region contraction, corresponding to the location shown in Fig. 5 (NXP (nozzle exit position) = +6 mm in the work of Al-Doori [34]). Fig. 6 shows that for the ideal gas model, the static pressure profiles from CFD simulations are in reasonable agreement with available experimental data and are similar to those presented in the literature [35,36]. One possible reason for the difference between experimental data and simulation results may be due to error in static pressure measurements in the experiment due to the difficulty of calibrating the pressure transducers at very low absolute pressure level.

The simulated pressure profile using the wet steam model displays significant structure that is not observed in the ideal gas simulation; two distinct zones of pressure rise are observed. The first distinct pressure rise in the wet steam case occurs in the mixing chamber and is attributable to the higher static pressure of the wet steam primary stream leaving the nozzle. The second distinct pressure rise for the wet steam simulation occurs near the outlet of the constant area zone and brings the static pressure close to the diffuser exit static pressure. For the simulations of Fig. 6, the ejector in the simulated wet steam case is operating a discharge pressure somewhat lower than the critical back pressure (for the wet steam simulations) whereas in the simulated ideal gas case, the ejector's discharge pressure is slightly higher than the ideal-gas-simulated critical back pressure.

The results from the simulations presented in Fig. 6 are representative of the level of agreement achieved in the other operating conditions where corresponding experimental data were available for comparison. There is an average relative error of 8.6% between the results of ideal gas simulation and experimental data while the difference is 11.2% for the wet steam case. Although the average relative error is slightly worse in the wet steam simulations, the difference is not particularly significant. It is concluded that the wet steam model is about as capable as the ideal gas model in simulating the static pressure profile.

6.2. Performance curve of the ejector

Fig. 7 shows performance curves of the ejector simulated with the ideal gas and wet steam models based on different back pressures of the ejector. In this figure, CFD results are compared with available experimental data for the ejector reported by Al-Doori [34], again with the primary nozzle exit located 6 mm inside the start of the mixing region contraction.

Table 2

Steam pressure and temperature values applied at ejector boundaries in the computational simulation.

Stream	Temperature (K)	Pressure (kPa)
Primary	403	270
Secondary	287	1.6
Discharge	–	4.2

Over this range of operating conditions, the wet steam model over-estimates the value of the entrainment ratio relative to the experimental data in the choked flow region, but under-estimates the critical back pressure relative to the experimental data. The value of entrainment ratio in the choked flow region in the experiment was 0.33 while it was 0.343 and 0.378 based on ideal gas and wet steam simulations, respectively; the difference between the ideal gas and wet steam cases is about 10%. The critical back pressure of the ejector in the ideal gas case was around 6 kPa, while it was around 6.4 kPa for the wet steam simulations – a difference of about 7%. The experimental data gives a critical back pressure of around 6.8 kPa. The simulation results for this particular ejector are comparable with those reported in other works [9–12] in which a higher entrainment ratio and a higher critical back pressure are identified using the wet steam model relative to the ideal gas simulation. Prior works [9–11] showed that the wet steam model yields an entrainment ratio around 14% higher than that for the ideal gas model under the same operating conditions (compared with 10% in the present case). Refs. [9–11] also reported that under the same boundary conditions, the wet steam model predicts a critical back pressure around 6% higher than that resulting from the ideal gas simulation (compared with 7% in the present case).

7. Discussion

The simulation results from the recent ejector simulations reported elsewhere [9–11] demonstrate that wet steam ejector simulations give a higher entrainment ratio and higher critical back pressure than equivalent simulations using an ideal gas model. However, the origin of such differences has not previously been

explained. The following discussion offers an explanation for the higher performance obtained in the simulation of ejectors using the wet steam model.

7.1. Higher entrainment ratio

As discussed in Section 4, the contacting of two streams with different values of velocity leads to the development of a mixing layer with increasing thickness in the streamwise direction. In the case of an ejector, the mixing of the primary and secondary streams starts at the end of the primary nozzle, where the streams first come in contact. The spreading rate of the mixing layer in the wet steam simulation is different from the case in the ideal gas simulation. The wet steam simulation models the condensation phenomenon in the primary nozzle and simulated values of velocity and temperature at the end of primary nozzle differ substantially from the ideal gas simulation case. This difference affects the mixing rate which can lead to a change in the ejector entrainment ratio.

Fig. 8(a) and (b) shows the development of the velocity vectors in the mixing chamber of the ejector for the ideal gas (part a) and wet steam (part b) simulations. These simulations were performed with a discharge pressure of 4.2 kPa. The mixing layer development is illustrated by the broken lines that have been added to this figure and it is clear that the growth rate of mixing layer is faster in the case of the wet steam simulation. A more rapidly growing mixing layer implies additional entrainment of mass into the mixing layer in the case of the wet steam simulations. Additional mass entrainment in the mixing layer leads to entraining more secondary stream into the mixing chamber and an increase in the entrainment ratio of the ejector.

From a comparison of Fig. 8(a) and (b), it is clear that the mixing region is displaced outwards by a considerable radius in the wet steam case relative to the ideal gas case. This is at least partly due to the higher static pressure in the wet steam case because of steam condensation in the primary nozzle which increases the nozzle exit static pressure. For the simulations with the boundary conditions presented in Table 2, the value of static pressure at the end of the primary nozzle is 1500 Pa for the ideal gas simulation (Fig. 8(a)) while it is 2500 Pa for wet steam simulation (Fig. 8(b)).

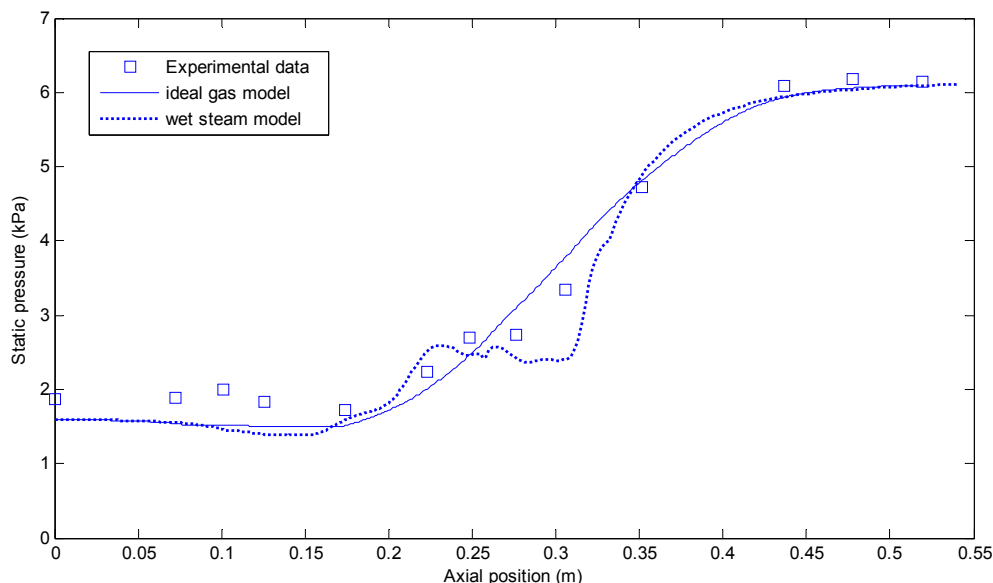


Fig. 6. Static pressure distribution along the ejector wall for the case of primary, secondary and discharge pressures of 270 kPa, 1.6 kPa, and 6.1 kPa respectively.

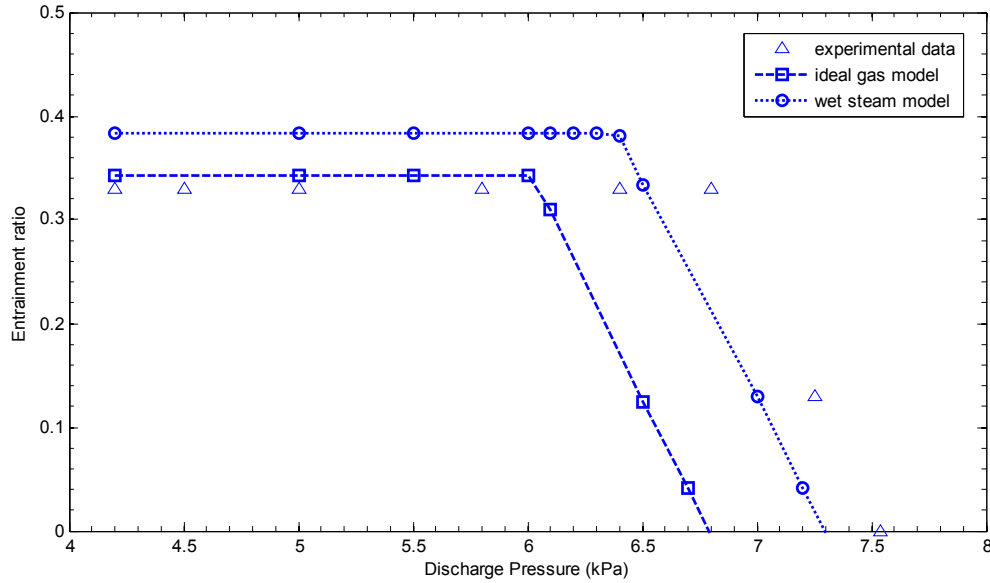


Fig. 7. Entrainment ratio with CFD simulations compared with experimental data.

To investigate if the elevated nozzle exit static pressure in the case of the wet steam simulations could be responsible for the increased growth of the mixing layer, another ideal gas simulation was performed with a higher nozzle exit static pressure to match the static pressure in the wet steam case. Results from this simulation are presented in Fig. 8(c). The spreading rate of the mixing layer in this elevated-pressure ideal gas simulation remains significantly lower than that of the wet steam case.

To quantify growth rate of the mixing layers in these three cases the velocity profile analysis referred to in Section 4.2 has been applied to these steam ejector simulations. Using the simulated velocity profiles at different streamwise locations in the mixing chamber, the mixing layer thickness δ was calculated at each location based on the thickness definition illustrated in Fig. 2.

Fig. 9 shows the mixing layer thickness results from this analysis. Linear regressions to the mixing layer thickness results are also included in Fig. 9. Based on the slopes of linear regression, the mixing layer growth rate δ' for the wet steam case is 0.075 (Fig. 8 part a) which is significantly larger than the ideal gas case (Fig. 8 part b) for which the growth rate was 0.059. Interestingly, the ideal gas case in which the nozzle exit static pressure was increased to match that of the wet steam case (Fig. 8 part c) gave a growth rate of only 0.0385, substantially lower than the other two cases. The elevated static pressure of the primary stream in the wet steam simulation is not directly responsible for the increased mixing layer growth rate in this case.

The compressibility effects within the mixing layer in the wet steam simulation will be reduced relative to the ideal gas case due to condensation phenomenon in the primary nozzle. Condensation does not greatly change the flow speed but it does increase the speed of sound which appears on the denominator of the correlating compressibility parameter M_c in Eq. (1) or Π_c in Eq. (2) and thus compressibility effects are reduced. The altered condition (velocity, density, and speed of sound) of the primary stream is the reason for the faster spreading rate of the mixing layer for wet steam simulation. Calculated values of M_c at the end of the primary nozzle based on the ideal gas (case (a)) and wet steam (case (b)) simulations are 1.35 and 1.24, respectively. The values of velocity, speed of sound and density for the primary and secondary streams at the primary nozzle exit are presented in Table 3 for each model.

Using these simulated values and the available empirical model (see Section 2), the calculated mixing layer growth rates are 0.0582 and 0.0746 for ideal gas and wet steam simulations, respectively. There is reasonable agreement between the computational and empirical values for the mixing layer growth rate.

The difference in the simulated mixing layer growth rates between the wet steam and ideal gas models is 21%, indicating a significantly faster growth rate for the wet steam model. The difference in the simulated entrainment ratio between the wet steam and ideal gas models is somewhat smaller at approximately 9%. Enhanced mixing layer growth does not translate proportionally into enhanced ejector entrainment ratio. For choked secondary flow operation, ejector entrainment ratio is influenced by both inviscid, pressure-driven effects, and viscous, mixing layer entrainment. A correlation introduced in Ref. [31] based on ideal gas simulations for a range of secondary stream conditions gives the portion of ejector entrainment ratio that can be attributed to mixing layer growth as:

$$\Delta ER = 0.42 (\delta' * ER)^{0.39} \quad (13)$$

where ΔER is the difference between entrainment ratios based on inviscid and viscous simulations and ER is the ejector entrainment ratio in the viscous simulation case. In the present case, where the ideal gas simulation case gives $ER = 0.343$ and $\delta' = 0.059$, the portion of ejector entrainment ratio attributable to mixing layer growth according to this correlation is approximately $\otimes ER = 0.1$, or about 30% of the overall entrainment ratio. The remaining 70% of the overall ejector entrainment ratio is accounted for by inviscid, pressure driven effects. The enhancement of mixing layer growth rate does not translate directly to enhanced ejector entrainment ratio because the mixing chamber effective cross sectional area available to the secondary stream is reduced by the elevated nozzle exit static pressure in the case of the wet steam simulations.

7.2. Higher critical back pressure

The wet steam nozzle flow simulation generates a higher nozzle exit static pressure and lower Mach number relative to the

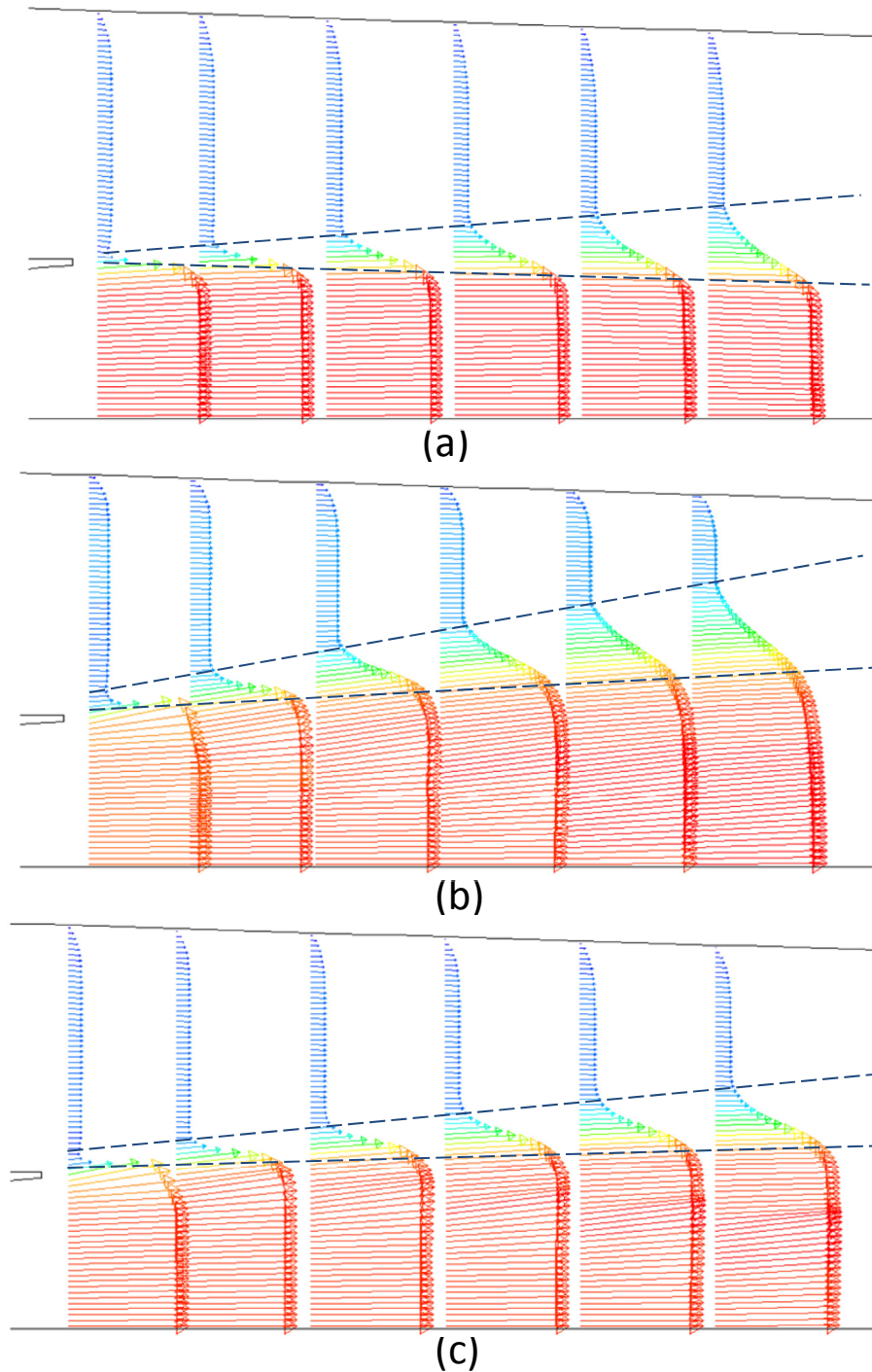


Fig. 8. Velocity vectors in the mixing chamber for different cases: (a) ideal gas simulation, (b) wet steam simulation, (c) ideal gas simulation with nozzle exit static pressure increased to 2.5 kPa.

equivalent ideal gas case but approximately the same nozzle exit momentum flux [30]. The secondary stream's boundary conditions including static pressure and momentum flux remain about the same at the ejector inlet in both ideal gas and wet steam cases. At a hypothetical location where the primary and secondary streams become fully mixed, the static pressure of the mixture will therefore be higher in the case of wet steam simulation. Moreover, because of condensation in the primary nozzle and the associated release of latent heat, the average Mach number of the mixed streams will be lower for the wet steam simulation than the

equivalent ideal gas case. Therefore, there will be a larger recovery of total pressure through the shock compression process within the diffuser section of the ejector in the case of the wet steam model.

The simulations show that higher critical back pressures are achieved with wet steam simulations relative to ideal gas simulations. The capacity for an ejector to increase the flow static pressure through the diffuser can be assessed by calculating the pitot pressure at the inlet to the diffuser. In the case of a subsonic flow, the pitot pressure is equal to the flow total pressure [37]:

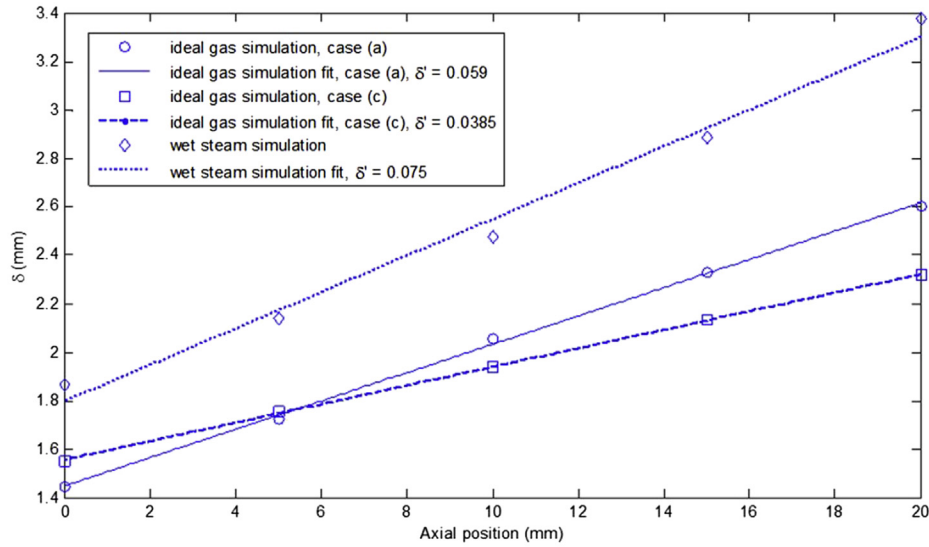


Fig. 9. Mixing layer development in the mixing chamber of the ejector for ideal gas and wet steam simulations.

$$\frac{P_{pitot}}{P} = \frac{P_0}{P} = \left[1 + \frac{\gamma - 1}{2} M^2 \right]^{\gamma/\gamma-1} \quad (14)$$

However, in the case of a supersonic flow, some total pressure is lost through the shock-compression process so the pitot pressure is given by Ref. [38]:

$$\frac{P_{pitot}}{P} = \left[\frac{\gamma + 1}{2} M^2 \right]^{\gamma/\gamma-1} \left[\frac{\gamma + 1}{2\gamma M^2 - \gamma + 1} \right]^{1/\gamma-1} \quad (15)$$

The specific heat ratio γ is constant for the ideal gas (dry steam) case with a value of 1.3. However, there is a departure from ideal gas behavior for wet steam because of steam condensation in the mixture and in this case, equilibrium values of γ and Mach number are used for the calculation of the pitot pressure. The equilibrium value of γ which is denoted as γ_e is 1.12 for low pressure steam and the equilibrium Mach number (M_e) is calculated using the equation presented in Ref. [39].

$$M_e = \frac{U}{\sqrt{\gamma_e(1 - \beta)RT_s}} \quad (16)$$

In this equation, β is the liquid mass fraction in the mixture and T_s is the saturation temperature. Such a similar value for γ_e can be also found by Zeuner's relation for wet steam [40]:

$$\gamma_e = 1.035 + 0.1\chi \quad (17)$$

Where χ is the quality of steam and $\chi = 1 - \beta$. Using this equation with substitution of β values from the FLUENT simulation results in an average value around 1.13 for γ_e at the start of the ejector diffuser.

At the entrance to the ejector's diffuser, the distribution of pitot and total pressure has been determined for ideal gas and wet steam

simulations. The values of P , M , U , β and T_s from the FLUENT simulations were used to calculate the pitot pressure using Eqs. (14) and (15) for the subsonic and supersonic parts, respectively. Fig. 10 shows the calculated pitot pressure results along the radial distance at the start of the diffuser for the ideal gas and wet steam simulations. It also presents the total pressure distribution directly obtained from FLUENT for both models. The calculated values of pitot pressure for the subsonic part of the radial profile closely match the values of total pressure from FLUENT.

At the start of the diffuser, the pitot pressure in the wet steam case is lower than that of the ideal gas case near the centerline of the ejector, but the situation is reversed as the outer most radius is approached. To identify a single representative value of pitot pressure, the average pitot pressure at the start of diffuser is calculated using,

$$\bar{P}_{pitot} = \frac{\int_0^R 2\pi r P_{pitot} dr}{\pi R^2} = \frac{2}{R^2} \int_0^R r P_{pitot} dr \quad (18)$$

where $R = 0.0127m$, the wall radius at the start of the subsonic diffuser. Using this equation for both ideal gas and wet steam simulations, the values of average pitot pressure are calculated as presented in Table 4. The average pitot pressure for the wet steam simulation is higher than that for the ideal gas model and therefore higher downstream pressures can be achieved through aerodynamic deceleration of the wet steam flow without inducing structural changes in the flow field upstream.

Although the calculated average total pressure presented in Table 4 is higher for the ideal gas simulation than that for the wet steam case, average total pressure values (which are also calculated using the same form as Eq. (14)) are not representative of the potential for pressure recovery in the diffuser because a significant

Table 3
Simulated values for each stream at the location of the primary nozzle exit.

Simulation model	Stream	Velocity (m/s)	Sound speed (m/s)	Density (kg/m ³)	M_c	Π_c	δ' (empirical)	δ' (computational)
Ideal gas, case (a)	primary	1060	272	0.0277	1.35	1.85	0.0582	0.059
	secondary	141	411	0.0113				
Wet steam	primary	1129	359	0.0247	1.24	1.47	0.0746	0.075
	secondary	169	413	0.0101				

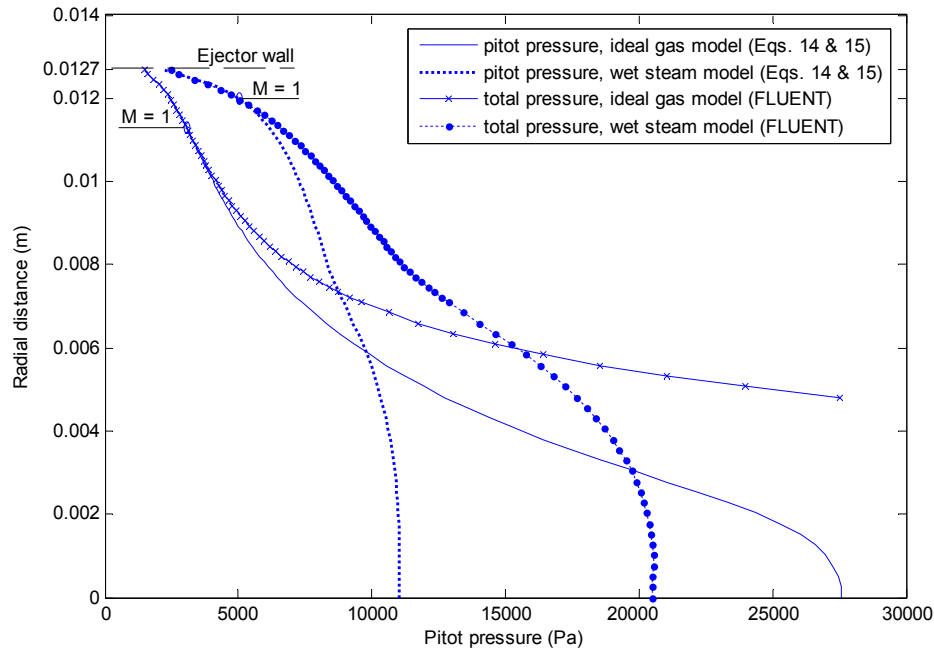


Fig. 10. Pitot pressure distribution in the radial direction at the start of subsonic diffuser.

portion of the flow entering the diffuser is supersonic and the total pressure does not take into consideration the formation of shock waves and the associated loss of total pressure. The deceleration process for supersonic flows typically encountered in ejectors, involves shock waves (a combination of normal and oblique shock waves) and an associated loss in total pressure. Therefore the achievable stagnation pressure of the supersonic flow is better reflected by the pitot pressure rather than the total pressure. As a result, pitot pressure is considered a more appropriate figure of merit in this context.

Another parameter relevant to the ejector critical back pressure is the velocity gradient near the wall at the start of the diffuser. Separation takes place due to the adverse pressure gradient ($dP/dx > 0$) which brings the low speed flow near the diffuser wall to rest more rapidly than it does the flow near the ejector centerline. The flow speed near the diffuser wall is higher for the wet steam model than that for the ideal gas simulation case. Therefore, separation takes place further downstream of the diffuser inlet for the wet steam simulation case.

Fig. 11 illustrates velocity profiles for both ideal gas and wet steam simulations at the location of flow separation in the ejector diffuser with operating conditions as mentioned in Table 2 and 4.2 kPa condenser pressure. As the secondary stream enters the subsonic diffuser, it is subjected to an adverse pressure gradient. The flow in the near-wall region reverses direction because the increase in static pressure exceeds the stagnation pressure of the flow in this near-wall region. As seen in Fig. 11, flow reversal first occurs on the diffuser wall at an axial location of 0.36 m for the ideal gas simulation and at 0.385 m for the wet steam simulation. The reason that flow separation occurs further downstream in the case of the wet steam simulations is a higher value of static pressure and momentum, a higher total pressure for the subsonic flow,

which exists in the vicinity of the wall in wet steam simulation case. Thus, higher pressures can be achieved in the diffuser without flow separation. The value of static pressure on the wall at the start of subsonic diffuser is 2180 and 1430 Pa for wet steam and ideal gas simulations, respectively.

8. Conclusion

Ejector simulations using a wet steam model result in higher entrainment ratios and higher critical back pressures than in the case of an ideal gas model. Flow conditions generated by the primary nozzle are affected by the steam condensation and these altered flow conditions relative to the ideal gas case affect the mixing process of the primary and secondary streams which is initiated at the primary nozzle exit. The present work has determined that augmented mixing of these two streams occurs in the wet steam case and this is the reason for the higher entrainment ratio. The resulting pitot pressure of the mixture is identified as the reason for the higher critical back pressure for the wet steam simulations relative to the ideal gas simulations.

The key simulation methods used in this work have been validated: the wet steam aspects with reference to supersonic steam nozzle flow pressure measurements, and the mixing entrainment aspects with reference to mixing layer growth rate data reported in the literature. Available experimental data for static pressure along the wall of a particular ejector and its performance at different values of condenser pressure were then simulated. Reasonable agreement between the simulation results and experimental data confirm the general reliability of the simulation methods.

The increased speed of sound in the primary stream for the wet steam simulation due to release of latent heat in the condensation process reduces compressibility effects in the mixing layer leading to an augmented mixing rate relative to the ideal gas case. Faster growth of the mixing layer between the primary and secondary streams provides the explanation for the improved entrainment ratio of ejectors simulated with the wet steam model. Higher critical back pressure attained by the wet steam model arises through an increase of the average pitot pressure at the entrance of subsonic diffuser.

Table 4

Calculated values for the average pitot and total pressure.

Simulation model	Average pitot pressure (Pa)	Average total pressure (Pa)
Ideal gas	7114.6	17,530
Wet steam	7806.3	10,840

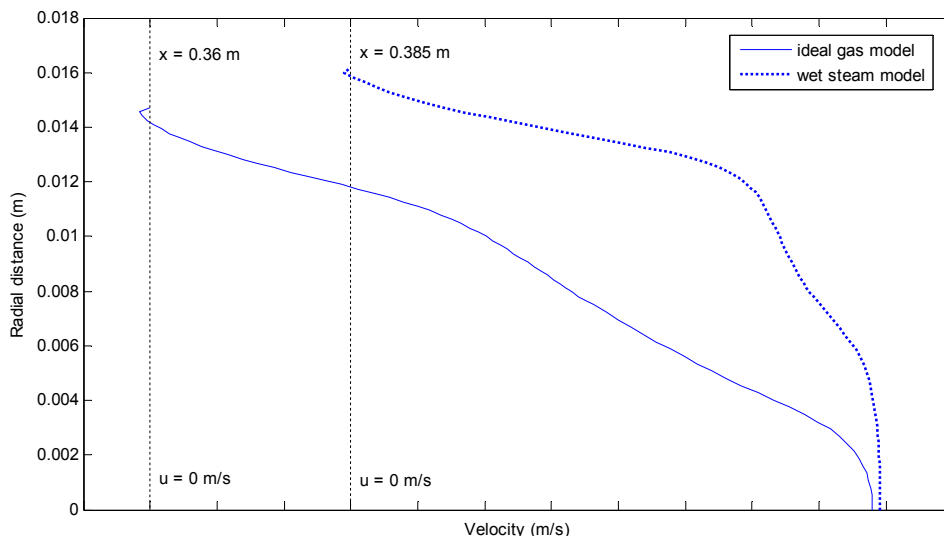


Fig. 11. Simulated velocity profiles at the position of reversal flow in the diffuser. Each velocity increment corresponds to 100 m/s.

Although the generation of water droplets in the primary nozzle represents a thermodynamic irreversibility, an improved mixing process between the primary and the secondary streams can be achieved when steam condensation occurs in the primary nozzle. This causes a higher entrainment ratio and a higher critical back pressure in the steam ejector with condensation. Thus, if higher entrainment ratio and higher back pressure performance are the targets, it is not necessary to superheat the ejector primary stream as the steam condensation in the primary nozzle actually has beneficial effects.

References

- Varga S, Oliveira AC, Diaconu B. Numerical assessment of steam ejector efficiencies using CFD. *Int J Refrig* 2009;32(6):1203–11.
- Varga S, Oliveira AC, Diaconu B. Influence of geometrical factors on steam ejector performance – a numerical assessment. *Int J Refrig* 2009;32(7):1694–701.
- Pianthong K, Seehanam W, Behnia M, Sriveerakul T, Aphornratana S. Investigation and improvement of ejector refrigeration system using computational fluid dynamics technique. *Energy Convers Manag* 2007;48(9):2556–64.
- Sharifi N, Sharifi M. Reducing energy consumption of a steam ejector through experimental optimization of the nozzle geometry. *Energy* 2014;66:860–7.
- Ji M, Utomo T, Woo J, Lee Y, Jeong H, Chung H. CFD investigation on the flow structure inside thermo vapor compressor. *Energy* 2010;35(6):2694–702.
- Ruangtrakoon N, Thongtip T, Aphornratana S, Sriveerakul T. CFD simulation on the effect of primary nozzle geometries for a steam ejector in refrigeration cycle. *Int J Therm Sci* 2013;63:133–45.
- Sriveerakul T, Aphornratana S, Chunnanond K. Performance prediction of steam ejector using computational fluid dynamics: part 2. Flow structure of a steam ejector influenced by operating pressures and geometries. *Int J Therm Sci* 2007;46(8):823–33.
- Yang X, Long X, Yao X. Numerical investigation on the mixing process in a steam ejector with different nozzle structures. *Int J Therm Sci* 2012;56:95–106.
- Sharifi N, Boroomand M, Kouhikamali R. Wet steam flow energy analysis within thermo-compressors. *Energy* 2012;47(1):609–19.
- Sharifi N, Boroomand M, Sharifi M. Numerical assessment of steam nucleation on thermodynamic performance of steam ejectors. *Appl Therm Eng* 2013;52(2):449–59.
- Wang X-D, Lei H-J, Dong J-L, Tu J-y. The spontaneously condensing phenomena in a steam-jet pump and its influence on the numerical simulation accuracy. *Int J Heat Mass Transf* 2012;55(17):4682–7.
- Zheng HT, Cai L, Li YJ, Li ZM. Computational fluid dynamics simulation of the supersonic steam ejector. Part 1: comparative study of different equations of state. *Proc Inst Mech Eng Part C J Mech Eng Sci* 2012;226(3):709–14.
- Brown GL, Roshko A. On density effects and large structure in turbulent mixing layers. *J Fluid Mech* 1974;64(04):775–816.
- Bogdanoff D. Compressibility effects in turbulent shear layers. *AIAA J* 1983;21(6):926–7.
- Papamoschou D, Roshko A. The compressible turbulent shear layer: an experimental study. *J Fluid Mech* 1988;197:453–77.
- Elliott G, Samimy M. Compressibility effects in free shear layers. *Phys Fluids A Fluid Dyn (1989–1993)* 1990;2(7):1231–40.
- Papamoschou D. Structure of the compressible turbulent shear layer. *AIAA J* 1991;29(5):680–1.
- Slessor M, Zhuang M, Dimotakis P. Turbulent shear-layer mixing: growth-rate compressibility scaling. *J Fluid Mech* 2000;414:35–45.
- Dimotakis PE. Two-dimensional shear-layer entrainment. *AIAA J* 1986;24(11):1791–6.
- Smits AJ, Dussauge J-P. Turbulent shear layers in supersonic flow. Springer Science & Business Media; 2006.
- Samimy M, Elliott G. Effects of compressibility on the characteristics of free shear layers. *AIAA J* 1990;28(3):439–45.
- Goebel SG, Dutton JC. Experimental study of compressible turbulent mixing layers. *AIAA J* 1991;29(4):538–46.
- Clemens N, Mungal M. Large-scale structure and entrainment in the supersonic mixing layer. *J Fluid Mech* 1995;284:171–216.
- Slessor MD. Aspects of turbulent-shear-layer dynamics and mixing. 1998. DTIC Document.
- Kline SJ. The 1980–81 afosr-httm-stanford conference on complex turbulent flows: comparison of computation and experiment. In: *AGARD Computation of Viscous-Inviscid Interactions* 22 p (SEE N81-26037 17-01); 1981.
- Chinzei N, Masuya G, Komuro T, Murakami A, Kudou K. Spreading of two-stream supersonic turbulent mixing layers. *Phys Fluids (1958–1988)* 1986;29(5):1345–7.
- Barre S, Quine C, Dussauge J. Compressibility effects on the structure of supersonic mixing layers: experimental results. *J Fluid Mech* 1994;259:47–78.
- ANSYS-FLUENT 14.5 User's guide.
- Ishazaki K, Ikohagi T, Daiguji H. A high-resolution numerical method for transonic non-equilibrium condensation flows through a steam turbine cascade. In: *Proceedings of the 6th International Symposium on Computational Fluid Dynamics*; 1995.
- Ariafar K, Buttsworth D, Sharifi N, Malpress R. Ejector primary nozzle steam condensation: area ratio effects and mixing layer development. *Appl Therm Eng* 2014;71(1):519–27.
- Ariafar, K., et al., Mixing layer effects on the entrainment ratio in steam ejectors through ideal gas computational simulations. *Energy*. Revised version under review.
- Moore MJ, Walters PT, Crane RI, Davidson BJ. Predicting the fog drop size in wet steam turbines. *Wet Steam* 1973;4:101–9.
- Bakhtar F, Tochai MM. An investigation of two-dimensional flows of nucleating and wet steam by the time-marching method. *Int J Heat Fluid Flow* 1980;2(1):5–18.
- Al-Doori GFL. Investigation of refrigeration system steam ejector performance through experiments and computational simulations. University of Southern Queensland; 2013.
- Sriveerakul T, Aphornratana S, Chunnanond K. Performance prediction of steam ejector using computational fluid dynamics: part 1. Validation of the CFD results. *Int J Therm Sci* 2007;46(8):812–22.
- Chunnanond K, Aphornratana S. An experimental investigation of a steam ejector refrigerator: the analysis of the pressure profile along the ejector. *Appl Therm Eng* 2004;24(2):311–22.
- Anderson JD. Modern compressible flow with historical perspective. 2003.
- Massey BS, Ward-Smith AJ, John A. *Mechanics of fluids*. vol. 45. Springer; 1989.
- Guha A. A unified theory for the interpretation of total pressure and temperature in two-phase flows at subsonic and supersonic speeds. In: *Proceedings of the Royal Society of London. Series A: Mathematical, Physical and Engineering Sciences*, vol. 454; 1998. p. 671–95 (1970).
- Nag P. *Power plant engineering*. Tata McGraw-Hill Education; 2002.

Chapter 5 Effects of mixing on the ejector entrainment ratio



Mixing layer effects on the entrainment ratio in steam ejectors through ideal gas computational simulations



Kavous Ariaifar ^{a, *}, David Buttsworth ^a, Ghassan Al-Doori ^{a, b}, Navid Sharifi ^c

^a University of Southern Queensland, Australia

^b Tikrit University, Iraq

^c Amirkabir University of Technology, Iran

ARTICLE INFO

Article history:

Received 10 March 2015

Received in revised form

24 November 2015

Accepted 7 December 2015

Available online xxx

Keywords:

Steam ejector

Mixing layer growth rate

Compressibility effects

Entrainment ratio

CFD (computational fluid dynamics)

ABSTRACT

Ejector entrainment ratios are influenced by both pressure-driven effects and the mixing between the primary and secondary streams, but the significance of each factor has not been identified in prior literature. This paper presents a computational simulation investigation of flow in a representative steam ejector to specify the contribution of mixing and pressure-driven effects to the overall ejector entrainment ratio under different operating conditions. The simulation of mixing layer growth was validated by using experimental data available in the literature, while the application of the computational method to the ejector flows was validated using static pressure distribution and entrainment ratio data in the particular experimental ejector arrangement. Simulation results show that under a fixed operating condition for the primary and discharge streams, at lower secondary pressure the ejector entrainment ratio is more strongly influenced by the mixing effects. For the particular ejector and the operating conditions considered herein, about 35% of the ejector entrainment ratio is due to mixing effects when the secondary stream pressure lift ratio is 4.5, while this portion is reduced to about 22% when the secondary stream pressure lift ratio is 1.6.

© 2015 Elsevier Ltd. All rights reserved.

1. Introduction

Large industrial plants often vent significant quantities of steam to the atmosphere. Recovery of the latent heat content of the otherwise vented steam has the potential to reduce energy demand. One approach is the application of a steam ejector which can boost the pressure and temperature to a more useful level. Steam ejectors are devices which utilize the energy of high pressure steam (the primary stream) to move low pressure steam (the secondary stream) and compress it to a higher pressure. The action of an ejector is akin to a vacuum pump, but ejectors do not use moving components to achieve the compression effect. Ejectors are known for simple construction, easy installation and low capital costs. Steam ejectors essentially consist of four main parts: a primary nozzle, a mixing chamber, a constant area section and a diffuser. Fig. 1 shows a schematic representation of a steam ejector, illustrating the different parts.

The function of the primary nozzle is to convert the high pressure and low velocity steam delivered to the nozzle into a very high velocity flow with a static pressure lower than that of the low pressure secondary stream. The velocity of steam increases as it enters the nozzle and reaches sonic velocity at the nozzle throat. Beyond this position, the velocity of steam becomes supersonic and further increases until the end of the nozzle where a very low pressure region is created. Under normal operating conditions, the low pressure at the primary nozzle exit causes the secondary stream to enter the mixing chamber where it mixes with the primary jet leaving the nozzle. Mixing of the primary and secondary stream continues and in the constant area zone, the mixing flow experiences a rapid pressure rise due to the action of one or more shock waves which decelerate the flow to a subsonic speed. Further deceleration of the mixed flow occurs in the subsonic diffuser portion of the ejector and at the exit of the diffuser, the fluid reaches the design outlet pressure.

One of the important parameters describing the performance of steam ejectors is the ER (entrainment ratio) which is defined as the ratio of the mass flow rate of the low pressure steam (the secondary mass flow rate) to the mass flow rate of the high pressure steam

* Corresponding author.

E-mail address: Kavous.ariafar@usq.edu.au (K. Ariaifar).

Nomenclature*English letters*

a	speed of sound, m/s
E	total energy, J
k	turbulent kinetic energy, J/kg
M	Mach number
M_c	convective Mach number
P	pressure, Pa
T	static temperature, °C
t	time, s
U	velocity, m/s
x	streamwise distance, m
y	spanwise distance, m

Greek letters

γ	ratio of specific heats
δ	shear layer thickness, m
δ'	growth rate of shear later thickness
δ'_0	growth rate of equivalent incompressible mixing layer
μ	dynamic viscosity, N s/m ²
μ_t	turbulent viscosity, N s/m ²
Π_c	compressibility parameter
ρ	mixture density, kg/m ³
τ_{ij}	stress tensor
ϕ	velocity ratio
Ω	density ratio
ω	specific dissipation rate, 1/s

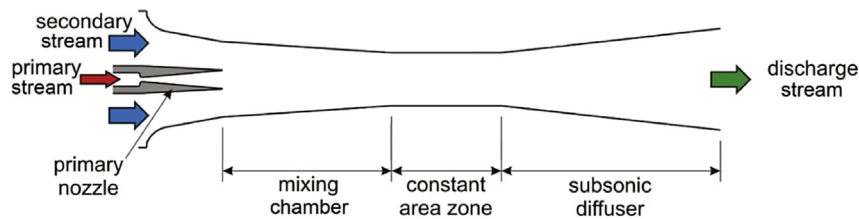


Fig. 1. Illustration showing the different zones within a typical ejector.

(the primary mass flow rate). In broad terms, the higher the entrainment ratio for an ejector, the larger the quantity of low pressure steam that can be recovered, so having a high ER is an advantage for industrial applications. However, another important ejector performance parameter is the critical back pressure which determines the pressure to which the secondary stream can be boosted without any decrease in the ER.

Parameters affecting the ejector performance include the operating conditions, the geometry of the different parts of the ejector and the nozzle exit position within the mixing chamber. Several works are available in the literature investigating the effect of these parameters experimentally and/or numerically using CFD (computational fluid dynamics).

A large number of investigations have focused on the effect of primary nozzle parameters on ejector performance. Riffat et al. [1,2], Eames et al. [3] and Zhu et al. [4] performed parametric studies including work on the axial nozzle position to achieve the highest entrainment ratio. Ruangtrakoon et al. [5,6] investigated the influence of different configurations of primary nozzle on ejector performance with fixed geometry for other parts of ejector. They analyzed the effects on primary stream's pressure, mass flow rate and Mach number and found that expansion angle of the primary stream jet plays an important role on the ejector performance.

There are also some investigations into the influence of the geometry of other parts of the ejector on performance, including length and diameter of the constant area section and the mixing chamber. Varga et al. [7,8] investigated the influence of the area ratio between the constant area section and the primary nozzle throat and also the length of constant area section. Yadav et al. [9] and Ji et al. [10] performed numerical simulations to optimize the geometry of the mixing chamber by investigating the effect of the angle of convergence and the diameter of the mixing chamber.

Research on the effect of operating conditions on the performance of ejector includes the work by Aidoun et al. [11], Wang et al. [12] and Pounds et al. [13]. In these studies, different operating conditions were selected at the inlet boundaries for the boiler and evaporator and at the outlet boundary for the condenser to investigate the effect of these parameters on the entrainment ratio and the coefficient of performance of the ejector.

The CFD technique has been applied in various works to investigate the flow structure and mixing processes inside steam ejectors. Sreevirakul et al. [14] and Yang et al. [15] studied the effect of operating pressures on the formation of shock waves and jet behaviour in ejectors. Yan et al. [16] performed a numerical study on the mixing process in a steam ejector using different nozzle structures. They explained the mixing process through the simulation of streamwise and spanwise vortex distribution in the mixing chamber and their effects on the ejector performance.

It is clear that many factors influence ejector performance, and in particular, the ejector entrainment ratio. However, the influence of mixing effects on the ejector entrainment ratio has not been explicitly defined in prior literature. Obviously mixing between the primary and secondary streams begins immediately downstream of the primary nozzle exit, but previous analytical and computational models have not determined the influence of such mixing effects on the ejector entrainment ratio. Without due consideration of the role of mixing on the entrainment ratio, opportunities for ejector design optimization, and thus improvements in energy efficiency, may be overlooked.

In this work, CFD has been used to investigate the influence that mixing between the primary and secondary streams has on the entrainment ratio of a particular steam ejector. Two approaches to validation of the computational approaches are adopted. The particular ejector is first simulated and its performance compared with experimental data, and then the simulation of the

compressible, turbulent mixing under simplified conditions is assessed with reference to prior experimental data. Having established the reliability of the computational tools, simulations are then performed to investigate the influence of variations in primary and secondary stream conditions on the development of the mixing and ejector entrainment ratio.

2. Mixing layer growth: empirical models

As illustrated in Fig. 2, when two uniform and nearly parallel streams with different values of velocity meet at the trailing edge of a splitter plate, a mixing layer forms at the interface between the two streams. When fully developed, the thickness of the mixing layer δ increases linearly with streamwise distance x , and therefore the growth rate of mixing layer δ' which is defined as $d\delta/dx$ remains constant. The growth rate of the mixing layer that forms between the primary and secondary streams immediately downstream of the primary nozzle exit has the potential to have a direct influence on the ejector entrainment ratio.

Mixing layer growth rate is affected by the velocity ratio across the mixing layer, the density ratio, compressibility effects and the Reynolds number. A number of investigations have been performed to study the effect of these parameters on the mixing layer growth rate. Brown and Roshko [17] conducted experiments for low speed incompressible mixing layers using different gases combinations to generate a large range of density ratios across the mixing layers. Dimotakis [18] also investigated the growth of mixing layers and noted that a mixing layer entrains an unequal amount of fluid from each of the streams. Dimotakis studied the role of the large-scale flow structures in the entrainment of streams in the mixing layer and through geometric and similarity considerations proposed an equation for the spreading of an incompressible mixing layer.

According to Dimotakis [18], a correlation for the growth rate of an incompressible mixing layer δ'_0 as a function of density ratio $\Omega = \rho_2/\rho_1$ and velocity ratio $\phi = U_2/U_1$ across the mixing layer is:

$$\delta'_0 = C_\delta \frac{(1-\phi)(1+\Omega^{1/2})}{2(1+\Omega^{1/2}\phi)} \left\{ 1 - \frac{(1-\Omega^{1/2})/(1+\Omega^{1/2})}{1+2.9(1+\phi)/(1-\phi)} \right\} \quad (1)$$

where C_δ is a constant with a value of around 0.35.

The effect of compressibility on growth rate of shear mixing layer was studied by Bogdanoff [19], Papamoschou and Roshko [20] and Dimotakis [21]. The growth of a compressible mixing layer is reduced relative to that of an incompressible mixing layer with the same velocity and density ratio as the compressible case. Papamoschou and Roshko [20] introduced the so-called convective Mach number (M_c) to correlate compressibility effects on the growth rate of turbulent, compressible mixing layers. The convective Mach number is a mixing layer Mach number with respect to a frame of reference travelling with the large scale structures in the flow field and is defined as:

$$M_c = \frac{\Delta U}{a_1 + a_2} \quad (2)$$

where ΔU is the velocity difference of two streams across the mixing layer and a_1 and a_2 are the speeds of sound on either side of the mixing layer. Papamoschou and Roshko [20] introduced the notion that the compressible mixing layer growth rate δ' normalized by its equivalent incompressible mixing layer growth rate δ'_0 is primarily a function of M_c and concluded that the normalized mixing layer growth rate decreases with increase of convective Mach number due to the compressibility effects.

Slessor et al. [22] subsequently introduced an alternative parameter as Π_c to correlate compressibility effects in the mixing layer:

$$\Pi_c = \max \left[\frac{\sqrt{\gamma_i - 1}}{a_i} \right] \Delta U \quad (3)$$

where i refers to either of streams. Both M_c and Π_c use the difference between the flow speeds on either side of the mixing layer and a representative speed of sound within the layer. Slessor et al. [22] proposed an equation for normalized growth rate of mixing layer as a function of Π_c :

$$\frac{\delta'}{\delta'_0} = \left(1 + \alpha_0 \Pi_c^2 \right)^{-\beta_0} \quad (4)$$

In the above expression, δ'_0 is the growth rate of an incompressible mixing layer with the same density ratio and velocity ratio as the compressible case, α_0 and β_0 are correlating parameters with approximate values of $\alpha_0 = 4$ and $\beta_0 = 0.5$.

There are different possible definitions of the mixing layer thickness. The most commonly used are δ_{10} , δ_s , δ_{pit} and δ_ω [23]. In the δ_{10} definition, which was adopted in the present work, the mixing layer thickness is defined as the distance between two points in the velocity profile where the local velocity is equal to $U_1 - 0.1\Delta U$ and $U_2 + 0.1\Delta U$. This mixing layer thickness, which is also described as the velocity 10% thickness, was used by Samimy and Elliott [24] and Goebel and Dutton [25]. The δ_s or the Stanford thickness, is defined by the distance between two points where the local velocity is $U_2 + \sqrt{0.1}\Delta U$ and $U_2 + \sqrt{0.9}\Delta U$. Chinzei et al. [26] and Barre et al. [27] applied this definition in their works.

The mixing layer thickness based on δ_{pit} is defined as the width of the pitot pressure profile from 5% to 95% of the difference of the free stream values. Papamoschou and Roshko [20], Clemens and Mungal [28] and Slessor [29] used this definition in their experimental works. The last definition, δ_ω or the vorticity thickness is defined to be the distance given by the ratio of the velocity difference ΔU across the layer divided by the maximum slope of the velocity profile $[\partial U/\partial y]_{max}$.

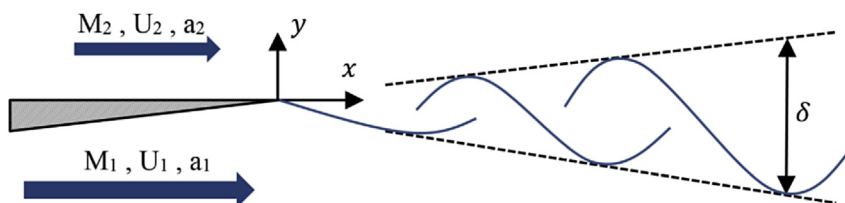


Fig. 2. Schematic of the mixing layer development.

3. Computational model

3.1. Governing equations

The governing equations can be written in compact Cartesian form according to the laws of conservation of mass, momentum and energy:

$$\frac{\partial \rho}{\partial t} + \frac{\partial}{\partial x_i}(\rho U_i) = 0 \quad (5)$$

$$\frac{\partial}{\partial t}(\rho U_i) + \frac{\partial}{\partial x_i}(\rho U_i U_j) = -\frac{\partial P}{\partial x_i} + \frac{\partial \tau_{ij}}{\partial x_j} \quad (6)$$

$$\frac{\partial}{\partial t}(\rho E) + \frac{\partial}{\partial x_i}(U_i(\rho E + P)) = \nabla \cdot \left(\alpha_{eff} \frac{\partial T}{\partial x_i} + U_j(\tau_{ij}) \right) \quad (7)$$

with

$$\tau_{ij} = \mu_{eff} \left(\frac{\partial U_i}{\partial x_j} + \frac{\partial U_j}{\partial x_i} \right) - \frac{2}{3} \mu_{eff} \frac{\partial U_k}{\partial x_k} \delta_{ij} \quad (8)$$

3.2. Turbulence model

In order to simulate the growth of the mixing layer between two streams in a particular ejector, a two equation turbulence model was applied to the whole flow domain based on the SST $k - \omega$ (Shear Stress Transport) model. A benefit of this model is the capacity to simulate free shear flow spreading rates with a reasonable agreement with measurements for far wakes, mixing layers, round and radial jets and is applicable to both wall-bounded flows and free flows [30]. The main governing equations for this model are described as:

$$\frac{\partial(\rho k)}{\partial t} + \frac{\partial}{\partial x_i}(\rho k U_i) = \frac{\partial}{\partial x_j} \left[\left(\mu + \frac{\mu_t}{\sigma_k} \right) \frac{\partial k}{\partial x_j} \right] + G_k - Y_k + S_k \quad (9)$$

$$\frac{\partial(\rho \omega)}{\partial t} + \frac{\partial}{\partial x_i}(\rho \omega U_i) = \frac{\partial}{\partial x_j} \left[\left(\mu + \frac{\mu_t}{\sigma_\omega} \right) \frac{\partial \omega}{\partial x_j} \right] + G_\omega - Y_\omega + D_\omega + S_\omega \quad (10)$$

where k and ω are the turbulent kinetic energy and the specific dissipation rate, respectively. Definitions of terms G , Y , S and D can be found in Ref. [30].

3.3. Numerical solution procedure

The governing equations were solved numerically using a commercial CFD code, FLUENT 14.5 which is based on the control volume method to approximate the governing equations as algebraic equations. A second order upwind scheme was selected to achieve a high order of accuracy at cell faces through a Taylor series expansion of the cell centered solution. The nonlinear governing equations were solved using the coupled implicit solver and the standard wall function was applied near the walls. Convergence of the solution was assumed when two criteria were satisfied:

- the relative difference of mass flow rate between the inlet and outlet boundaries must be less than 10^{-7} ; and
- every type of calculated residual error must be less than 10^{-6} .

4. Ejector geometry and boundary conditions

The main dimensions of the particular steam ejector, which was designed and operated in a refrigeration system by Al-Doori [31], are summarized in Table 1. The computations were performed using an axisymmetric domain in order to reduce the CPU cost and simulation time.

The primary NXP (nozzle exit position) was at +6 mm. NXP is defined as the distance between the primary nozzle exit plane and the mixing chamber inlet plane. Fig. 3 shows the computational element configuration with a close-up view of the mesh elements near the primary nozzle and start of the mixing chamber. The computational grid was generated based on the structured quadrilateral elements. In order to check the sensitivity of the results to the mesh density, three different mesh densities were generated: the coarse mesh density with 14,400 elements, the medium with 42,900 and the fine with 78,500 elements. The results showed that the difference for the net mass flow rate for medium and fine level was less than 1%, and hence the medium mesh was selected with consideration of the computational costs while providing sufficient cells in the mixing chamber. The medium mesh provided a minimum of 4 cells per mm in the transverse direction and this resolution is required where mixing of the primary and secondary streams occurs in order to calculate the growth rate of mixing layer according to discussion of Section 5.

Pressure inlet boundaries were selected for the primary and secondary streams entering the ejector and a pressure outlet was used for the discharge stream leaving the ejector. Inlet boundary conditions were set based on the saturated vapour conditions of steam, to match experimental operating conditions [31]. The temperature and pressure values for different ejector operating conditions as applied to the boundary conditions in the simulations are given in Table 2.

5. Validation of the numerical method

In this section, validation of the numerical method is first presented for the static pressure distribution along the ejector wall and then for the entrainment ratio of the ejector described in Section 4. The principal focus of the present work is the effect of mixing of the primary and secondary flows on the ejector entrainment ratio. The rise in static pressure that occurs within the ejector is influenced to some degree by the mixing process, but a more convincing case for validation is established if the correct simulation of static pressure distribution and entrainment ratio are simultaneously achieved. However, the entrainment ratio of an ejector is not solely dictated by mixing effects. Therefore as a further validation of the CFD tool applied in this work, the mixing layer growth rates for a configuration of two planar, parallel streams with different velocities and densities are simulated and compared to experimental results. Although this planar mixing layer configuration does not actually

Table 1
Geometrical details of the steam ejector.

Geometrical parameters	Size (mm)
Primary nozzle inlet diameter	10
Primary nozzle throat diameter	3.2
Primary nozzle outlet diameter	13.6
Primary nozzle divergent length	59.5
Mixing chamber inlet diameter	37
Mixing chamber length	155
Constant area zone diameter	25.4
Constant area zone length	75
Subsonic diffuser length	210
Subsonic diffuser outlet diameter	50

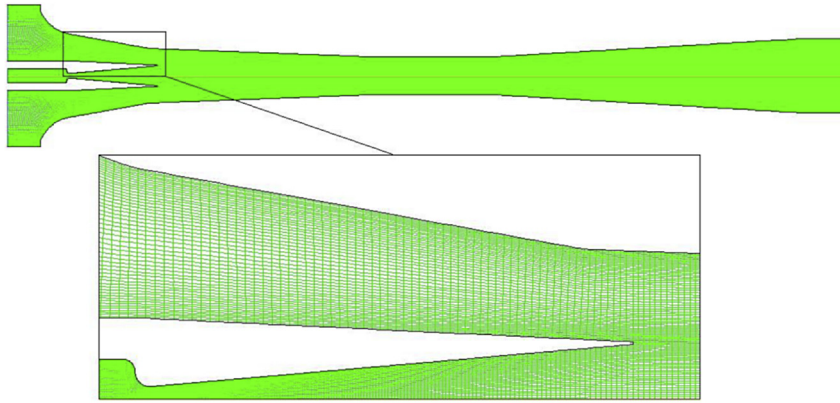


Fig. 3. Computational grid used for ejector simulations in the case of the medium mesh density.

Table 2
Steam pressure and temperature values for the ejector boundaries.

Stream	Temperature (K)	Pressure (kPa)
Primary	383, 403, 423	143.3, 270, 476
Secondary	283, 287, 291	1.2, 1.6, 2.1
Discharge	–	4.2, 6

occur in the ejector, it provides a direct test of the computational model in the simulation of compressible mixing under conditions directly relevant to the ejector environment.

5.1. Static pressure distribution and entrainment ratio

Fig. 4 shows the static pressure distribution along the simulated ejector wall compared with experimental data for operating pressures of 270 kPa and 1.2 kPa for the primary and secondary streams and a discharge pressure of 6 kPa. As it is observed from Fig. 4, pressure profiles from the experiment and CFD method are reasonably well matched. The static pressure profile from CFD

simulation underestimates the experimental data with a relative error of about 11% in the mixing chamber and constant area zones while it overestimates the static pressure with a relative error of about 6% in the subsonic diffuser during the pressure rise. Simulations were also performed for other operating conditions where corresponding experimental data was available for comparison and the result in Fig. 4 is representative of the level of agreement achieved in the other conditions. The treatment of the ejector steam flow using ideal gas model has the potential to contribute to the observed differences between the experimental data and the simulations. The simulated pressure profile along the ejector wall is consistent with the level of agreement between simulations and experiments reported in the literature [32,33] where the ideal gas assumption was also used to model steam within the ejector.

Table 3 presents the values of entrainment ratio obtained with the CFD simulations and corresponding values of available experimental data. Simulations were performed for different primary stream pressures of 143.3, 270 and 476 kPa, while secondary and discharge stream pressures remained constant at 1.6 kPa and 4.2 kPa, respectively. The ejector entrainment ratio decreases with increases of the primary stream pressure over the current operating

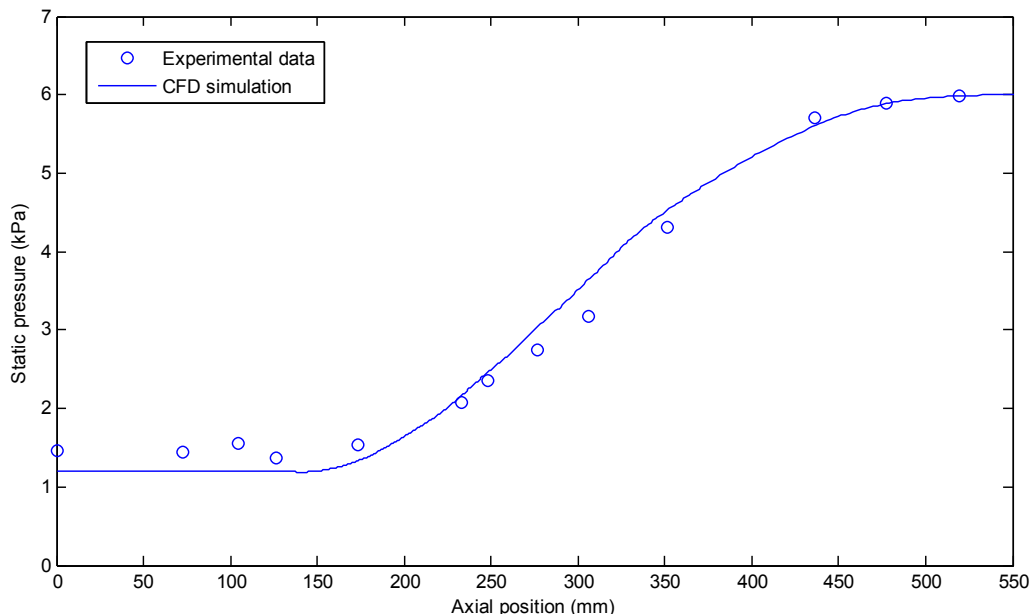


Fig. 4. Static pressure distribution along the ejector wall for primary, secondary, and discharge pressures of 270 kPa, 1.2 kPa, and 6 kPa respectively.

Table 3
Experimental data [31] and CFD results for the ejector entrainment ratio.

Primary stream pressure (kPa)	Secondary stream pressure (kPa)	Discharge stream pressure (kPa)	Entrainment ratio (Exp.)	Entrainment ratio (CFD)	Simulation error (%)
143.3	1.6	4.2	0.44	0.486	10.4
270			0.33	0.355	7.5
476			–	0.212	–

conditions. This is a well-established effect observable in most ejectors operating in a double-choked or critical mode. In the case of this particular ejector, the simulated entrainment ratio decreases from 0.486 at the primary stream pressure of 143.3 kPa to a value of 0.212 at the pressure of 476 kPa. Differences between the CFD results and available experimental data for the ejector entrainment ratio are 10.4% and 7.5% for the primary stream operating pressures of 143.3 and 270 kPa, respectively. Contributions to these errors will arise from the ideal gas assumption for steam behaviour and the application of *SST k- ω* turbulence model for the ejector simulation.

This validation work demonstrates the capacity to simulate the ejector flow environment, as represented by the pressure rise process and entrainment ratio, with reasonable fidelity: differences between the simulated and physical values are in the vicinity of 10%. The level of agreement between the experimental data and the simulations in this case provides the basis for claiming that subsequent ejector CFD simulations are likely to reflect gross aspects of the pressure rises and entrainment ratios that are achievable in physical ejectors at other operating conditions, despite significant modelling approximations such as the application of the ideal gas model in the steam ejector.

5.2. Mixing layer development of two parallel streams

The validation work with the simulation of the static pressure and entrainment ratio (Section 5.1) provides some indirect evidence that the computational software can simulate the mixing correctly, but a more direct assessment of its performance in the simulation of mixing is also needed. Before simulating the growth of the mixing layer formed between the primary and secondary streams in the ejector, it was deemed important to first demonstrate the ability of FLUENT software and the *SST k- ω* turbulent model to simulate the mixing layer growth rate under compressible flow conditions for which experimental data is available. For this purpose, compressible mixing layers formed between two free streams were simulated and the growth rate defined.

As illustrated in Fig. 5, when two streams with different values of velocity meet, a mixing layer with a thickness of δ develops. The growth of this layer is influenced by turbulent effects and the

Table 4
Flow properties for each stream in the mixing layer simulation.

U_1 (m/s)	T_1 (K)	a_1 (m/s)	U_2 (m/s)	T_2 (K)	a_2 (m/s)	M_c
1715	293	343	1348	180.9	269.6	0.6
			1242.3	153.6	248.4	0.8
			1143.7	130.2	228.7	1
			1051.5	110.1	210.3	1.2
			965	92.7	193	1.4
			883.8	77.8	176.8	1.6
			807.3	65	161.6	1.8

compressibility of the mixing flow. In a practical mixing layer configuration, boundary layers will develop on the splitter plate which separates the two streams upstream of the domain illustrated in Fig. 5, however the computational domain considered here has uniform inlet conditions across the two streams. As the streams contact the upper and lower walls, oblique shock waves which are attached to the leading edge of these walls are generated due to the displacement thickness of boundary layers that grows on the walls. Another pair of oblique shock waves is generated at the trailing edge of the splitter plate due to the growth of the mixing layer.

In order to simulate the mixing layer growth, a 2-D planar computational domain with a rectangular shape of 150 mm in length and 100 mm in height was used. The height of computational domain was selected large enough to prevent the oblique shock waves created by the upper and lower walls from disturbing the growth of the mixing layer and the deduction of the local thickness values of the mixing layer. In order to have approximately the same shock wave angles within the domain and thereby ensure a zone free of disturbances that was uniform in size across all simulated conditions, in-flow boundary conditions of velocity and temperature were selected so that each stream enters the computational domain with a Mach number of 5. (The angle of shock waves formed by the boundary layers and the mixing layers is primarily a function of the Mach number of the flow entering the domain, although the displacement thickness of the boundary and mixing layers do also have an effect.)

Three different mesh densities were trialed to confirm the mesh independence of the results: the coarse mesh with 54,400 cells, the

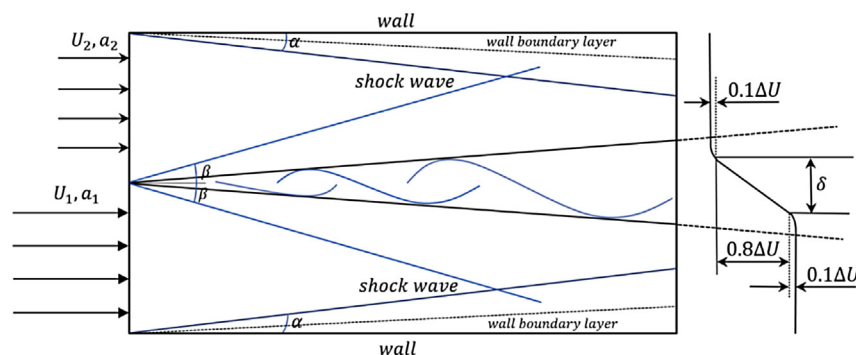


Fig. 5. Illustration of mixing layer development and definition of the mixing layer thickness δ based on the velocity profile.

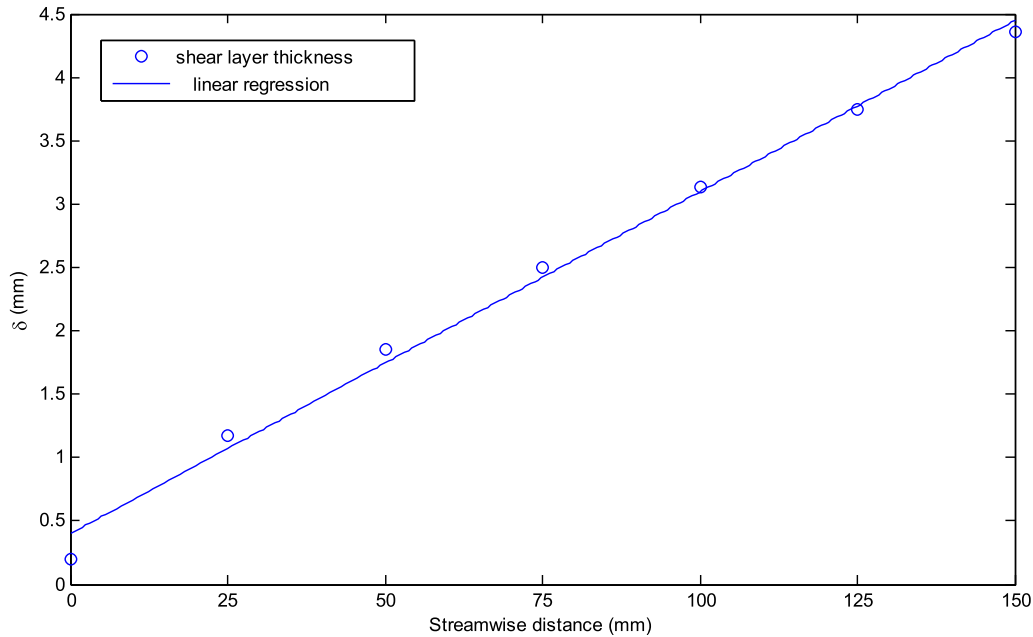


Fig. 6. Mixing layer thickness variation with streamwise distance for the $M_c = 1.4$ case.

medium mesh with 108,600 cells, and the fine mesh with 217,100 cells. For the case where $M_c = 1.4$ (see Table 4), simulated values of the mixing layer thickness for a particular downstream distance of 75 mm for the coarse, medium and fine mesh densities were 1.353, 2.536 and 2.557 mm, respectively. The medium mesh density was then selected for the remaining simulations with consideration of the computational costs and close agreement with the fine mesh result (less than 1% difference).

Two streams of air, each treated as an ideal gas with different velocities and temperatures were selected to generate different M_c conditions as specified in Table 4. Simulations were performed for $M_c > 0.6$ since these conditions are representative of the compressibility encountered during the mixing of the primary and secondary streams in a steam ejector. (Calculated M_c values based on ejector simulations immediately downstream of the primary nozzle exit are higher than 0.6, and this is discussed in Section 6.) Boundary conditions for the simulations were specified as 'pressure inlet' for two streams entering the domain and 'pressure outlet' for the partially mixed discharge stream. The value of the static pressure on both pressure inlets was 1000 Pa and the static temperature in the primary stream was specified as 293 K. At the pressure outlet a value of 100 Pa was used. Total pressures and temperatures for the two inlet streams were calculated using gas dynamics equations. Table 4 presents the values of velocity and temperature for each stream together with calculated M_c for each case.

Velocity profiles at seven streamwise distances were extracted from the simulation results and were analyzed to determine the mixing layer thickness based on the definition of 80% of the velocity difference as illustrated in Fig. 5. An illustrative result showing the simulated growth of mixing layer thickness δ for the $M_c = 1.4$ case together with a linear regression is presented in Fig. 6 which illustrates there is a nearly linear growth for mixing layer thickness with the streamwise distance.

The growth rate of the mixing layer thickness δ' was determined from the slope of growth line for the mixing layer thickness. The normalized growth rate of the mixing layer δ'/δ'_0 was then calculated and compared with available experimental data reported by the literature as shown in Fig. 7. Following steps were used in order to calculate δ'/δ'_0 :

1. Determine the value of δ' for a given M_c (as explained above for the $M_c = 1.4$ case)
2. Calculate the velocity ratio ϕ and density ratio Ω using the given values in Table 4. (Density is calculated using the values of pressure and temperature and the ideal gas relationship for air.)
3. Substitute the calculated values of ϕ and Ω in Eq. (1) in order to calculate δ'_0 .
4. Calculate the ratio between δ' and δ'_0 .
5. Repeat steps 1–4 for the range of different M_c values.
6. Plot δ'/δ'_0 for each M_c .

As seen in Fig. 7, the computational simulation results are in reasonable agreement with experimental data. There is substantial scatter in the experimental results and one contributing factor here is the application of different definitions for the calculation of the mixing layer thickness. Nevertheless, the simulations performed for this validation exercise demonstrate reasonable agreement with the experimental data over this range of convective Mach numbers: the trend of decreasing normalised growth rate with increasing M_c is demonstrated, although differences between the CFD results and individual experiments is as high as 32.4% in the worst case. The standard deviation between the experimental data and the CFD simulation over this range of convective Mach numbers is 11.2%. The CFD is thereby confirmed as an adequate approach in simulating the development of mixing in the present steam ejector applications and the magnitude of errors that are likely to arise is consistent with those observed in the simulation of static pressures and ejector entrainment ratio of around 10%.

6. Ejector mixing layer growth

In this section, it is demonstrated that higher mixing layer growth rates accompany higher values of entrainment ratio for the ejector. This is achieved by first discussing the analysis of mixing layer development in the ejector (Section 6.1) and then presenting results showing mixing layer development for different conditions in the primary stream (Section 6.2) and the secondary stream (Section 6.3).

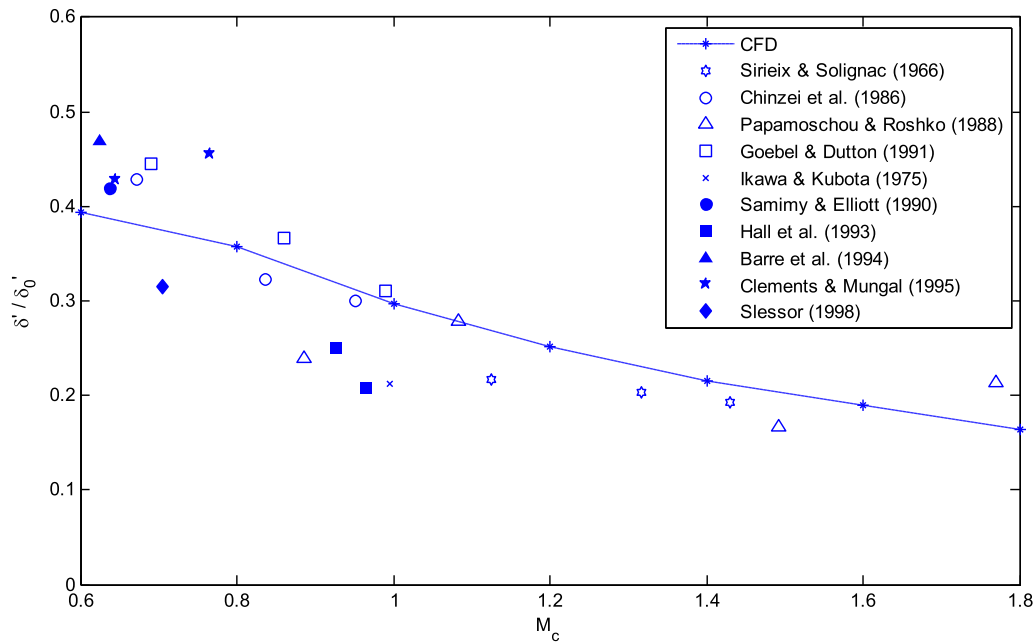


Fig. 7. Normalized mixing layer growth rate as a function of convective Mach number.

6.1. Approach to the analysis

The mixing of the primary and secondary streams starts at the end of the primary nozzle, where the two streams first come in contact. The growth rate of the mixing layer will change with the values of the velocity and density of the two streams. That is, the growth rate of the mixing layer will change with different operating conditions of the ejector. Changes in the mixing layer growth rate under different ejector operating conditions have the potential to affect the ejector entrainment ratio.

Fig. 8 shows the development of the velocity vectors downstream of the primary nozzle exit in the mixing chamber of the ejector at a particular operating condition. The mixing layer development is illustrated by the broken lines that have been added to this figure. A more rapidly growing mixing layer implies additional entrainment of mass into the mixing layer which leads to the induction of additional secondary stream mass into the mixing chamber and thus an increase in the entrainment ratio of the ejector. The mixing layer growth rate is determined at different

ejector operating conditions to assess the effect of growth rate on the ejector entrainment ratio.

The primary and secondary flow conditions adjacent to the mixing layer are the conditions that should be used in calculating the convective Mach number. Since there can be substantial changes in the flow conditions immediately downstream of the primary nozzle exit, the convective Mach number should be calculated based on those local conditions. Fig. 9 provides a schematic representation of the primary and secondary streams in the vicinity of the primary nozzle exit. Depending on the ejector operating condition, the primary stream at the nozzle exit will generally adjust its static pressure to some degree in order to match the static pressure in the secondary stream. At the same time, however, the secondary stream is generally accelerating in the mixing chamber, so its static pressure is decreasing from some initial value at the nozzle exit plane (P_{2i}) to the value it adopts at the secondary stream choking condition (P_2). It is assumed that the static pressure of the primary stream is altered by isentropic waves (an isentropic expansion fan is illustrated in Fig. 9). The static

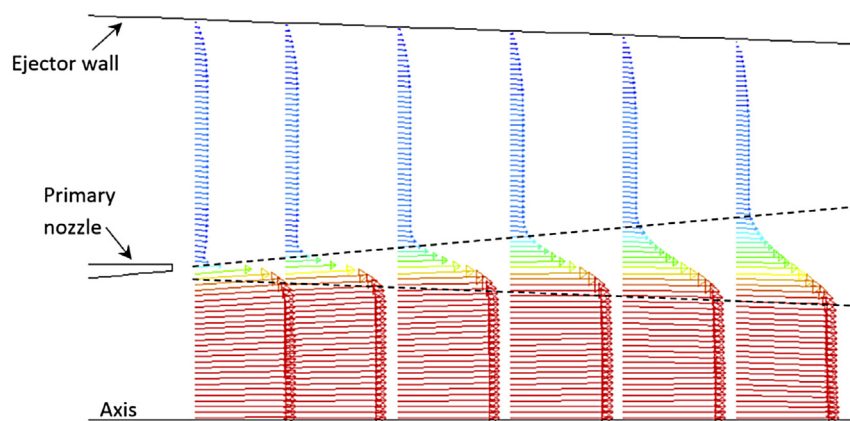


Fig. 8. Velocity vectors in the mixing chamber indicating mixing layer development from the computational simulations for the case of 270 kPa for the primary pressure and 1.6 kPa and 4.2 kPa for the secondary and discharge pressures, respectively.

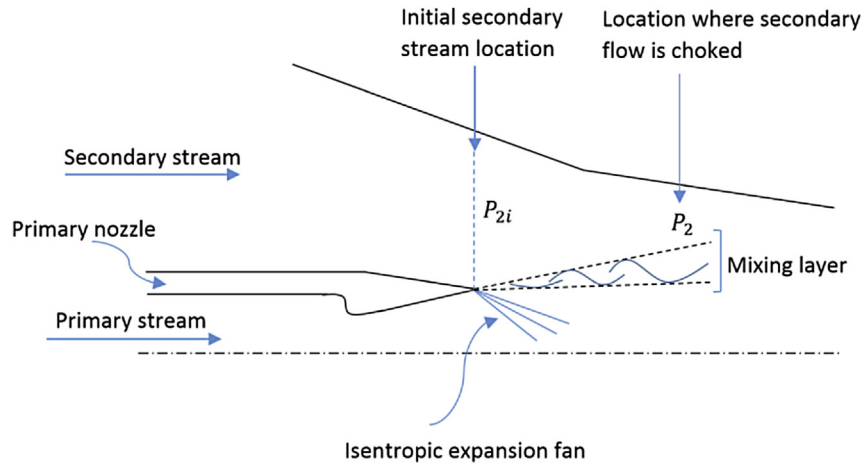


Fig. 9. Schematic illustration of the flow features in the vicinity of the primary nozzle exit.

pressure of the primary stream will initially be matched to P_{2i} close to the nozzle exit, but will be matched to P_2 further downstream. Therefore two different values of M_c (or Π_c) can be calculated for the mixing layer depending on the matching of the primary stream to either P_{2i} or P_2 and these two values will set the limits on applicable values of M_c (and Π_c) in the ejector. In the following sections, the reported values of M_c and Π_c are based on the average of values corresponding to P_{2i} and P_2 .

The growth rate of the mixing layer in the ejector δ' can be determined from the CFD simulations by analysing the velocity profile according to the approach outlined in Section 5.2 for the case of the planar mixing layer. Alternatively, an empirical estimate of the mixing layer growth rate can be obtained using the equations presented in Section 2 according to the following steps:

1. Calculate δ'_0 using Eq. (1) for each operating condition with the values of velocity and density for the primary and secondary streams at the end of the primary nozzle with isentropic adjustments for the pressure matching between the primary and secondary streams.
2. Calculate Π_c using Eq. (3) for each operating condition with the values of speed of sound for the primary and secondary streams at the end of the primary nozzle, again with isentropic pressure-matching adjustments. (The ratio of specific heats in the ideal gas steam ejector calculations is taken as $\gamma = 1.3$ for both the primary and secondary streams in this work.)
3. Substitute calculated values of δ'_0 and Π_c in Eq. (4) to provide an empirical estimate of δ' .

In the following sections, the mixing layer growth rate in the ejector is determined using both the computationally-simulated velocity profiles as well as the empirical method to illustrate the level of agreement that can be attained in the ejector application.

6.2. Mixing layer growth rate at different operating conditions for the primary stream

In order to investigate the changes of the mixing layer growth rate with different operating conditions for the primary stream, simulations were performed with stagnation pressures of 143.3, 270 and 476 kPa for the primary stream and a stagnation pressure of 1.6 kPa for the secondary stream and a static pressure of 4.2 kPa for the discharge streams. In each case, stagnation temperature values for the primary and secondary streams used in the

simulations were determined on the assumption that the flows in each case were saturated vapour, as was the case in the experiments.

The values of velocity, static pressure, speed of sound and density at the primary nozzle exit plane are presented in Table 5 for each stream and each operating condition. The mixing layer compressibility parameters M_c and Π_c are calculated through the static pressure matching approach described in Section 6.1.

From Table 5, it is clear that the mixing layer compressibility (as reflected in the value of M_c and Π_c) increases with increase of the primary stream pressure. Accompanying this increased compressibility, the mixing layer growth rate decreases. Calculated values of δ' based on the empirical method are 0.0763, 0.0618 and 0.0517 for operating conditions of 143.3, 270 and 476 kPa, respectively. Values of δ' based on the CFD simulations (the velocity profile analysis) for these operating conditions are 0.0706, 0.059 and 0.0465. Thus, the empirical and computational methods for estimating the mixing layer growth rate indicate a decrease of approximately 8% and 11% respectively over this range of increase in the primary stream pressure. For each of the three primary stream pressure cases, the empirical and computational methods give mixing layer growth rate values that agree to within approximately 11%, consistent with the validation work presented in Section 5.2.

Fig. 10 provides further details of the development of the mixing layer thickness as deduced from the simulated velocity profiles for each case. The slope of line fitted to the mixing layer thickness results in Fig. 10 is the value of the mixing layer growth rate δ' (CFD) as reported in Table 5. The mixing layer thickness determined from the velocity profile at the first station downstream of the nozzle exit (the 1 mm station) does not appear to vary with the primary stream stagnation pressure in a consistent manner. However, at each condition, the simulated growth of the mixing layer thickness is well approximated by the linear model, as observed in Fig. 10.

Table 5 indicates that both mixing layer compressibility parameters M_c and Π_c increase with an increase in the primary stream stagnation pressure and that a decrease in the mixing layer growth rate accompanies this increase in mixing layer compressibility. With less secondary stream entrainment into the mixing layer as the primary stream stagnation pressure increases, a decrease in the ejector entrainment ratio is the expected result. However, there are also changes in the secondary stream flow rate that are driven by changes in pressure differences (inviscid effects) that operate simultaneously with viscous, mixing layer entrainment effects. The relative significance of inviscid, pressure-driven

Table 5
Simulated mixing layer results at different primary stream pressures.

Primary stream pressure	Stream	Velocity (m/s)	Static pressure (kPa)	Sound speed (m/s)	Density (kg/m ³)	M_c	Π_c	δ' (Emp.)	δ' (CFD)	ER (CFD)	ER (Exp.)
143.3 kPa	Primary	1027	0.95	268	0.0167	1.118	1.503	0.0763	0.0706	0.486	0.44
	Secondary	142	1.47	410	0.0113						
270 kPa	Primary	1060	1.59	272	0.0277	1.226	1.696	0.0618	0.059	0.355	0.33
	Secondary	141	1.48	411	0.0113						
476 kPa	Primary	1089	2.65	277	0.0443	1.33	1.885	0.0517	0.0465	0.212	–
	Secondary	138	1.48	411	0.0114						

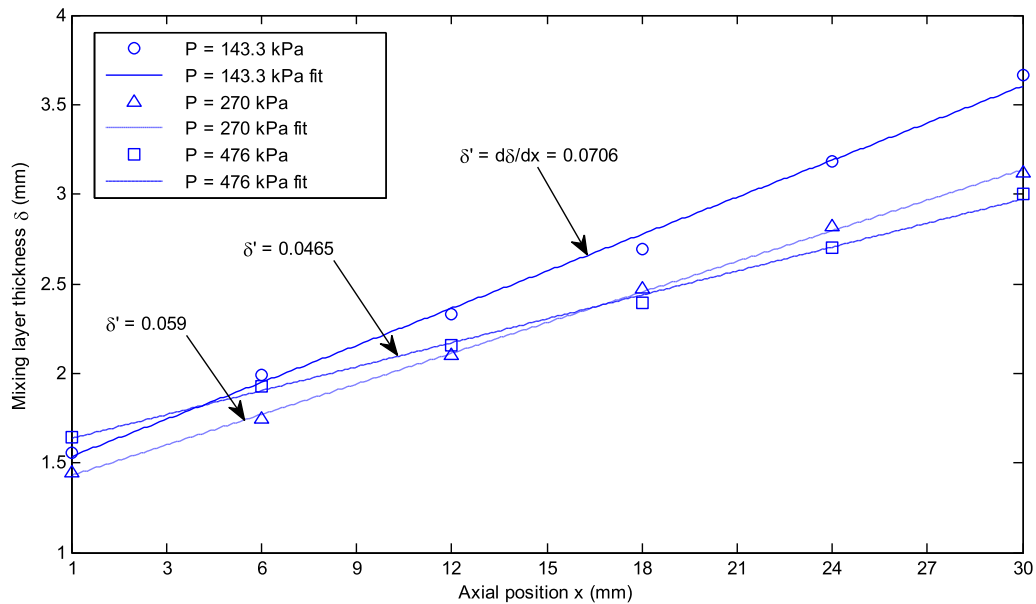


Fig. 10. Mixing layer development at different operating conditions for the primary stream with the secondary stream stagnation pressure of 1.6 kPa.

entrainment and viscous, mixing layer entrainment on the overall entrainment ratio of the ejector will be discussed in Section 7.

6.3. Mixing layer growth rate at different operating conditions for the secondary stream

To study the change in the mixing layer development at different secondary stream operating conditions, simulations were performed at values of 1.2, 1.6 and 2.1 kPa for the stagnation pressure of the secondary stream and with a constant stagnation pressure of 270 kPa for the primary stream and 4.2 kPa for the static pressure of the discharge streams. Again, stagnation temperature values for the simulations were determined from the assumption that saturated vapour conditions prevail, as was the case in the experiments.

The values of velocity, static pressure, sound speed and density from CFD simulation at the end of the primary nozzle are presented in Table 6 for each stream at different operating conditions.

Table 6
Simulated mixing layer results for different secondary stream pressures.

Secondary stream pressure	Stream	Velocity (m/s)	Static pressure (kPa)	Sound speed (m/s)	Density (kg/m ³)	M_c	Π_c	δ' (Emp.)	δ' (CFD)	ER (CFD)	ER (Exp.)
1.2 kPa	Primary	1060	1.59	272	0.0277	1.275	1.789	0.0562	0.0551	0.297	–
	Secondary	136	1.12	408	0.0087						
1.6 kPa	Primary	1060	1.59	272	0.0277	1.226	1.696	0.0618	0.059	0.355	0.33
	Secondary	141	1.48	411	0.0113						
2.1 kPa	Primary	1060	1.59	272	0.0277	1.185	1.611	0.0683	0.0631	0.404	–
	Secondary	143	1.94	413	0.0147						

Calculated values of δ' using the empirical equations together with those determined from the simulated velocity profiles are also presented in this table. Fig. 11 shows the mixing layer thickness δ at 6 transverse locations downstream of the primary nozzle for each operating conditions. The mixing layer growth rate δ' is calculated as the slope of linear regression for each case in the simulated velocity profile method. Agreement between the simulated velocity profile method and the empirical values for the mixing layer growth rate is comparable to that obtained in Section 6.2 for the case of varying primary stream conditions.

From Table 6, the ejector entrainment ratio increases with increasing secondary stream pressure: it rises from 0.297 for the secondary stream pressure of 1.2 kPa to a value of 0.404 at pressure of 2.1 kPa. It is reasonable that for a fixed primary stream stagnation pressure and ejector discharge pressure, an increase in the secondary stream stagnation pressure should yield and increase in secondary stream mass flow rate (and hence, an increase in ejector entrainment ratio) by virtue of the increased pressure difference

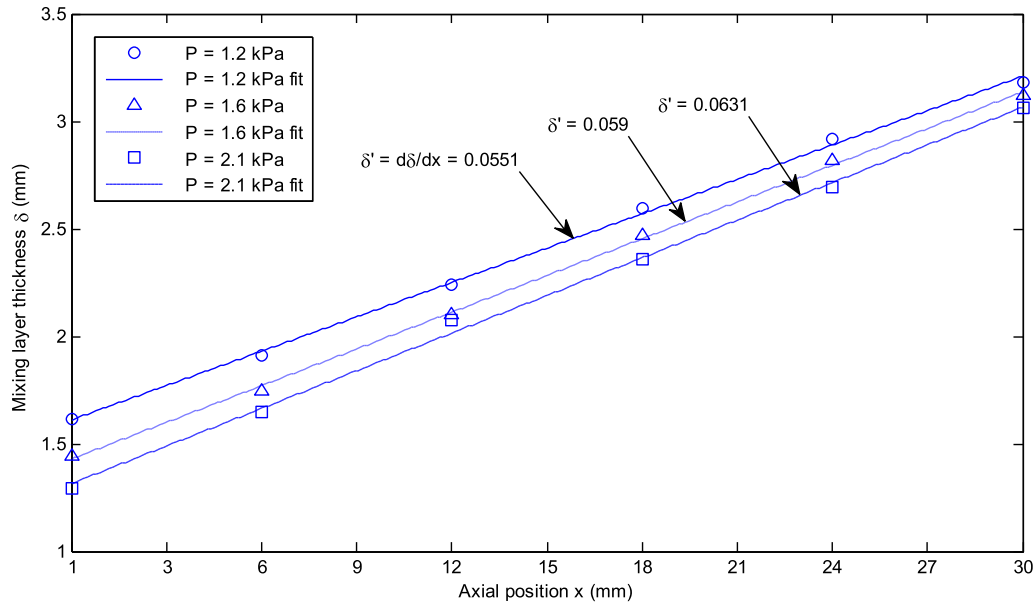


Fig. 11. Mixing layer development at different operating conditions for the secondary stream with the primary stream stagnation pressure of 270 kPa.

between the secondary stream inlet and the mixing chamber. But it is important to note that the results in Table 6 and Fig. 11 show the mixing layer growth rate also increases with the increase of secondary stream pressure. It is therefore conceivable that enhanced entrainment into the mixing layer is making a contribution to the observed increase in the ejector entrainment ratio with increasing secondary stream pressure. Determining the significance of the mixing layer entrainment and distinguishing it from the contribution due to the inviscid, pressure-driven effects is the focus of the following section.

7. Relative significance of mixing layer growth and inviscid effects

In the previous section, it was demonstrated that higher values of ejector entrainment ratio are accompanied by faster growth of the mixing layer. However, the relationship between the ejector mixing layer growth rate and the ejector entrainment ratio was not defined. In this section, the inviscid, pressure-driven influence on the ejector entrainment ratio is decoupled from the contribution due to viscous, shear-driven effects in the mixing layer.

Ejector computational simulations were performed over a range of operating conditions, firstly using a completely inviscid solver, and then using a turbulent ($SST k - \omega$) model as applied in previous sections of this paper, except with a slip-wall condition imposed on the ejector wall boundary. Simulations were performed using a single condition for the primary stream of 270 kPa stagnation pressure with saturated temperature of 403 K and discharge stream of 3 kPa while the secondary stream's pressure was varied from 0.94 kPa to 2.65 kPa. The purpose of the inviscid simulations was to establish the entrainment ratio performance of the ejector in the absence of any influence due to mixing layer development. Any variations in the entrainment ratio in the inviscid cases are therefore attributable entirely to pressure-driven effects. The entrainment ratio achieved with the turbulent simulations with the slip wall can then be directly compared with the inviscid simulations to define the portion of the ejector entrainment ratio directly attributable to the development of mixing between the primary and secondary streams. The slip wall boundary condition has been used for the turbulent simulations

for comparability to the inviscid simulations: the slip wall boundary condition was effectively in operation in the inviscid simulations as well.

The results of these simulations are summarized in Table 7. Simulations were performed with 5 different secondary stream stagnation pressures with stagnation temperatures corresponding to the saturation values. For all simulations, the primary stream stagnation pressure was kept at 270 kPa and the discharge pressure was kept low enough to ensure choking of the secondary stream was achieved for each of the conditions. In Table 7, the column entitled "change in ER" represents the difference between viscous and inviscid simulations for ejector entrainment ratio and indicates the portion of the ER attributable to mixing effects. The column entitled "relative change in ER" is the quantity $\Delta ER/ER$.

In the following tables, M_c and Π_c was calculated using the method explained in Section 6.1 and Fig. 9. The mixing layer growth rate, however, was calculated using the empirical equation presented in Eq. (4).

The results in Table 7 indicate that as the secondary stream pressure increases, the change in ER increases and the relative change in ER decreases. For the secondary stream pressure of 0.94 kPa, about 35% of the entrainment ratio is due to the mixing of the primary and secondary streams while this portion is reduced to about 22% when the secondary stream pressure is increased to 2.65 kPa. The ejector entrainment ratio is increasingly influenced by pressure driven effects when secondary stream pressure increases. However, for lower secondary stream pressures, mixing layer effects have an increasing influence on the ejector entrainment ratio.

In order to simulate a wider range of mixing layer conditions as reflected in the compressibility parameters (M_c and Π_c) and observe the influence on the ER, an additional set of simulations was performed with the same operating condition as used for the Table 7 results but with doubled the absolute stagnation temperature for each secondary stream pressure. Table 8 summarizes the results of these simulations. Similar trends are observed for the conditions of Tables 7 and 8.

Fig. 12 shows the simulated change in entrainment ratio ($\Delta ER = ER - ER_i$) plotted against mixing layer growth rate (δ')

Table 7
Entrainment ratios for various secondary stream stagnation pressures with saturation temperatures.

Secondary stream stagnation conditions kPa (K)	Entrainment ratio		Change in ER (ΔER)	Relative change in ER (%)	Π_c	M_c	δ' (Emp.)
	Inviscid simulation (ER_i)	Turbulent simulation with slip wall condition (ER)					
0.94 (279)	0.166	0.254	0.088	34.6	1.87	1.316	0.0518
1.2 (283)	0.221	0.323	0.102	31.6	1.794	1.279	0.0565
1.6 (287)	0.278	0.381	0.103	27	1.698	1.229	0.0622
2.1 (291)	0.35	0.462	0.112	24.2	1.618	1.188	0.0692
2.65 (295)	0.448	0.571	0.123	21.5	1.543	1.148	0.0752

Table 8
Entrainment ratios for various secondary stream stagnation pressures with elevated temperatures.

Secondary stream stagnation conditions kPa (K)	Entrainment ratio		Change in ER (ΔER)	Relative change in ER (%)	Π_c	M_c	δ' (Emp.)
	Inviscid simulation (ER_i)	Turbulent simulation with slip wall condition (ER)					
0.94 (558)	0.115	0.183	0.068	37.1	1.624	0.91	0.0484
1.2 (566)	0.156	0.228	0.072	31.6	1.559	0.887	0.0525
1.6 (574)	0.197	0.274	0.077	28.1	1.464	0.848	0.0571
2.1 (582)	0.246	0.337	0.091	27	1.358	0.805	0.0615
2.65 (590)	0.314	0.421	0.107	25.4	1.268	0.772	0.0657

scaled by the viscous entrainment ratio (ER) with the data taken from in Table 7 (labelled 'Table 7 results' in Fig. 12) and Table 8 (labelled 'Table 8 results'). The intention of this plot is to establish a correlation that reflects the fraction secondary stream mass flux that is attributable to the mass entrained into the growing mixing layer. The value ER is used to scale δ' on the abscissa rather than using the mixing layer growth rate alone on the abscissa because the mixing layer growth rate will have a non-zero value, even when there is no secondary stream entrainment.

The least squares curve fit to the simulation data points shown in Fig. 12 is given by:

$$\Delta ER = 0.42(\delta' * ER)^{0.39} \tag{11}$$

Although there is a paucity of data approaching the origin in Fig. 12, the power-law form was adopted because it is recognized that when the viscous entrainment ratio is zero (there is no secondary flow in the ejector), there can be no change of ejector

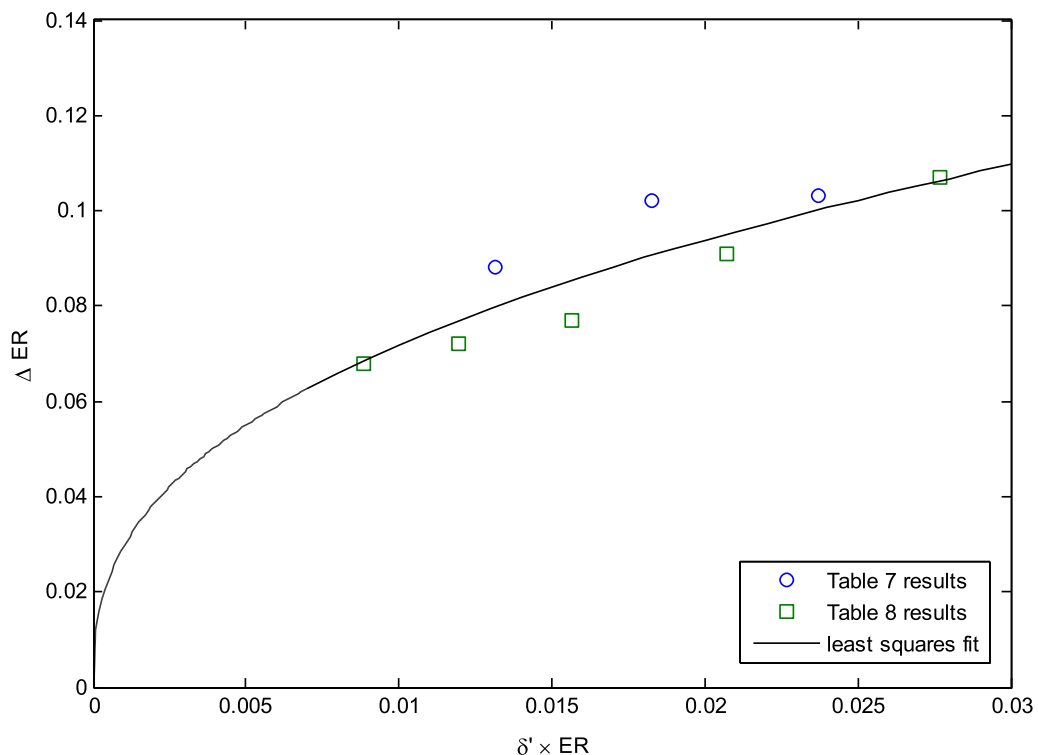


Fig. 12. Portion of ejector entrainment ratio attributable to mixing layer growth rate.

entrainment ratio that is attributable to mixing layer development. From Fig. 12 it is observed that the portion of the ejector entrainment ratio attributable to mixing effects generally increases with the mixing layer growth rate and the viscous entrainment ratio.

8. Conclusion

The present work has focused on the role of mixing of the primary and secondary streams on the ejector entrainment ratio. The ejector entrainment ratio is primarily influenced by two factors: pressure-driven effects and mixing effects. Computational simulations based on inviscid and viscous solvers were performed to specify the influence of these two factors on the entrainment ratio under some typical operating conditions for a steam ejector. Simulation results for the entrainment ratio based on the inviscid solver were used to determine the entrainment ratio due to the pressure driven effects and the increase in entrainment ratio achieved with the viscous simulation results was then used to identify the portion of the entrainment ratio associated with mixing effects.

The computational simulation methods used in this work were validated using the static pressure distribution and the entrainment ratio measured in a particular ejector. In addition, the simulation of mixing layer growth rate for two parallel streams with different values of velocity and temperature has been assessed using experimental data reported elsewhere in the literature. Errors in static pressure, entrainment ratio and mixing layer growth rate of around 10% were identified through these validation exercises. The level of agreement between the simulation results and experimental data in these validation exercises indicates the degree of confidence that can be placed on the results from the subsequent ejector simulations.

Based on the results of the simulations and the experimental data, ejector entrainment ratio increases with a decrease of the primary stream pressure (assuming saturated vapour reservoir conditions) with constant operating conditions for the secondary and discharge streams. Such a decrease in primary stream pressure is accompanied by a decrease in the mixing layer compressibility effects and an increase of the mixing layer growth rate. In addition, the ejector entrainment ratio also increases with an increase of the secondary pressure (assuming saturated vapour reservoir conditions) with constant conditions for the primary and discharge streams. In this case, mixing layer compressibility effects also decrease with the rise of the secondary stream pressure and this is also accompanied by an enhancement of the mixing layer growth rate.

When the secondary stream pressure increases for fixed operating conditions for the primary and discharge streams, the ejector entrainment ratio is increasingly influenced by the pressure driven effects and mixing effects become less significant. For example, about 35% of the entrainment ratio is due to the mixing effects for the secondary stream stagnation conditions of 0.94 kPa and 279 K, but this portion is reduced to about 22% when the secondary stream stagnation conditions are 2.65 kPa and 295 K. The ejector entrainment ratio is increasingly influenced by pressure driven effects when secondary stream pressure increases. From the computational simulations, the portion of ejector entrainment ratio attributable to mixing effects has been correlated with the rate of compressible mixing layer growth. By defining the influence of mixing between the primary and secondary stream on the ejector entrainment ratio, a more reliable basis for ejector optimisation can be developed.

References

- [1] Riffat S, Gan G, Smith S. Computational fluid dynamics applied to ejector heat pumps. *Appl Therm Eng* 1996;16(4):291–7.
- [2] Riffat S, Omer S. CFD modelling and experimental investigation of an ejector refrigeration system using methanol as the working fluid. *Int J Energy Res* 2001;25(2):115–28.
- [3] Eames IW, Ablwaifa AE, Petrenko V. Results of an experimental study of an advanced jet-pump refrigerator operating with R245fa. *Appl Therm Eng* 2007;27(17):2833–40.
- [4] Zhu Y, Cai W, Wen C, Li Y. Numerical investigation of geometry parameters for design of high performance ejectors. *Appl Therm Eng* 2009;29(5):898–905.
- [5] Ruangtrakoon N, Aphornratana S, Sriveerakul T. Experimental studies of a steam jet refrigeration cycle: effect of the primary nozzle geometries to system performance. *Exp Therm Fluid Sci* 2011;35(4):676–83.
- [6] Ruangtrakoon N, Thongtip T, Aphornratana S, Sriveerakul T. CFD simulation on the effect of primary nozzle geometries for a steam ejector in refrigeration cycle. *Int J Therm Sci* 2013;63:133–45.
- [7] Varga S, Oliveira AC, Diaconu B. Influence of geometrical factors on steam ejector performance—a numerical assessment. *Int J Refrig* 2009;32(7):1694–701.
- [8] Varga S, Oliveira AC, Diaconu B. Numerical assessment of steam ejector efficiencies using CFD. *Int J Refrig* 2009;32(6):1203–11.
- [9] Yadav RL, Patwardhan AW. Design aspects of ejectors: effects of suction chamber geometry. *Chem Eng Sci* 2008;63(15):3886–97.
- [10] Ji M, Utomo T, Woo J, Lee Y, Jeong H, Chung H. CFD investigation on the flow structure inside thermo vapor compressor. *Energy* 2010;35(6):2694–702.
- [11] Aidoun Z, Ouzzane M. The effect of operating conditions on the performance of a supersonic ejector for refrigeration. *Int J Refrig* 2004;27(8):974–84.
- [12] Wang X-D, Dong J-L. Numerical study on the performances of steam-jet vacuum pump at different operating conditions. *Vacuum* 2010;84(11):1341–6.
- [13] Pounds DA, Dong JM, Cheng P, Ma HB. Experimental investigation and theoretical analysis of an ejector refrigeration system. *Int J Therm Sci* 2013;67:200–9.
- [14] Sriveerakul T, Aphornratana S, Chunnanond K. Performance prediction of steam ejector using computational fluid dynamics: Part 2. Flow structure of a steam ejector influenced by operating pressures and geometries. *Int J Therm Sci* 2007;46(8):823–33.
- [15] Yang K, Lee H, Jung H. Numerical prediction of jet behavior of thermal vapor compressor. *Desalin Water Treat* 2011;33(1–3):248–54.
- [16] Yang X, Long X, Yao X. Numerical investigation on the mixing process in a steam ejector with different nozzle structures. *Int J Therm Sci* 2012;56:95–106.
- [17] Brown GL, Roshko A. On density effects and large structure in turbulent mixing layers. *J Fluid Mech* 1974;64(04):775–816.
- [18] Dimotakis PE. Two-dimensional shear-layer entrainment. *AIAA J* 1986;24(11):1791–6.
- [19] Bogdanoff D. Compressibility effects in turbulent shear layers. *AIAA J* 1983;21(6):926–7.
- [20] Papamoschou D, Roshko A. The compressible turbulent shear layer: an experimental study. *J Fluid Mech* 1988;197:453–77.
- [21] Dimotakis PE. Entrainment into a fully developed, two-dimensional shear layer. In: *AIAA, Aerospace Sciences Meeting*; 1984.
- [22] Slessor M, Zhuang M, Dimotakis P. Turbulent shear-layer mixing: growth-rate compressibility scaling. *J Fluid Mech* 2000;414:35–45.
- [23] Smits AJ, Dussauge J-P. *Turbulent shear layers in supersonic flow*. Springer Science & Business Media; 2006.
- [24] Samimy M, Elliott G. Effects of compressibility on the characteristics of free shear layers. *AIAA J* 1990;28(3):439–45.
- [25] Goebel SG, Dutton JC. Experimental study of compressible turbulent mixing layers. *AIAA J* 1991;29(4):538–46.
- [26] Chinzai N, Masuya G, Komuro T, Murakami A, Kudou K. Spreading of two-stream supersonic turbulent mixing layers. *Phys Fluids (1958–1988)* 1986;29(5):1345–7.
- [27] Barre S, Quine C, Dussauge J. Compressibility effects on the structure of supersonic mixing layers: experimental results. *J Fluid Mech* 1994;259:47–78.
- [28] Clemens N, Mungal M. Large-scale structure and entrainment in the supersonic mixing layer. *J Fluid Mech* 1995;284:171–216.
- [29] Slessor MD. *Aspects of turbulent-shear-layer dynamics and mixing*. 1998 [DTIC Document].
- [30] ANSYS-FLUENT 14.5 User's guide.
- [31] Al-Doori GFL. Investigation of refrigeration system steam ejector performance through experiments and computational simulations. University of Southern Queensland; 2013.
- [32] Chunnanond K, Aphornratana S. An experimental investigation of a steam ejector refrigerator: the analysis of the pressure profile along the ejector. *Appl Therm Eng* 2004;24(2):311–22.
- [33] Sriveerakul T, Aphornratana S, Chunnanond K. Performance prediction of steam ejector using computational fluid dynamics: Part 1. Validation of the CFD results. *Int J Therm Sci* 2007;46(8):812–22.

Chapter 6 Pitot and static pressure measurements in a co-flowing steam jet

Pitot and static pressure measurements in a co-flowing steam jet

Kavous Ariafar¹, Thomas Cochrane², Ray Malpress¹ and David Buttsworth¹

¹University of Southern Queensland, Australia

²Australian National University, Australia

Abstract:

Condensation in the primary nozzle of a steam ejector changes the steam jet properties during the nozzle expansion process and affects the mixing rate of the primary and secondary streams and thus the performance of steam ejectors. Only limited experimental data is available for the mixing of wet steam jets at conditions relevant to steam ejectors. The present work provides static and pitot pressure measurements within a wet supersonic steam jet which mixes with a low pressure co-flowing secondary stream. High pressure steam was delivered to the primary nozzle at a stagnation pressure and temperature of 270 kPa and 406 K, respectively. The primary nozzle throat diameter was 3.2 mm and its exit diameter was 13.6 mm. The low pressure secondary steam was delivered to the mixing chamber at stagnation conditions of 1 kPa and 323 K. Pitot and static pressure measurements were obtained on the mixing jet centreline from the nozzle tip until a downstream location of 185 mm in the mixing chamber. Radial profiles of pitot and static pressure were also measured at positions of 5, 20, 35, 85, 135 and 185 mm downstream of the nozzle exit. With the mixing chamber pressure maintained at 1.3 kPa, the mixing jet was in an under-expanded condition. CFD simulations with a non-equilibrium wet steam model also demonstrate the under-expanded jet structure. The pitot pressure profiles at the furthest locations downstream (135 and 185 mm) show reasonable agreement between experiments and simulations in terms of the spreading of the jet due to turbulent mixing. However, there are significant differences between the experimental and simulated pitot and static pressures profiles in the transverse and axial directions. Some of these differences arise because of incorrect simulation of flow structures in the near field of the jet. Contributions to these differences are also

likely to arise because the simulated static pressures in the under-expanded wet steam jet core are lower than the triple point for water (0.61 kPa), so potential exists for liquid-solid and vapour-solid phase transitions that are not currently modelled in the simulations.

1. Introduction

There are many devices in which two almost-parallel streams get mixed and the performance of these devices depends in part, on the mixing rate of the streams. A supersonic steam ejector is one such device. Ejectors are a type of compressor used to increase the pressure of a low pressure stream. A steam ejector consists of a primary nozzle which expands high pressure steam (known as the primary stream) to create a very low pressure region in the vicinity of the nozzle exit and entrain low pressure steam (the secondary stream). The induced low pressure fluid from the secondary stream then mixes with the primary high speed jet which leaves the nozzle. It is possible to achieve a higher pressure than is present in the secondary stream by decelerating the mixture in a diffuser.

An important parameter that describes the performance of steam ejectors is the entrainment ratio (ER) which is defined as the ratio of mass flow rate of the entrained secondary stream to that of the high pressure primary stream. In general, having an ejector system with a high entrainment ratio is an advantage for industrial applications, as the higher the entrainment ratio, the larger the quantity of low pressure steam that can be recovered. The critical back pressure is another important parameter for the ejector performance which determines the pressure to which the secondary stream can be increased without any decrease in the ER.

There are many factors which influence the ejector performance and in particular the ejector entrainment ratio. The mixing process between the primary and secondary streams, which begins immediately downstream of the primary nozzle exit with the formation of a mixing layer, is one of these factors. Ariaifar et al. [1] performed an ideal gas computational simulation to investigate the contribution of mixing to the ejector entrainment ratio under different operating conditions. For a

particular ejector and operating conditions, they found that about 35% of the ejector entrainment ratio is attributable to mixing effects. In another work, Ariafar et al. [2] carried out a computational study to explore why wet steam ejector simulations yield a higher ejector performance compared to the ideal gas simulations. Their results showed that enhanced mixing layer growth which arises due to steam condensation in the primary nozzle is the likely cause of higher entrainment ratio of the ejector simulations using the wet steam model. Therefore, accurate simulation of the mixing process within ejectors is required in order to maximize the performance of steam ejectors which leads to improvements in energy efficiency.

However, the best choice for modelling axisymmetric compressible turbulent mixing within ejectors is not clear. For example, Hemidi et al. [3] advocate the $k - \varepsilon$ turbulence model, while Bartosiewicz et al. [4] and Ruangtrakoon et al. [5] have determined that the best choice in their application is the $k - \omega SST$ turbulence model. Cutler et al. [6] and Clifton and Cutler [7] conducted an experimental work on constant pressure high speed axisymmetric jet mixing to provide data for validation of computational simulation tools. Their results indicated the need for improvement of computational simulation capabilities, particularly for jet regions at the locations where the ratio of downstream distance from the nozzle exit and the nozzle exit diameter were higher than 4 ($x / D > 4$).

Jet mixing in ejectors normally occurs within a geometry that is nominally axisymmetric, but with flow conditions that are turbulent and highly compressible with strong pressure gradients. The case of steam ejector mixing is even more complicated because of condensation effects but limited data exists: measurements of wall static pressures and performance maps for various configurations are available in the literature, but these do not provide direct measurements of mixing. In order to investigate steam jet mixing at conditions related to steam ejector operation, Al-Doori and Buttsworth [8] provided several experimental pitot pressure surveys for the mixing region. For this experimental work, there was no secondary stream. The free shear layer growth rate they calculated from the pitot pressure measurements was consistent with results from mixing layer correlations. However, in the

Al-Doori and Buttsworth [8] configuration, the primary nozzle and the diffuser were nominally axisymmetric, but the mixing chamber had a rectangular cross section. Computational simulation of their wet-steam mixing results therefore requires a fully three dimensional approach, which is computationally expensive.

To provide data on supersonic steam jet mixing with conditions similar to those in steam ejectors with a nominally axisymmetric geometry, an experimental investigation was carried out with a high pressure steam jet which expands through a converging-diverging nozzle and mixes with low pressure co-flowing steam. The pitot and static pressures of the mixing jet were measured by a probing system in the mixing chamber to provide data on the mixing process of the streams and also the steam jet structure. To demonstrate the suitability of the data for validation of computational simulations of wet steam jet mixing, some initial simulations using the $k - \omega SST$ turbulence model are also presented. Such an axisymmetric arrangement lends itself to computational simulation using axisymmetric modeling which is computational cost effective.

2. Experimental set up

Figure 1 illustrates the arrangement of the experimental apparatus which consists of four main components: the steam generator, the evaporator, the mixing chamber, and the condenser.

2.1 Steam generator

The steam generator was used to supply the required high pressure steam as the primary stream for the experiment. The electric Simons boiler was used to provide steam with a mass flow rate of 3.3 ± 0.04 g/s and stagnation pressure of 270 ± 2 kPa to feed to the mixing chamber. The steam mass flow rate was measured through a Coriolis mass flow meter (Yokogawa, specify model number RCCF31) installed between the steam generator and the test section. A calibrated electronic pressure transducer (Wika, type A-10) was used to measure the steam static pressure delivered to the primary nozzle. A dial gauge pressure was also used to monitor the pressure during the experiment.

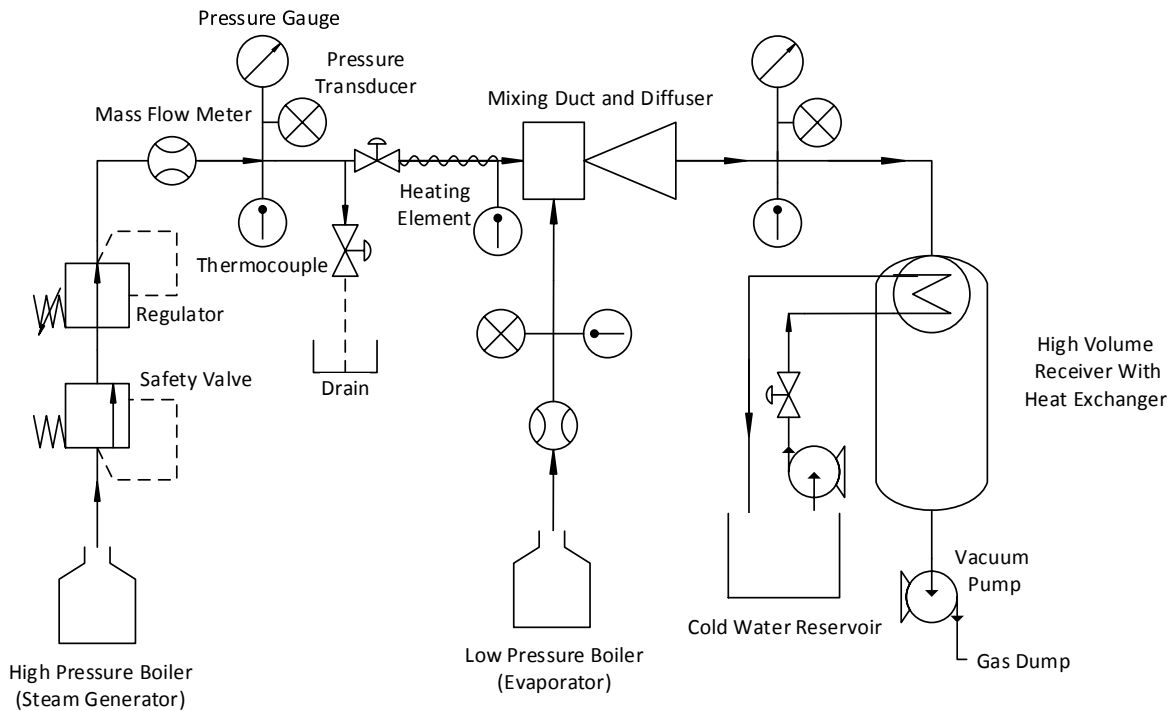


Figure 1. Arrangement of the experimental apparatus

An electrical heating element was wrapped around the pipe connection between the mass flow meter and the primary nozzle to ensure that superheat steam was delivered to the test section. The heating element was rated at 300 W and increased the steam temperature delivered to the primary nozzle by approximately 4°C. The steam stagnation temperature was 133 ± 1 °C during the experiment and this value was measured using a K-type thermocouple located within the primary line, approximately 400 mm upstream of the primary nozzle.

2.2 Evaporator

The evaporator used in this experiment was designed by Al-Doori [9] to simulate a 3500 W cooling load and was insulated using Armaflex insulation to reduce the external heat gain and included an electric heater element with a rating of 3600 W at its base. A single phase half controlled rectifier was used to control the load of the evaporator together with a Watt meter to measure the electrical power.

The steam stagnation pressure and temperature which was delivered from the evaporator to the test section as the secondary stream were measured by using a calibrated electronic pressure transducer (Wika, type A-10) and a K-type thermocouple, respectively. The mass flow rate was measured with a Coriolis mass flow meter (Siemens, model number FCT030). The operating conditions for the secondary stream were at 1 ± 0.1 kPa, 50 ± 1.5 °C and 1.4 ± 0.07 g/s for the stagnation pressure, stagnation temperature and mass flow rate, respectively. All signals from the pressure transducers, thermocouples and mass flow meters were recorded on a National Instruments Compact Data Acquisition (cDAQ) system.

2.3 Condenser

Steam discharged from the test section was delivered through a diffuser into the condenser. The diffuser was not choked, so the test section pressure was maintained constant by adjusting the condensed steam temperature. The condenser consisted of two concentric pipes approximately 6 meters long. The inner pipe was a 6" diameter brass pipe which contained the discharged steam and the outer pipe was PVC. Cold water was circulated through the annulus between these two concentric pipes in order to condense the discharged steam. The target was to maintain the condenser pressure at 1.5 ± 0.1 kPa. A vacuum pump was connected to the downstream end of the condenser to provide additional capacity, particularly for removal of small quantities of purging air introduced during the experiment.

2.4 Co-flowing steam jet

2.4.1 Primary nozzle

Figure 2 illustrates a schematic of the co-flowing steam jet apparatus. It consists of a primary nozzle, secondary inlet, diffuser, test section, measurement probes and traversing mechanism for the probes. The primary nozzle and the secondary inlet parts were designed by Al-Doori [9]. The nozzle exit

position was adjusted to be 15 mm downstream from the edge of the nozzle end plate. The main dimensions of the primary nozzle and the secondary inlet are presented in Table 1.

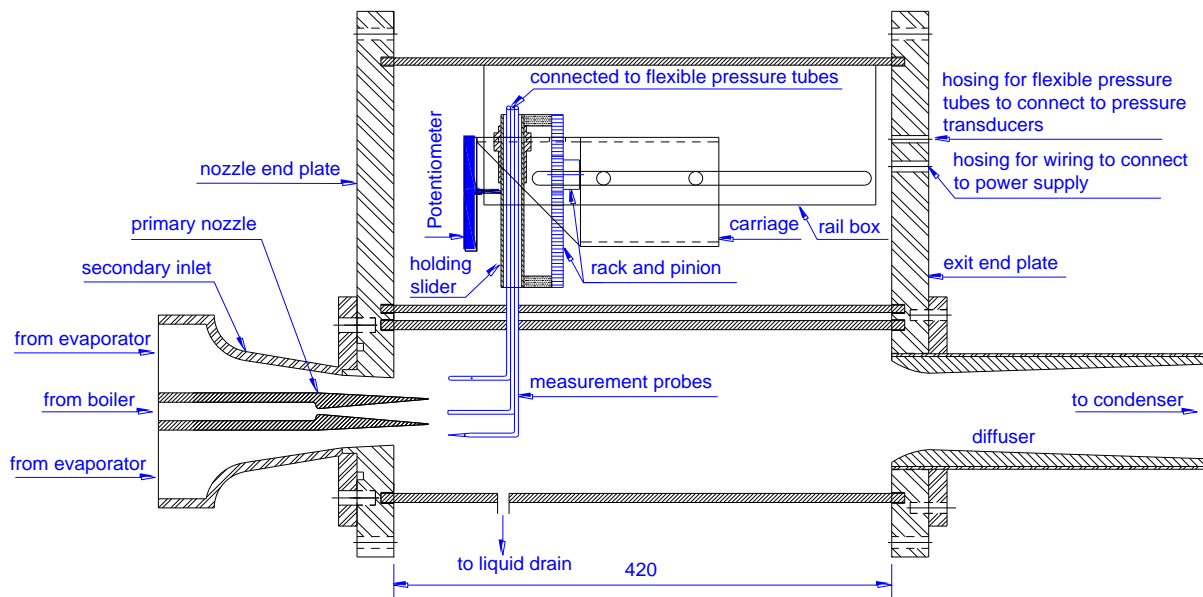


Figure 2. Arrangement of the co-flowing steam jet, dimensions in mm

2.4.2 Test section

The test section included two transparent Acrylic tubes with the length of 420 mm. The lower tube with the wall thickness of 5 mm, has an inner diameter of 90 mm. It was used as the mixing chamber for the primary stream delivered through the primary nozzle and the secondary stream delivered through the secondary inlet. The upper tube housed the moving mechanism for the measurement probes, flexible pressure tubes and wiring connections. It has an inner diameter of 132 mm with a wall thickness of 4 mm. These Acrylic tubes were connected to each other through a 5 mm thick aluminium plate with a 3 mm wide slot along its length to enable the movement of the measuring probes along the length of the test section. The arrangement of the aluminium plate that connected the two Acrylic tubes is shown in Figure 3.

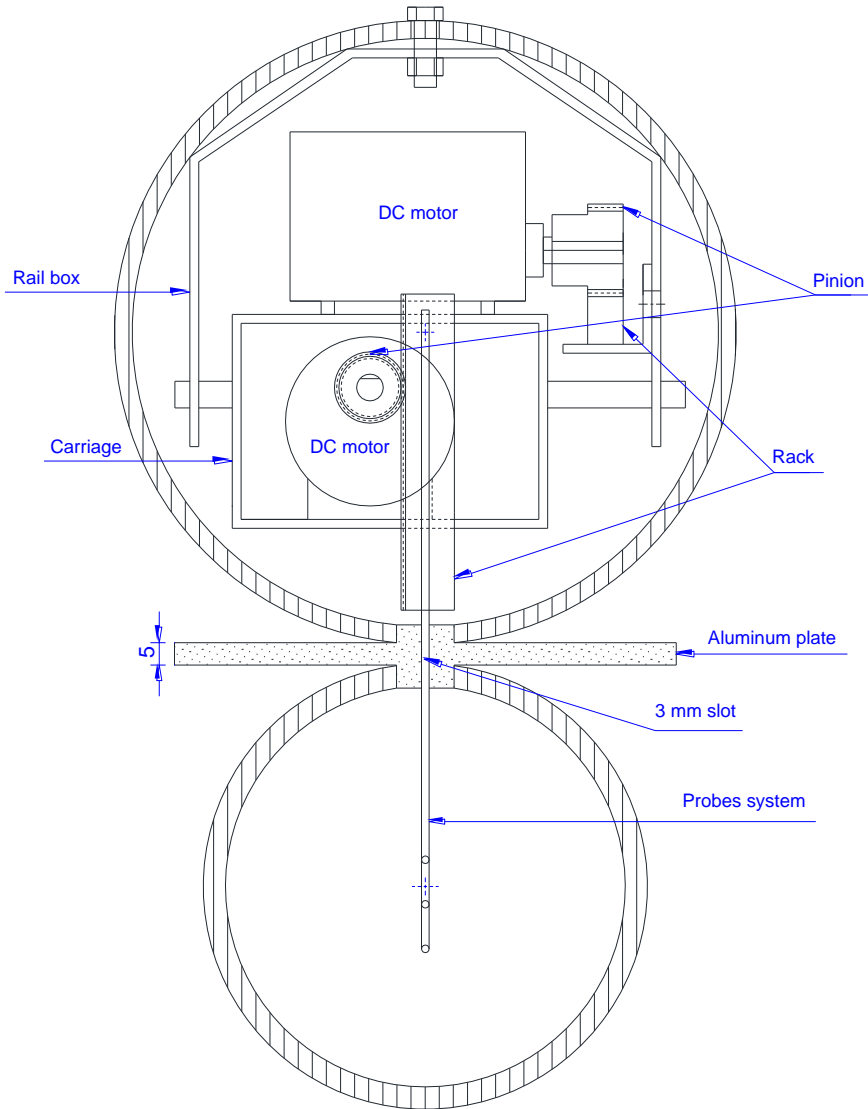


Figure 3. Section view of the test section including measurement probes and arrangement of the moving mechanism, dimensions in mm

2.4.3 Diffuser

The diffuser was designed to deliver the steam to the condenser and also to recover some of the total pressure in the test section. It allows the condenser to operate at a slightly higher pressure than in the test section. Key dimensions of the diffuser are summarized in Table 1. Pressure at the exit of the diffuser was measured using a calibrated pressure transducer (Wika, type A-10) and was also monitored by a pressure gauge during the experiment. A K-type thermocouple was also used to record the steam discharge temperature.

Table 1. Geometric details of the co-flowing steam jet apparatus

Geometric parameters	Size (mm)
Primary nozzle inlet diameter	10
Primary nozzle throat diameter	3.2
Primary nozzle outlet diameter	13.6
Primary nozzle divergent length	59.5
Inlet diameter of the secondary inlet	106
Outlet diameter of the secondary inlet	37
Diffuser inlet diameter	80
Diffuser throat diameter	44.5
Diffuser outlet diameter	80
Diffuser divergent length	270
Mixing chamber length	420
Mixing chamber diameter	90

2.4.4 Measurement probes and traversing mechanism

Figure 4 shows the arrangement of the measurement probes which were designed to measure the static and pitot pressures of steam in the test section. The probes were made of brass tube with 1.6 mm OD and 1 mm ID. The upper probe with a closed hemispherical nose was used to measure the static pressure within the subsonic portion of the mixing jet. The hemispherical shape for the nose is used so that the flow is disturbed only at the nose section. Four holes (pressure taps) of 0.25 mm diameter were drilled at a location 10 mm downstream of the nose at 90° intervals around the circumference. The pressure taps were located around the circumference at several diameters downstream of the nose so that the measurement is not influenced by the disturbed flow in the vicinity of the nose. The size of pressure taps must be small and free from imperfections such as burrs, in order not to disturb the flow locally. But the size of the holes must not be too small, since very small hole may lead to longer response time. The size, position and number of the holes were selected based on recommendations in Refs. [10-12].

The middle probe with an open and flat face end was the pitot probe while the lower probe with a conical nose was designed to measure the static pressure for the supersonic portion of the steam jet. The design of the supersonic static probes differs from the subsonic static pressure probes in that a conical shock waves forms at the tip of the probe. In order to keep the strength of the conical shock

wave low, the conical nose was chosen to be as sharp as practical: a 5 degree half-angle for the conical tip was chosen in this case. Another reason for selecting a sharp nose is to ensure the conical shock wave detachment Mach number is low [11, 13]. In this arrangement, the holes are located on the cone surface and the pressure on the cone surface can be related to the undisturbed flow static pressure by the conical shock theory if the Mach number and ratio of specific heats are known. Static pressure measurements with the supersonic static probe will be very sensitive to inclination of the tube relative to the flow direction. Inclinations beyond 5° (half angle of the nose) result in a large error in the measured static pressure. In order to minimize this error, it is a common practice to have static probes with four holes in mutually perpendicular directions [14].

These three probes were assembled and welded together to form a system for pressure measurement of the steam jet in the mixing chamber. The three brass tubes were connected to three calibrated pressure transducers (Wika, type A-10) through three flexible pressure tubes.

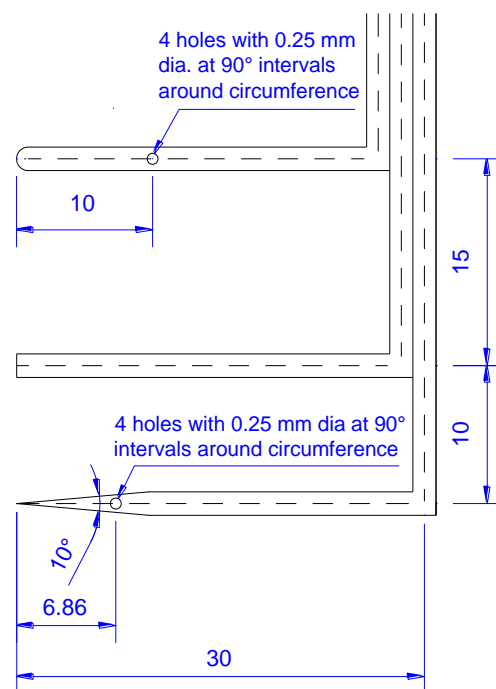


Figure 4. Measurement probes, dimensions in mm

A pair of DC motors, racks and pinions were used to traverse the probes in the vertical and horizontal directions. A cross sectional view of the test section, which illustrates the measurement probes and

shows the traversing mechanism is presented in Figure 3. Steam jet pressures were measured at 6 positions downstream from the primary nozzle exit plane: 5, 20, 35, 85, 135 and 185 mm. A potentiometer was used to indicate the probe positions during a full vertical traverse relative to the centreline of the primary nozzle. Steam jet pressures were also measured along the centreline from the nozzle tip until the 185 mm downstream position. Experimental data was recorded when the operating pressures of the apparatus reached a steady state condition.

In a full vertical traverse, the probes moved vertically through a distance of 27 mm, and this movement typically took around 16 minutes. The probes were traversed downwards at each location downstream of the nozzle exit, and the pitot probe started from a location 25 mm above the jet centreline and finished at a location 2 mm below the jet centreline. Vertical positions of the probes during any given traverse were determined from a linear potentiometer and the measured upper and lower position limits. Two limit switches were used to stop the traverse mechanism when it reached the upper and lower position limits. The uncertainty in positioning for the probe traversing mechanism using this method was around ± 0.5 mm.

To ensure that liquid droplets generated due to steam condensation did not block the probes and the flexible pressure tubes, atmospheric air purging was regularly applied through solenoid valves on a tee branch of each of the flexible pressure tubes close to the pressure transducers. When actuated, the solenoid valves allowed a small amount of atmospheric air into the pressure measurement line, and this air was vented into the test section through the measuring orifices of the three probes. The decay time for the increased pressure due to purge was around 8 seconds for the pitot probe – this was the time from the pressure increase in the line at the time of solenoid actuation to the time for the pressure to fall back to the local pressure being measured at the probe. The corresponding time for the supersonic and subsonic static probes was around 14 seconds. A stepping timer was connected to the DC motor which was used for the vertical movement so that the probes traversed around 1 mm in less than 1 second in vertical direction and then stopped for 20 seconds at every step during a full

traverse. Air was purged alternatively to the probes during a full traverse; every second step purged the pitot probe and every alternate step purged the static probes.

For probe measurements during the traverse along the jet centreline, no limit switch or potentiometer was used. A full traverse, which took around 45 minutes, started from a downstream position of 185 mm from the nozzle exit plane towards the nozzle tip (corresponding to a position of 0 mm). In this case, probe position was determined from a sighting technique referenced to custom ruler markings adhered to the outer surface of the mixing chamber. The uncertainty for this positioning method is estimated to be less than ± 3 mm. By using the stepping timer connected to the DC motor for the horizontal movement, the probes traversed around 2 mm in less than 1 second for each step and were then stopped for 30 seconds. Air was purged through the probe on every step as it traversed along the centreline.

3. Computational simulation

The primary motivation for the present work was to provide experimental data on mixing in a steam jet configuration suitable for validation of modelling efforts. This is an important contribution because other experiments relating to steam ejectors have not provided direct data on the jet mixing process. Phenomena such as steam condensation and shock and expansion waves can affect the mixing process and unless accurate modelling of the mixing is achieved, reliable and robust design optimisation may be difficult. In this section, a CFD technique is applied to aid the interpretation of the flow structure and mixing process within the steam jet, and to identify scope for future improvements in CFD simulation efforts.

3.1 Computational model

3.1.1 Governing equations

The laws of conservation of mass, momentum and energy which have been solved in this work through computational simulation are:

$$\frac{\partial \rho}{\partial t} + \frac{\partial}{\partial x_i} (\rho U_i) = 0 \quad (1)$$

$$\frac{\partial}{\partial t} (\rho U_i) + \frac{\partial}{\partial x_j} (\rho U_i U_j) = -\frac{\partial P}{\partial x_i} + \frac{\partial \tau_{ij}}{\partial x_j} \quad (2)$$

$$\frac{\partial}{\partial t} (\rho E) + \frac{\partial}{\partial x_i} (U_i (\rho E + P)) = \vec{\nabla} \cdot (\alpha_{eff} \frac{\partial T}{\partial x_i} + U_j (\tau_{ij})) \quad (3)$$

with

$$\tau_{ij} = \mu_{eff} \left(\frac{\partial U_i}{\partial x_j} + \frac{\partial U_j}{\partial x_i} \right) - \frac{2}{3} \mu_{eff} \frac{\partial U_k}{\partial x_k} \delta_{ij} \quad (4)$$

In the case of two-phase wet steam, ρ is the mixture density, U is velocity and $E = e + \frac{U \cdot U}{2}$ is the total specific energy of the mixture, where e is the specific internal energy and $\frac{1}{2} U \cdot U$ is the specific kinetic energy.

3.1.2. Turbulence model

In order to investigate the mixing process and simulate the co-flowing steam jet configuration, a two equation turbulence model was applied to the whole flow domain based on the $k - \omega$ SST (Shear Stress Transport). A benefit of this model which was proposed by Menter [15], is the capacity to simulate free shear flow spreading rates which generally agrees with measurements for far wakes, mixing layers, round and radial jets and is applicable to both wall-bounded flows and free flows [16]. It was also shown in the literature that this model can well predict the flow physics inside the ejectors

with a good agreement with experimental results [4, 5, 17]. The main governing equations for this model are described by Refs. [15, 18]:

$$\frac{\partial(\rho k)}{\partial t} + \frac{\partial}{\partial x_i}(\rho k U_i) = \frac{\partial}{\partial x_j} \left[\left(\mu + \frac{\mu_t}{\sigma_k} \right) \frac{\partial k}{\partial x_j} \right] + G_k - Y_k + S_k \quad (5)$$

$$\frac{\partial(\rho \omega)}{\partial t} + \frac{\partial}{\partial x_i}(\rho \omega U_i) = \frac{\partial}{\partial x_j} \left[\left(\mu + \frac{\mu_t}{\sigma_\omega} \right) \frac{\partial \omega}{\partial x_j} \right] + G_\omega - Y_\omega + D_\omega + S_\omega \quad (6)$$

In the above equations, k and ω are the turbulent kinetic energy and the specific dissipation rate, respectively. Definitions of the terms G , Y , S and D can be found in Ref. [16].

3.1.3 Wet steam model

The steam behavior is governed by the Eulerian-Eulerian approach and the two phase flow is modeled using the compressible Navier-Stokes conservation equations together with two additional transport governing equations. These equations are available in the wet steam model in FLUENT for the liquid phase mass fraction (β) and the number of liquid droplets per unit volume (η).

The first additional transport equation governing the mass fraction of the condensed liquid phase is written as [19]:

$$\frac{\partial(\beta \rho)}{\partial t} + \nabla \cdot (\rho \beta \vec{U}) = \Gamma \quad (7)$$

where Γ is the mass generation rate due to condensation and evaporation, which is correlated with the nucleation rate I (number of new droplets per unit volume per second) and the growth or demise of these droplets.

The second additional transport equation estimates the growth of droplet numbers per unit volume of steam and is:

$$\frac{\partial(\rho\eta)}{\partial t} + \nabla \cdot (\rho\eta\vec{U}) = \rho I \quad (8)$$

The homogeneous nucleation theory explains the creation of a liquid phase in the form of droplets from a superheated phase in the absence of foreign particles. The estimation of the size of created droplets during the nucleation in wet steam flow is very difficult. The classical theory of nucleation is used to calculate the number of liquid droplets. More information about the wet steam theory and the equations used in this present approach can be found from Ref. [20]. To reduce the complexity of the two phase flow model, assumptions of no slip between the phases, and negligible volume of the condensed liquid are used since droplet sizes are typically very small and negligible interaction between the droplets is expected.

3.1.4 Numerical solution procedure

The governing equations were solved numerically using a commercial CFD code, FLUENT 14.5 which is based on the control volume method that approximates the governing equations as algebraic equations. A second order upwind scheme was selected to achieve a high order of accuracy at cell faces through a Taylor series expansion of the cell centered solution. The nonlinear governing equations were solved using the coupled implicit solver and the standard wall function was applied near the walls. Convergence of the solution was assumed when two criteria were satisfied:

- the relative difference of mass flow rate between the inlet and outlet boundaries of less than 10^{-7} ; and
- every type of calculated residual error was less than 10^{-6}

3.2 Geometry and boundary conditions

The geometry of the co-flowing steam jet was produced based on the main dimensions summarized in Table 1. The computations were performed using a 2-D axisymmetric solver in order to reduce the

CPU cost and simulation time. Figure 5 shows the computational element configuration with a close up view of the mesh elements near the nozzle exit and start of the mixing chamber.

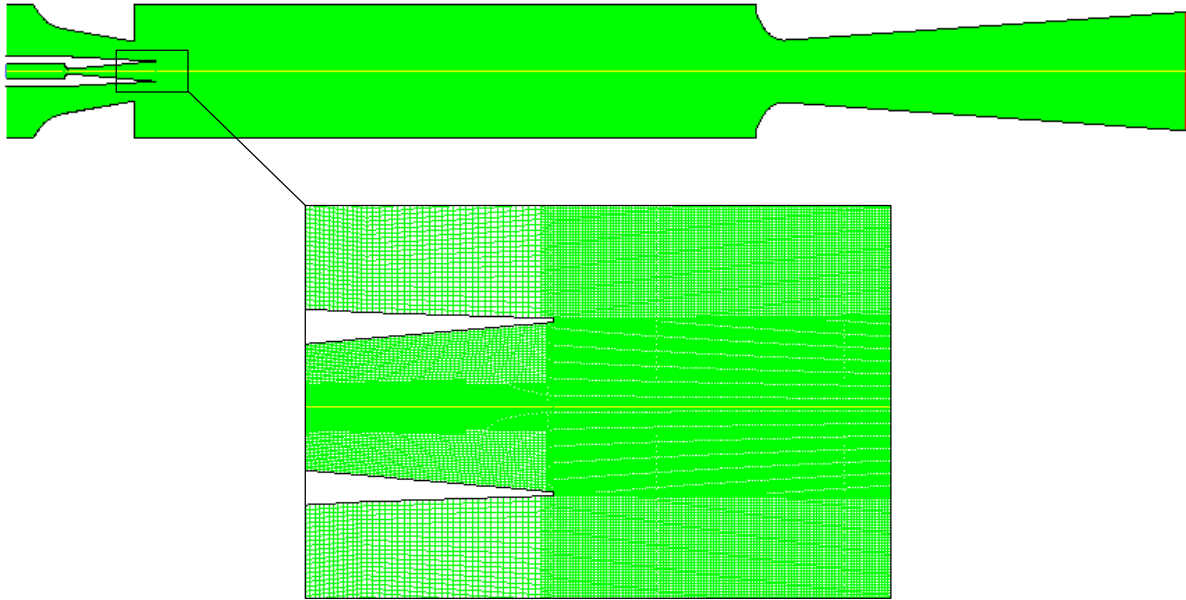


Figure 5. Computational grid used for co-flowing steam jet simulations in the case of the medium mesh density

The computational grid was generated based on structured quadrilateral elements. Mesh adaption was performed in the mixing chamber from the nozzle exit plane until the last particular downstream location, where the experimental data was measured. In order to check the sensitivity of the results to the mesh density, three different mesh sizes with different resolution in each millimetre were generated: the coarse mesh density with 46440 elements, the medium with 172900 and the fine mesh with 237100 elements. The results showed essentially the same profile for the static pressure along the centreline for the medium and fine mesh densities: maximum differences of less than 4% were obtained for these two cases. Therefore, the medium mesh was selected for further computations with consideration of the computational costs while still providing sufficient cells in the mixing chamber. The medium mesh provided a minimum of 4 cells per millimeter in the radial direction.

The inlet boundaries were pressure inlet and mass flow inlet for the primary and secondary streams, respectively. A pressure outlet boundary condition was also selected for the discharge stream leaving

the diffuser. The parameter values for the experimental operating conditions which were applied to the boundary conditions in computational simulation are given in Table 2.

Table 2. Steam flow parameters applied to the co-flowing steam jet boundaries. For the primary and secondary streams, the given values are stagnation and it is static value for the discharge stream

Stream	Pressure (kPa)	Temperature (K)	Mass flow rate (g/s)
Primary	270 ± 2	406 ± 1	3.3 ± 0.04
Secondary	1 ± 0.1	323 ± 1.5	1.4 ± 0.07
Discharge	1.5 ± 0.1	-----	-----

3.3 Pitot pressure calculation from CFD results

To calculate the pitot pressure from the CFD simulation, standard expressions for pitot pressure in subsonic and supersonic flows are used. In the case of a subsonic flow, the pitot pressure is equal to the flow total pressure [21]:

$$\frac{P_{pitot}}{P} = \frac{P_0}{P} = \left[1 + \frac{\gamma-1}{2} M^2 \right]^{\frac{\gamma}{\gamma-1}} \quad (9)$$

However, in supersonic flow, some total pressure is lost through the shock compression process and the pitot pressure is calculated by the Rayleigh equation [22]:

$$\frac{P_{pitot}}{P} = \left[\frac{\gamma+1}{2} M^2 \right]^{\frac{\gamma}{\gamma-1}} \left[\frac{\gamma+1}{2\gamma M^2 - \gamma + 1} \right]^{\frac{1}{\gamma-1}} \quad (10)$$

There is a departure from ideal gas behaviour for wet steam because of the occurrence of steam condensation in the mixture and in this case, equilibrium values of γ and Mach number are used for calculation of the pitot pressure. The equilibrium value of γ which is denoted as γ_e is 1.12 for low pressure steam and the equilibrium Mach number (M_e) is calculated using the equation presented in Ref. [23].

$$M_e = \frac{U}{\sqrt{\gamma_e (1-\beta) RT_s}} \quad (10)$$

In this equation, β is the liquid mass fraction in the mixture and T_s is the saturation temperature. These set of equations, however, are based on constant ratio of specific heats gas dynamic results and do use the ideal gas equation.

Pitot and cone-static pressure are also calculated using the thermodynamic properties of the steam from the CFD results based on the equilibrium and frozen-composition assumptions using CoolProp thermodynamic data. For the frozen-composition calculations of pitot and cone-static pressure, the liquid fraction in the flow is held constant at the pre-shock value specified by the CFD simulation so there is no change in steam composition when it passes through the shock wave and that the thermodynamic properties of steam (as reflected in the ratio of specific heats) remains fixed at its pre-shock value. However, with the equilibrium calculation of pitot and cone-static pressure, the liquid fraction in the flow is assumed to instantaneously adjust to the state dictated by the equilibrium thermodynamic properties of the wet steam and the gas dynamics associated with the normal and conical shock waves and the isentropic flow processes downstream of these shocks.

3.4 Probe blockage effect

In order to investigate the blockage effect of the probes on the flow structure downstream of the primary nozzle exit, a 2-D simulation using axisymmetric solver was performed for the probes located at 50 mm downstream of the primary nozzle exit plane along the centreline. Figure 6 shows the computational element configuration for this simulation. To simulate the blockage effect of the probes using the axisymmetric solver, the frontal area of the probes seen by the flow was divided into 8 different blunt parts and distributed in the radial direction in the mixing chamber to give a net blockage effect consistent with the physical configuration. The blockage diameter on the centreline was 1.6 mm reflecting the diameter of the probes in reality.

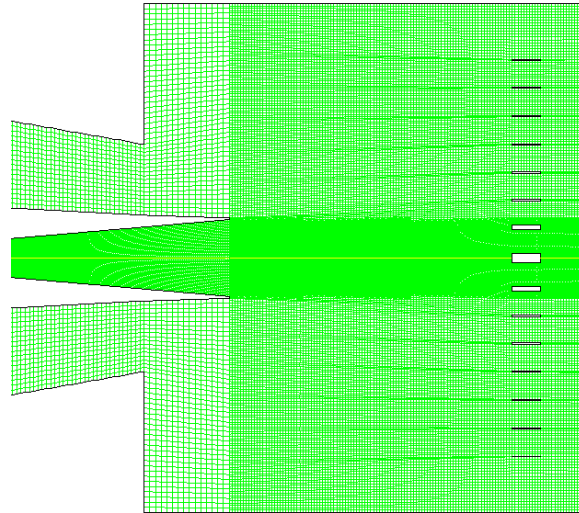


Figure 6. Grid elements for probes blockage effect

Figure 7 compares the static pressure profiles along the centreline from the nozzle exit plane up to the simulated probe location for cases with, and without the probe blockage effect. Figure 7 demonstrates that apart from the region immediately ahead of the probes in which the flow is decelerated by the probes, the flow on the centreline of the jet remains largely unaffected by the probe blockage.

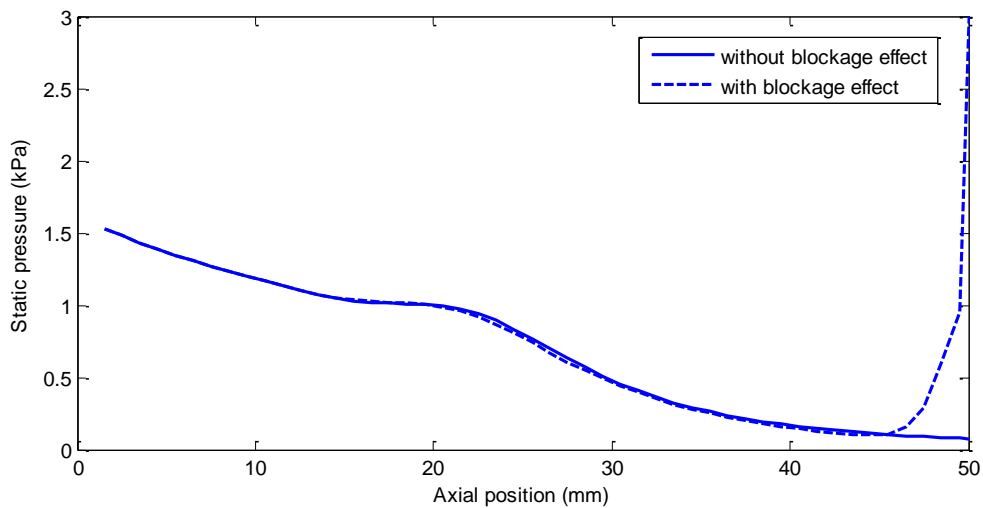


Figure 7. Comparison of the simulated static pressure profiles on the centerline for steam jet flow with, and without a probe blockage effect

4. Results and discussion

4.1 Static pressure profile along the centerline

Figure 8 presents the static pressure profile measured with the supersonic static probe (the cone-static pressure probe) along the jet centerline, together with the comparison to the results from the CFD simulations. The measurement was performed between the nozzle tip and a position of 185 mm downstream of the nozzle. The CFD simulation of static pressure which was achieved using a non-equilibrium wet steam model is labelled in Figure 8 as 'free stream static pressure'.

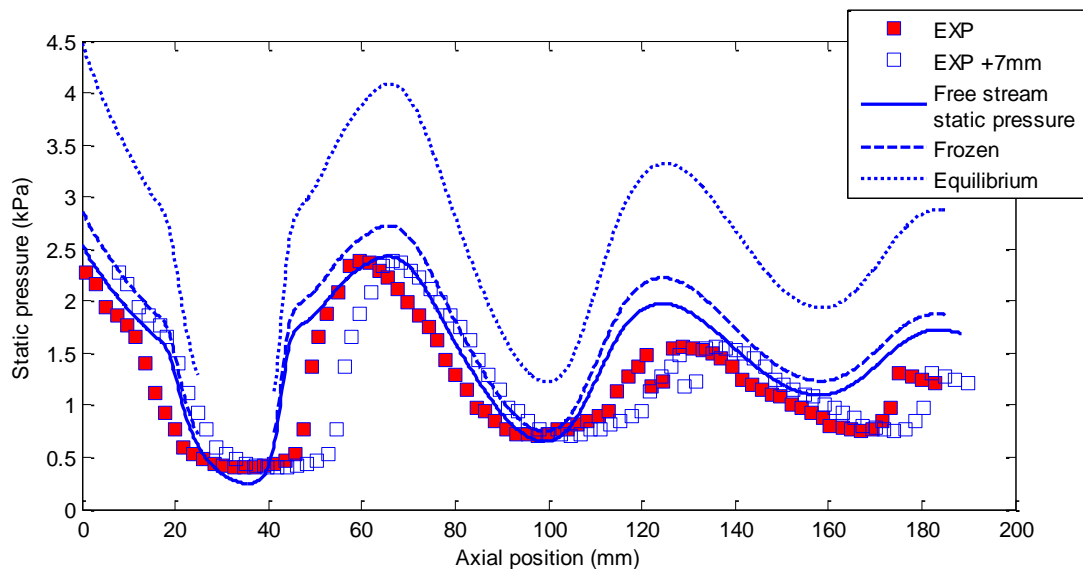


Figure 8. Static pressure profile along the jet centreline

The experimental static pressure data is presented in Figure 8 at two axial locations: the first which is represented by the solid symbol indicates the location of the tip of the cone probe; the second which is represented by the open symbol indicates the location of the static pressure orifices on the cone probe which are 7 mm downstream of the tip of the cone. The static pressure profile along the initial portion of the centerline is determined largely by inviscid shock and expansion wave processes. To help with the explanation of flow structure on the centerline, contour lines of the static pressure ranging from 0.247 to 3 kPa from the CFD simulation are illustrated in Figure 9. The centerline and

particular downstream locations at which the experimental data was measured are specified in this figure.

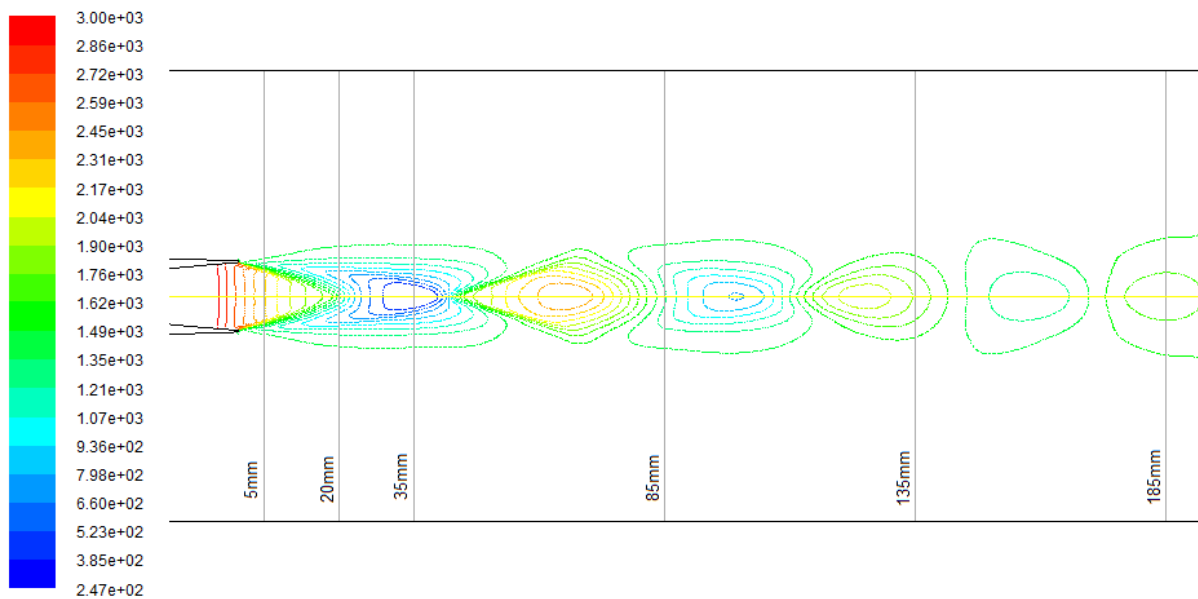


Figure 9. Contour lines of the static pressure (with the unit of kPa) in the mixing chamber from the CFD simulations

As the high pressure steam passes through the primary nozzle throat, it expands and accelerates in the conically-divergent part of the nozzle. The conical flow expansion process of the primary jet at the end of the primary nozzle continues for some distance, and if the local static pressure in the mixing chamber is lower than that for the expanded steam, the value of the static pressure decreases with further expansion. This process for the steam jet continues with a series of oblique shock and expansion waves so that its static pressure rises and its flow direction is adjusted for compatibility with the local static pressure and flow direction of the secondary stream in the mixing chamber. The strength of these shock and expansion waves decreases with increasing distance downstream.

As it is observed in Figure 8, the measured steam jet static pressure at the nozzle tip is around 2.3 kPa and this pressure steadily decreases until it reaches about 1.5 kPa at a distance of about 15 mm downstream of the nozzle tip. At this point, expansion waves arising from the under-expanded nature of the jet first reach the centerline and cause a more rapid static pressure decrease until it reaches a minimum value of around 0.45 kPa at an axial location of 35 mm from the nozzle exit plane. The non-

equilibrium computational simulations presented in Figure 8 and Figure 9 also simulate this low pressure region on the centerline, but the shape and magnitude of the minimum pressure region is significantly different in simulations: a sharper dip that reaches a lower pressure of about 0.25 kPa is simulated. Because the triple point of water occurs at a pressure of 0.61 kPa, there will be a tendency for liquid-to-solid and vapour-to-solid transitions that have not been included in the computational simulations. The energy exchanges associated with these transitions will tend to increase the pressure in the vapour and this is a likely contributor to the differences observed between the measurements and the computational simulations.

After the minimum pressure is reached at about 35 mm downstream of the nozzle exit, the centerline static pressure fluctuates due to the shock and expansion wave structures with three peaks and two troughs observable in the data and the simulations up to the location of 185 mm, as can be seen in Figure 8 and Figure 9. The data and simulations both demonstrate that the strength of these fluctuations is reduced with downstream distance, but there remain significant discrepancies between the measured and simulated results. For example, the simulated magnitude of the two peaks in static pressure at around 130 and 180 mm exceeds that of the experimental measurements by about 25%. In these downstream regions, the static pressure remains higher than the triple point value: the dip below 0.61 kPa only occurs in the first trough. However, the incorrect thermodynamics in the simulation of this first region will affect the flow downstream.

The frozen-composition calculation for the cone-static pressure obviously gives values for pressure that are higher than the static pressure obtained directly from the CFD simulations because of the conical shock compression effect, but the results from frozen-composition calculation do not offer improved agreement with the experimental data. The equilibrium calculation for the cone static pressure is in error by a significant margin. It is likely that the flow speed during transit through the conical shock and over the cone probe remains high such that there are insufficient collisions between the vapour phase molecules and the water droplets for there to be any significant change in

composition so the flow does not approach equilibrium composition for the cone probe. The discontinuity in the cone static pressure profiles for the equilibrium and frozen-composition calculations in the vicinity of 35 mm downstream position arises because these calculations were not able to be performed at static pressures below the triple point because of the lack of thermodynamic data in this region.

4.2 Pitot pressure profile along the centerline

Figure 10 shows the pitot pressure profile obtained from the pitot probe from the centerline from the nozzle tip until the 185 mm downstream position. The figure also includes the pitot profile from the non-equilibrium CFD simulation results which is labelled on Figure 10 as 'ideal gas, $\gamma = 1.12$ ' and calculated by using the method presented in section 3.3. Equilibrium and frozen composition calculations for the pitot pressure are also included in Figure 10. It is clear that the pitot pressure profile along the steam jet centerline has similar trends to the static pressure profile with troughs and peaks due to the expansion waves and shocks associated with the under-expanded characteristics of the jet.

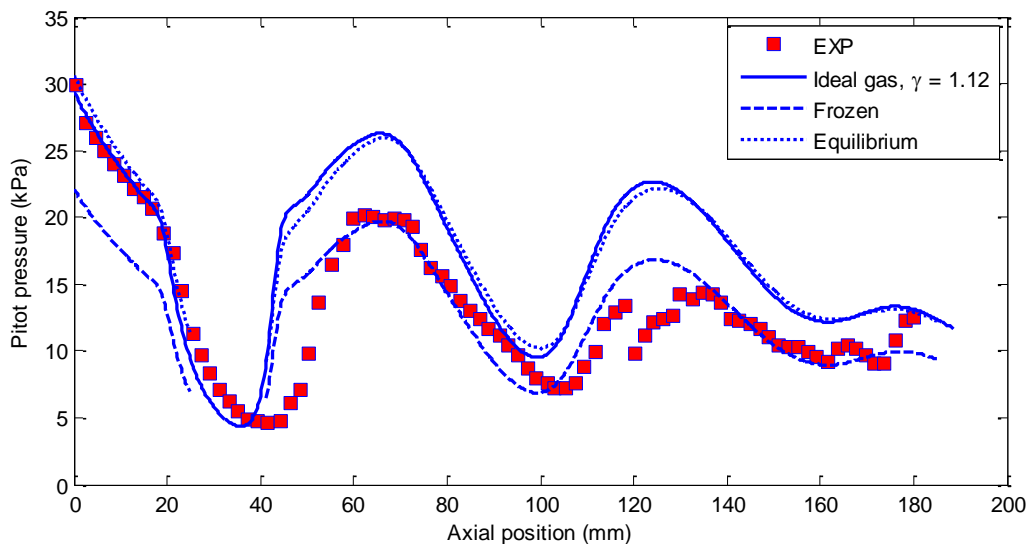


Figure 10. Pitot pressure profile along the jet centreline

The pitot pressure for the steam jet at the nozzle exit is about 30 kPa from the measurements, but it is reduced to a value of around 12 kPa at 185 mm downstream. The relative reduction of pitot pressure is more pronounced than the reduction of static pressure over this same distance because total pressure of the steam jet is lost during the shock-compression process that occurs in the under-expanded jet, and momentum is transferred from the primary jet to the secondary stream through the mixing process. There is a sudden pressure drop at 120 mm downstream for the pitot pressure in Figure 10 and the static pressure in Figure 8 but the feature does not appear in the computational simulations. The ideal gas calculation of pitot pressure using flow properties from the non-equilibrium wet steam CFD simulation predicts the values of the pitot pressure from the nozzle exit until a location 35 mm downstream reasonably well, but the calculation then overestimates the values during the shock process until the farthest measurement station downstream. The Rayleigh-pitot equation with an approximate equilibrium value for the specific heat ratio was used to calculate the pitot pressure from the computational simulation and this may be a factor that contributes to the discrepancy between the measurements and the simulations. The accuracy of the turbulence model used in this application is also uncertain. The fact that the static pressure passed below the triple point as discussed in section 4.1 is another important consideration that affects the accuracy of the simulation of the inviscid flow properties downstream of this region.

The equilibrium-composition pitot pressure profile determined from the CFD results closely follows the 'ideal gas, $\gamma = 1.12$ ' and both calculations show reasonable agreement with the experimental data from the nozzle tip until 35 mm downstream location. However, for locations further downstream, the frozen-composition calculation offers better agreement with the experimental data than the equilibrium calculation, but given the frozen-composition model is not reliable in the upstream regions, it cannot offer reliable insight to the flow physics downstream. The low flow speeds in the shock-compressed vapour adjacent to the pitot probe is the likely reason for the equilibrium-composition model performing reasonably in the vicinity of the nozzle exit.

4.3 Static pressure profiles at particular downstream locations

Figure 11 presents the static pressure profiles measured with the supersonic and subsonic static probes at particular downstream locations together with the comparison with the results derived from the non-equilibrium wet steam simulations. The supersonic static pressure probe was traversed in the test section in a vertical direction from 15 mm to -12 mm with respect to the nozzle centerline (0 mm radius), while the subsonic static pressure probe was traversed from 40 mm to 13 mm.

As it can be seen in Figure 11, the supersonic static pressure probe is able to define steam jet pressure variations at different downstream locations. The measurements of static pressure in the transverse direction presented in Figure 11 are consistent with those on the jet centerline presented in Figure 8.

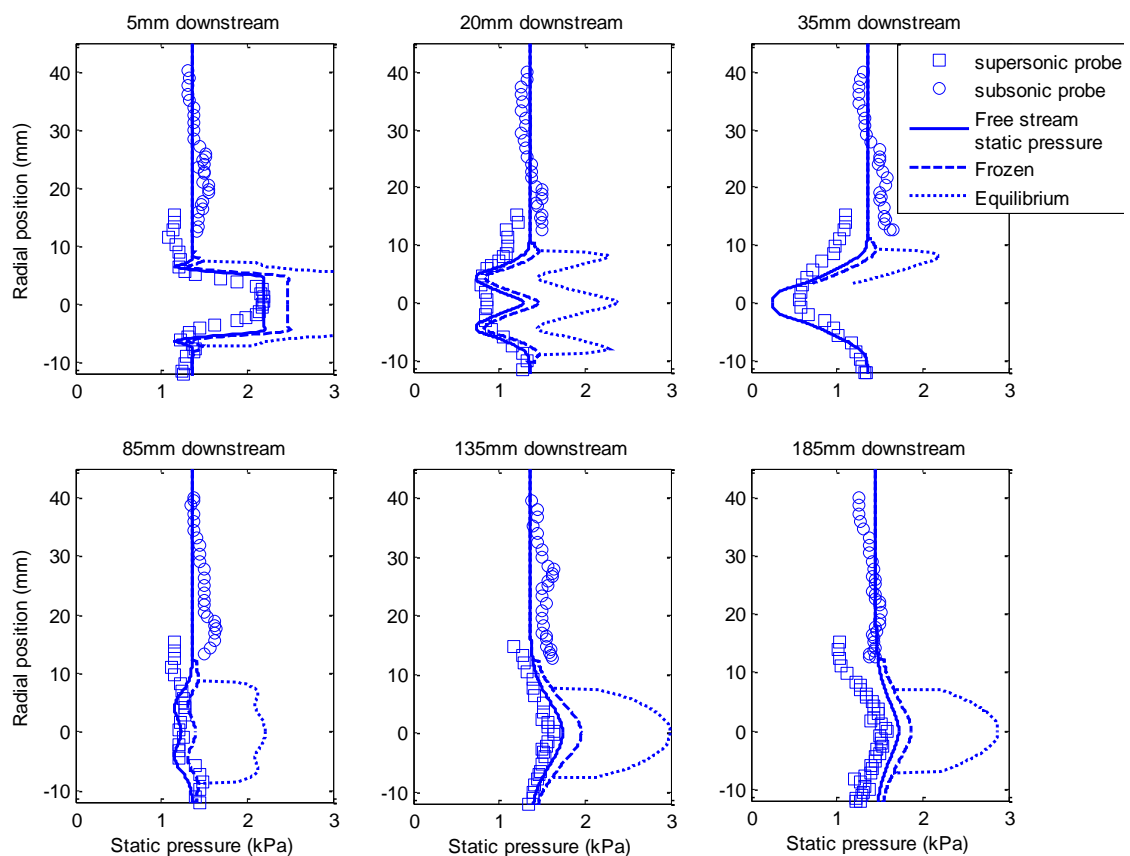


Figure 11. Static pressure profiles at different downstream locations

The subsonic static probe measured the static pressure for the subsonic part of the mixture in the test section which remained almost constant at 1.35 KPa for different downstream locations. The values of subsonic pressure in the test section, which was dependent to the background pressure in the condenser, increased slightly at each downstream location during the full traverse downwards. Each full traverse for the probes took around 16 minutes and during this period of time there was an increase in the condenser pressure.

There exists a region between 10 mm and 15 mm, where static pressure data is available from both the subsonic probe and the supersonic (conical) probe. In this overlapping region, the results from the conical probe are always lower than those from the subsonic probe. This is consistent with the fact that in this region of subsonic flow, the flow accelerates to negotiate a path around the conical probe and hence pressure are lower than measured by the subsonic static pressure probe.

Non-equilibrium CFD simulations for the static pressure (without any compression due to the conical shock) show a reasonable agreement with the experimental data: the trends and magnitudes for the simulated static pressure profiles closely approximate the experimental results. A particular exception however is for the locations of 20 and 35 mm downstream of the nozzle exit. These stations correspond to the location where the static pressure drops below the triple point value and this is likely to contribute to the differences between the simulations and the experimental data. The cone-static pressure profiles obtained from the frozen-composition calculation predict a close trend to the static pressure values directly from the CFD simulations, but there is a significant difference between the equilibrium-composition calculations and the experimental data as was discussed in section 4.1.

4.4 Pitot pressure profiles at particular downstream locations

Pitot pressure profiles at different downstream locations are presented in Figure 12. At each downstream location, the pitot probe was moved in the vertical direction from 25 mm to a downward position of -2 mm with respect to the nozzle centerline. It is clear that the value of pitot pressure for

the steam jet decreases from 26 kPa on the centerline at 5 mm downstream of the nozzle exit to a value of around 11 kPa at 185 mm downstream location. These results are consistent with the centerline measurements presented in Figure 10. The pitot pressure of the steam jet is reduced by supersonic expansion waves ahead of the probe because these waves accelerate the flow to a higher Mach number which increases the loss of total pressure through the normal shock on the pitot probe. The opposite effect occurs when an oblique shock is ahead of the probe.

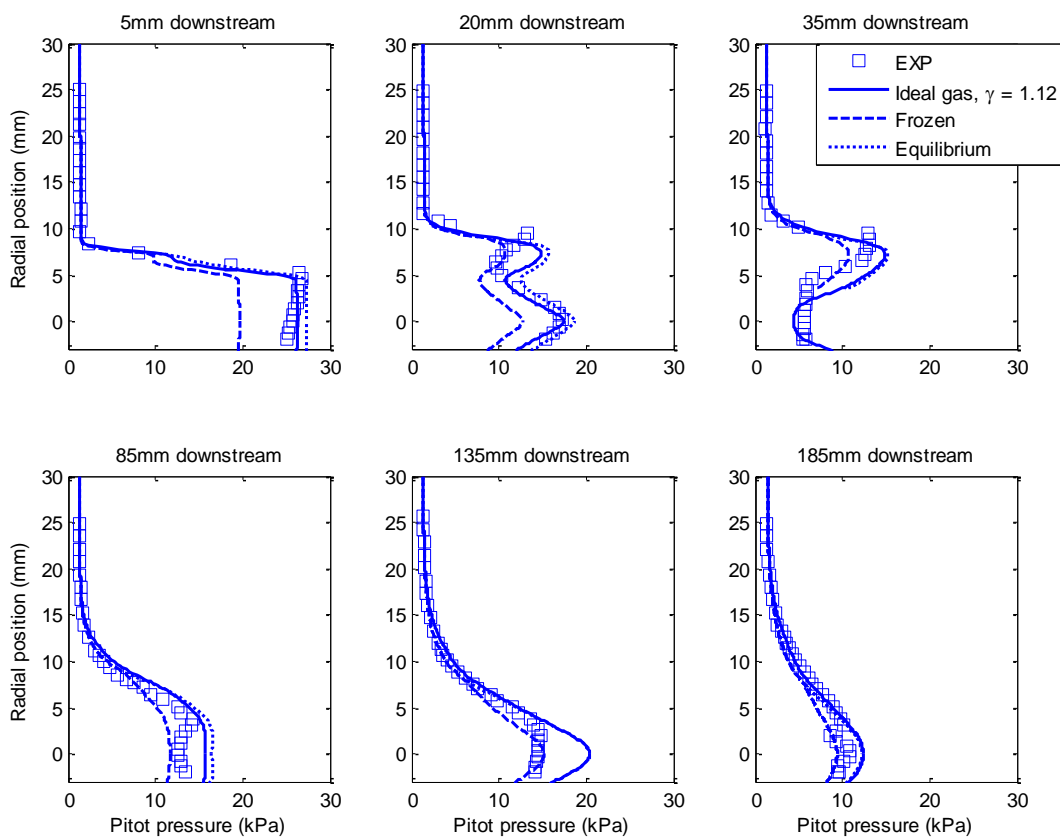


Figure 12. Pitot pressure profiles at different downstream locations

Pitot pressure in the steam jet at locations 20 and 35 mm downstream from the nozzle is strongly influenced by the supersonic wave processes associated with the under-expanded nature of the jet. Trends in the pitot pressure profiles at these stations are simulated with all 3 calculations based on the non-equilibrium wet steam CFD reasonably well, but the details and magnitudes of the

distributions differ from the experimental data. Again, the static pressure falling below the triple point is likely to cause inaccuracy in the calculations because no model for the liquid-to-solid and vapour-to-solid phase transitions has been included.

Pitot pressure profiles obtained from the CFD simulations show reasonable agreement with the experimental data for the outer regions of the jet (radius values greater than 5 mm) for locations 85, 135 and 185 mm downstream of the nozzle exit. However, for the inner region of the jet (radius values less than 5 mm), there are significant differences between the simulations and the experimental results. For radius values greater than 5 mm, turbulent mixing will strongly influence the development of the jet. But it is not possible to conclude that turbulent mixing is being simulated accurately in this case because the pitot pressure profiles are influenced by both pressure wave effects and mixing effects and clearly there are deficiencies in the simulation of the pressure wave effects.

Pitot profiles from the equilibrium-composition calculation are essentially the same as for the ideal gas, $\gamma = 1.12$ calculation for locations of 35mm, 135mm and 185mm and are in very close agreement for other downstream locations. The equilibrium-composition calculation is likely to provide a reasonable model for the pitot probe data as the flow is decelerated essentially to a low average flow speed ahead of the probe giving sufficient time for the composition of the flow to change to the equilibrium composition.

5. Conclusion

Uncertainties in the modelling of wet steam ejectors under conditions of compressible, turbulent flow with strong pressure gradients and condensation has stimulated the development of new experimental data for model development and validation work. A new experimental arrangement including a probe system and traversing mechanism was developed to measure the pitot and static pressures in a co-flowing steam jet at a condition relevant to steam ejector operation. The steam jet

with condensing conditions at approximately Mach 3.15 was generated downstream of a converging-diverging nozzle. A gearing system and DC motors were used to move the probes axially and transversely inside the test section.

A new set of experimental data was obtained from the pitot and static pressure probes to describe the steam jet behaviour in an under expanded condition, representative of steam ejector conditions. The experimental data indicates that the static pressure of steam which leaves the nozzle decreases to a minimum value through an expansion process and then increases with some fluctuations through induced oblique shock waves, typical of an under-expanded jet structure. The static pressures that develop immediately downstream of the nozzle exit are lower than the pressure of the triple point of water, so it is expected that transitions to ice will be induced.

Computational simulations using a non-equilibrium standard wet steam model and the $k - \omega$ SST turbulence model were performed to aid the interpretation of the steam jet structure and demonstrate the general suitability of the data for model development and validation. The simulation results, on the whole, showed a reasonable agreement with the experimental data, but differences in the vicinity of 25% were apparent at certain locations. An obvious area for improvement in the computational simulations is the development and inclusion of a model for the transitions to and from the solid phase which have not been included in the wet steam model that has been used in this work.

References

1. Ariafar, K., et al., *Mixing layer effects on the entrainment ratio in steam ejectors through ideal gas computational simulations*. Energy, 2016. **95**: p. 380-392.
2. Ariafar, K., et al., *Effect of mixing on the performance of wet steam ejectors*. Energy, 2015. **93**: p. 2030-2041.
3. Hemidi, A., et al., *CFD analysis of a supersonic air ejector. Part I: Experimental validation of single-phase and two-phase operation*. Applied Thermal Engineering, 2009. **29**(8): p. 1523-1531.
4. Bartosiewicz, Y., et al., *Numerical and experimental investigations on supersonic ejectors*. International Journal of Heat and Fluid Flow, 2005. **26**(1): p. 56-70.

5. Ruangtrakoon, N., et al., *CFD simulation on the effect of primary nozzle geometries for a steam ejector in refrigeration cycle*. International Journal of Thermal Sciences, 2013. **63**: p. 133-145.
6. Cutler, A.D., et al., *Supersonic coaxial jet experiment for computational fluid dynamics code validation*. AIAA journal, 2006. **44**(3): p. 585-592.
7. Clifton, C.W. and A.D. Cutler, *A Supersonic Argon/Air Coaxial Jet Experiment for Computational Fluid Dynamics Code Validation*. NASA/CR-2007-214866, NASA Langley Research Center, Hampton, Virginia, 2007.
8. Al-Doori, G. and D.R. Buttsworth, *Pitot pressure measurements in a supersonic steam jet*. Experimental Thermal and Fluid Science, 2014. **58**: p. 56-61.
9. Al-Doori, G.F.L., *Investigation of refrigeration system steam ejector performance through experiments and computational simulations*, 2013, University of Southern Queensland.
10. Balachandran, P., *Fundamentals of compressible fluid dynamics*. 2006: PHI Learning Pvt. Ltd.
11. Rathakrishnan, E., *Instrumentation, measurements, and experiments in fluids*. 2007: CRC Press.
12. Roshko, A. and H. Liepmann, *Elements of gas dynamics*, 1957, Wiley, New York.
13. Anderson, J.D., *Modern compressible flow: with historical perspective*. Vol. 12. 1990: McGraw-Hill New York.
14. Rathakrishnan, E., *Applied gas dynamics*. 2010: John Wiley & Sons.
15. Menter, F.R., *Two-equation eddy-viscosity turbulence models for engineering applications*. AIAA journal, 1994. **32**(8): p. 1598-1605.
16. *ANSYS-FLUENT 14.5 User's guide*.
17. Lin, C., et al., *Numerical investigation of geometry parameters for pressure recovery of an adjustable ejector in multi-evaporator refrigeration system*. Applied Thermal Engineering, 2013. **61**(2): p. 649-656.
18. Menter, F.R., *Zonal two equation k-turbulence models for aerodynamic flows*. AIAA paper, 1993. **2906**: p. 1993.
19. Ishazaki, K., T. Ikohagi, and H. Daiguji. *A high-resolution numerical method for transonic non-equilibrium condensation flows through a steam turbine cascade*. in *Proceedings of the 6th international symposium on computational fluid dynamics*. 1995.
20. Ariaifar, K., et al., *Ejector primary nozzle steam condensation: Area ratio effects and mixing layer development*. Applied Thermal Engineering, 2014. **71**(1): p. 519-527.
21. Anderson, J.D., *Modern compressible flow with historical perspective*. 2003.
22. Massey, B.S., A.J. Ward-Smith, and A. John, *Mechanics of fluids*. Vol. 45. 1989: Springer.
23. Guha, A., *A unified theory for the interpretation of total pressure and temperature in two-phase flows at subsonic and supersonic speeds*. Proceedings of the Royal Society of London. Series A: Mathematical, Physical and Engineering Sciences, 1998. **454**(1970): p. 671-695.

Chapter 7 Conclusions

7.1 Summary

Supersonic steam ejectors are widely used in a large number of industries that use steam as a heating or a power-generating medium. Ejectors are devices which utilize the energy of a high pressure fluid (the primary stream) to move a low pressure fluid (the secondary stream) and enable it to be compressed to a higher pressure. Their action is similar to a vacuum pump or compressor but ejectors do not use any moving components or electricity for the compression process. They are known for simple construction, easy installation and low capital costs.

The entrainment ratio (ER) is one of the important parameters which is used to quantify the amount of low pressure steam that can be recovered and compressed to a higher pressure. The entrainment ratio is a direct measurement of the energy efficiency of steam ejectors. In broad terms, the higher the ER for steam ejectors, the larger the quantity of low pressure steam that can be recovered, so having a high ER is an advantage for industrial applications. The mixing between the primary and secondary streams affects the ER and is influenced by the condensation of steam in the primary nozzle which has a significant influence on the steam properties at the end of the primary nozzle. In this study, condensation and mixing effects in steam ejectors were investigated by experiment and computational simulation. The study was conducted in four phases in order to:

1. Describe the effect of steam condensation on flow properties at the primary nozzle exit and identify how these properties affect the mixing layer growth rate;
2. Probe the origins of the effects of steam condensation on the ejector performance;
3. Examine the effect of the mixing layer development on the ejector entrainment ratio; and
4. Provide detailed measurement of steam mixing in a co-flowing steam jet suitable for validation of steam ejector modelling.

7.2 Effect of steam condensation on flow characteristics in the primary nozzle and mixing process

Condensation within steam ejectors is initiated within the primary nozzle and has a profound effect on the flow conditions downstream. A computational simulation study using the wet steam and ideal gas models was performed for the primary nozzle of a particular steam ejector to investigate the effect of condensation on steam jet properties and mixing layer growth rate. The following conclusions were made based on the simulation results.

- After the initiation of condensation, higher nozzle static pressures and temperatures resulted for the wet steam model than in the case of the ideal gas model.
- Lower Mach numbers were observed in the case of the wet steam model.
- There was no significant difference in the momentum flux profile when using ideal gas and wet steam models.
- The increased speed of sound in primary stream due to the release of latent heat in the condensation process reduces compressibility effects in the mixing layer leading to an augmented mixing rate relative to the ideal gas case.
- For a particular primary nozzle and operating condition, the difference in the mixing layer growth rates between the ideal gas and wet steam models was 29%, indicating a faster growth rate of the mixing layer for the wet steam model.

7.3 Effects of steam condensation on the ejector performance

A complete steam ejector was selected as a case study for computational simulation using both ideal gas and wet steam assumptions. From the simulation results, the following conclusions were drawn.

- A higher entrainment ratio and critical back pressure was achieved for wet steam simulation than in the case of an ideal gas model.

- Flow conditions generated by the primary nozzle which are affected by the steam condensation altered the flow conditions relative to the ideal gas case and these altered conditions affect the mixing process of the primary and secondary streams which is initiated at the primary nozzle exit.
- Increased mixing of the primary and secondary streams occurs in the wet steam case and this was the reason for the higher entrainment ratio.
- A higher value for the pitot pressure of the mixture at the entrance of the ejector diffuser was identified as the reason for the higher critical back pressure for the wet steam simulation relative to the ideal gas simulation.

7.4 Effect of mixing layer development of the ejector entrainment ratio

The ejector entrainment ratio is primarily influenced by two factors: pressure-driven effects and mixing-driven effects. Computational simulations based on inviscid and viscous solvers were performed to specify the influence of these two factors on the entrainment ratio under some typical operating conditions for a steam ejector. Simulation results for the entrainment ratio based on the inviscid solver were used to determine the entrainment ratio due to the pressure driven effects. The increase in entrainment ratio achieved with the viscous simulation results was then used to identify the portion of the entrainment ratio associated with mixing effects. The following conclusions were drawn.

- Ejector entrainment ratio increases by a decrease in the mixing layer compressibility effects and an increase of the mixing layer growth rate.
- For fixed operating conditions for the primary and discharge streams, the ejector entrainment ratio is increasingly influenced by the pressure driven effects and mixing effects become less significant.
- Under a fixed operating conditions for the primary and discharge streams, about 35% of the entrainment ratio is due to the mixing effects for the secondary stream stagnation conditions

of 0.94 kPa and 279 K, but this portion is reduced to about 22% when the secondary stream stagnation conditions are 2.65 kPa and 295 K.

- The portion of ejector entrainment ratio attributable to mixing effects was correlated with the rate of compressible mixing layer growth.

7.5 Measurement of steam mixing in a co-flowing steam jet

The pitot and static pressures of a high pressure supersonic steam jet which expanded through a converging diverging nozzle and mixed with a low pressure co-flowing stream was measured to provide direct data on the mixing of wet steam jets in ejectors. Measurements were performed along the mixing jet centreline from the nozzle tip until a downstream location of 185 mm in the mixing chamber. Radial profiles of pitot and static pressure were also measured at positions of 5, 20, 35, 85, 135 and 185 mm downstream of the nozzle exit. Computational simulations were also performed using the $k - \omega$ SST turbulence model for validation of simulation results. Based on the experimental data and computational results, following conclusion were made.

- The static pressure of steam which leaves the nozzle decreases to a minimum value through an expansion process and then increases with some fluctuations through induced oblique shock waves, indicating a typical of an under-expanded jet structure.
- The static pressures that develop immediately downstream of the nozzle exit are lower than the pressure of the triple point of water, so it is expected that transitions to ice will be induced.
- The simulation results, on the whole, showed a reasonable agreement with the experimental data, but differences of about 25% were apparent at specific locations.
- An improvement for the wet steam model in computational simulation is required to include the transitions to and from the solid phase.

7.6 Areas for Future Research

Research was performed using computational simulation to investigate the effects of steam condensation on the mixing process and the performance of steam ejectors. The pitot and static pressures of a wet steam jet were also measured using a new apparatus to provide data on the wet steam mixing process suitable for model development and validation of simulations. However, further computational and experimental work is required to improve modelling and simulation capabilities.

The following recommendations for future investigations are made:

- Improvement of the wet steam model to include the transitions to and from the solid phase for cases in which the steam pressure is lower than the triple point of water.
- Measurement of condensing steam pressure and temperature along the centreline of a converging diverging nozzle.
- Measurement of high pressure steam jet properties downstream of a converging diverging nozzle using laser diagnostic techniques.

References

1. ESDU, E., *jet pump, data item 86030*. ESDU International Ltd., London, 1985.
2. Grazzini, G. and A. Rocchetti, *Influence of the objective function on the optimisation of a steam ejector cycle*. international journal of refrigeration, 2008. **31**(3): p. 510-515.
3. Chen, Y.-M. and C.-Y. Sun, *Experimental study of the performance characteristics of a steam-ejector refrigeration system*. Experimental Thermal and Fluid Science, 1997. **15**(4): p. 384-394.
4. ASHRAE, G. and D. Book, *Steam Jet Refrigeration Equipment*. Chap, 1967. **12**: p. 133-138.
5. Keenan, J. and E. Neumann, *A simple air ejector*. ASME Journal of Applied Mechanics, 1942. **64**: p. 75-82.
6. Eames, I., S. Aphornratana, and H. Haider, *A theoretical and experimental study of a small-scale steam jet refrigerator*. International Journal of Refrigeration, 1995. **18**(6): p. 378-386.
7. Eames, I.W., *A new prescription for the design of supersonic jet-pumps: the constant rate of momentum change method*. Applied thermal engineering, 2002. **22**(2): p. 121-131.
8. DeFrate, L. and A. Hoerl. *Optimum design of ejectors using digital computers*. in *Chem. Eng. Prog. Symp. Series*. 1959.
9. Munday, J.T. and D.F. Bagster, *A new ejector theory applied to steam jet refrigeration*. Industrial & Engineering Chemistry Process Design and Development, 1977. **16**(4): p. 442-449.
10. Huang, B., et al., *A 1-D analysis of ejector performance*. International Journal of Refrigeration, 1999. **22**(5): p. 354-364.
11. Zhu, Y., et al., *Shock circle model for ejector performance evaluation*. Energy Conversion and Management, 2007. **48**(9): p. 2533-2541.
12. Sherif, S., et al., *Analysis and modeling of a two-phase jet pump of a thermal management system for aerospace applications*. International journal of mechanical sciences, 2000. **42**(2): p. 185-198.
13. Cizungu, K., A. Mani, and M. Groll, *Performance comparison of vapour jet refrigeration system with environment friendly working fluids*. Applied Thermal Engineering, 2001. **21**(5): p. 585-598.
14. Aidoun, Z. and M. Ouzzane, *The effect of operating conditions on the performance of a supersonic ejector for refrigeration*. International Journal of Refrigeration, 2004. **27**(8): p. 974-984.
15. Selvaraju, A. and A. Mani, *Analysis of a vapour ejector refrigeration system with environment friendly refrigerants*. International Journal of Thermal Sciences, 2004. **43**(9): p. 915-921.
16. Yapıcı, R. and H. Ersoy, *Performance characteristics of the ejector refrigeration system based on the constant area ejector flow model*. Energy Conversion and Management, 2005. **46**(18): p. 3117-3135.
17. Sun, D.W. and I.W. Eames, *Performance characteristics of HCFC-123 ejector refrigeration cycles*. International Journal of Energy Research, 1996. **20**(10): p. 871-885.
18. Chou, S., P. Yang, and C. Yap, *Maximum mass flow ratio due to secondary flow choking in an ejector refrigeration system*. International journal of refrigeration, 2001. **24**(6): p. 486-499.
19. Ma, X., et al., *Experimental investigation of a novel steam ejector refrigerator suitable for solar energy applications*. Applied Thermal Engineering, 2010. **30**(11): p. 1320-1325.
20. Sriveerakul, T., S. Aphornratana, and K. Chunnanond, *Performance prediction of steam ejector using computational fluid dynamics: Part 1. Validation of the CFD results*. International Journal of Thermal Sciences, 2007. **46**(8): p. 812-822.
21. Sun, D.-W., *Experimental investigation of the performance characteristics of a steam jet refrigeration system*. Energy Sources, 1997. **19**(4): p. 349-367.
22. Chunnanond, K. and S. Aphornratana, *An experimental investigation of a steam ejector refrigerator: the analysis of the pressure profile along the ejector*. Applied Thermal Engineering, 2004. **24**(2): p. 311-322.

23. Bartosiewicz, Y., et al., *Numerical and experimental investigations on supersonic ejectors*. International Journal of Heat and Fluid Flow, 2005. **26**(1): p. 56-70.
24. Yapıcı, R. and C. Yetişen, *Experimental study on ejector refrigeration system powered by low grade heat*. Energy Conversion and Management, 2007. **48**(5): p. 1560-1568.
25. Sankarlal, T. and A. Mani, *Experimental investigations on ejector refrigeration system with ammonia*. Renewable Energy, 2007. **32**(8): p. 1403-1413.
26. Chen, S.-L., J.-Y. Yen, and M.-C. Huang, *An experimental investigation of ejector performance based upon different refrigerants*, 1998, American Society of Heating, Refrigerating and Air-Conditioning Engineers, Inc., Atlanta, GA (United States).
27. Pounds, D.A., et al., *Experimental investigation and theoretical analysis of an ejector refrigeration system*. International Journal of Thermal Sciences, 2013. **67**: p. 200-209.
28. Ruangtrakoon, N., S. Aphornratana, and T. Sriveerakul, *Experimental studies of a steam jet refrigeration cycle: Effect of the primary nozzle geometries to system performance*. Experimental Thermal and Fluid Science, 2011. **35**(4): p. 676-683.
29. Chang, Y.-J. and Y.-M. Chen, *Enhancement of a steam-jet refrigerator using a novel application of the petal nozzle*. Experimental Thermal and Fluid Science, 2000. **22**(3): p. 203-211.
30. Chaiwongsa, P. and S. Wongwises, *Experimental study on R-134a refrigeration system using a two-phase ejector as an expansion device*. Applied Thermal Engineering, 2008. **28**(5): p. 467-477.
31. Dong, J., et al., *An experimental investigation of steam ejector refrigeration systems*. Journal of Thermal Science and Engineering Applications, 2012. **4**(3): p. 031004.
32. Eames, I.W., A.E. Ablwaifa, and V. Petrenko, *Results of an experimental study of an advanced jet-pump refrigerator operating with R245fa*. Applied Thermal Engineering, 2007. **27**(17): p. 2833-2840.
33. Yapıcı, R., *Experimental investigation of performance of vapor ejector refrigeration system using refrigerant R123*. Energy Conversion and Management, 2008. **49**(5): p. 953-961.
34. Yapıcı, R., et al., *Experimental determination of the optimum performance of ejector refrigeration system depending on ejector area ratio*. International journal of refrigeration, 2008. **31**(7): p. 1183-1189.
35. Varga, S., et al., *Experimental and numerical analysis of a variable area ratio steam ejector*. international journal of refrigeration, 2011. **34**(7): p. 1668-1675.
36. Aphornratana, S., S. Chungpaibulpatana, and P. Srihirin, *Experimental investigation of an ejector refrigerator: effect of mixing chamber geometry on system performance*. International journal of energy research, 2001. **25**(5): p. 397-411.
37. Shah, A., I.R. Chughtai, and M.H. Inayat, *Experimental study of the characteristics of steam jet pump and effect of mixing section length on direct-contact condensation*. International Journal of Heat and Mass Transfer, 2013. **58**(1): p. 62-69.
38. Ouzzane, M. and Z. Aidoun, *Model development and numerical procedure for detailed ejector analysis and design*. Applied Thermal Engineering, 2003. **23**(18): p. 2337-2351.
39. Bartosiewicz, Y., Z. Aidoun, and Y. Mercadier, *Numerical assessment of ejector operation for refrigeration applications based on CFD*. Applied Thermal Engineering, 2006. **26**(5): p. 604-612.
40. Sriveerakul, T., S. Aphornratana, and K. Chunnanond, *Performance prediction of steam ejector using computational fluid dynamics: Part 2. Flow structure of a steam ejector influenced by operating pressures and geometries*. International Journal of Thermal Sciences, 2007. **46**(8): p. 823-833.
41. Pianthong, K., et al., *Investigation and improvement of ejector refrigeration system using computational fluid dynamics technique*. Energy Conversion and Management, 2007. **48**(9): p. 2556-2564.

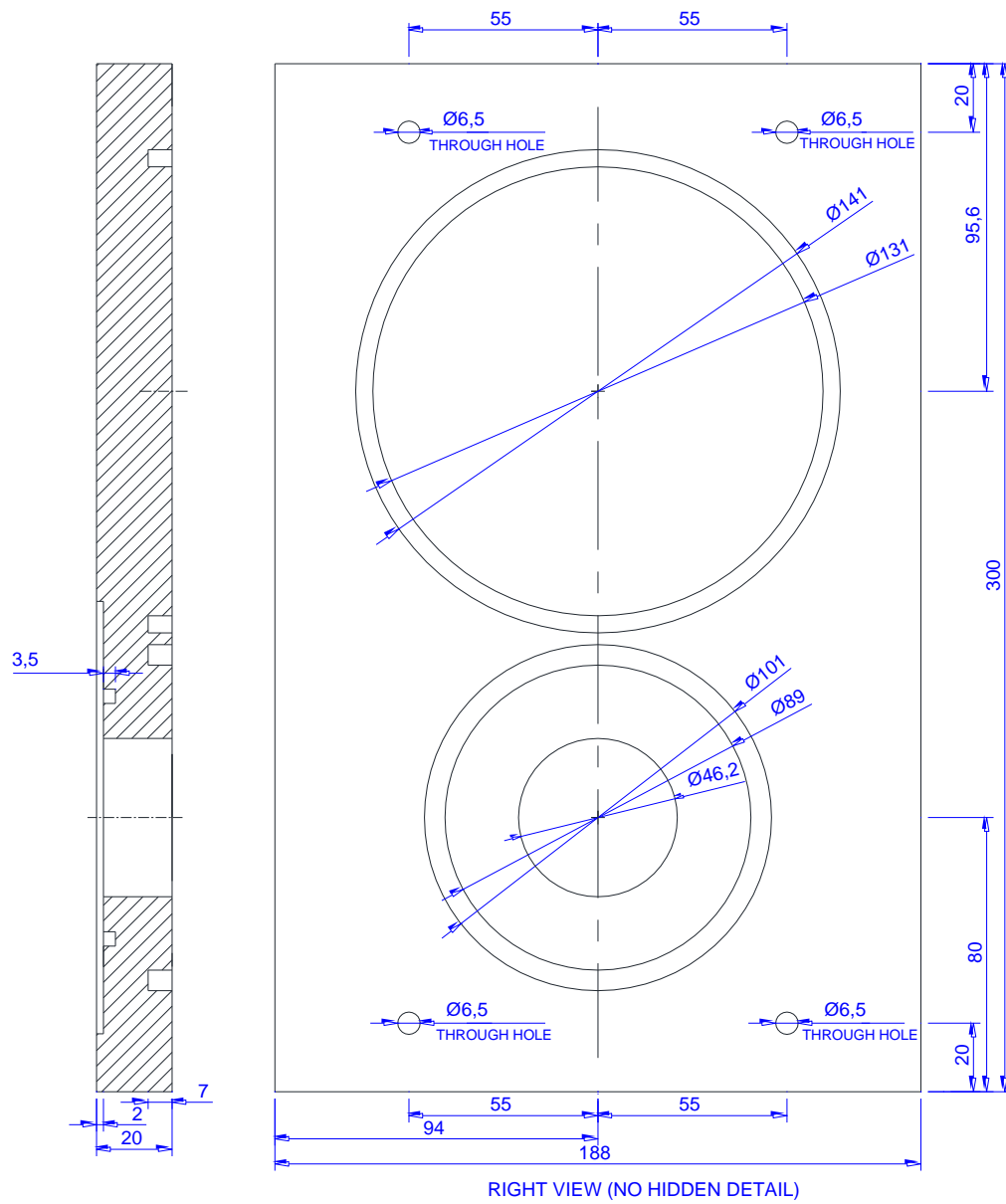
42. Hemidi, A., et al., *CFD analysis of a supersonic air ejector. Part I: Experimental validation of single-phase and two-phase operation*. Applied Thermal Engineering, 2009. **29**(8): p. 1523-1531.
43. Wang, X.-D. and J.-L. Dong, *Numerical study on the performances of steam-jet vacuum pump at different operating conditions*. Vacuum, 2010. **84**(11): p. 1341-1346.
44. Sharifi, N. and M. Boroomand, *An investigation of thermo-compressor design by analysis and experiment: Part 1. Validation of the numerical method*. Energy Conversion and Management, 2013. **69**: p. 217-227.
45. Riffat, S. and S. Omer, *CFD modelling and experimental investigation of an ejector refrigeration system using methanol as the working fluid*. International Journal of Energy Research, 2001. **25**(2): p. 115-128.
46. Rusly, E., et al., *CFD analysis of ejector in a combined ejector cooling system*. International Journal of Refrigeration, 2005. **28**(7): p. 1092-1101.
47. Zhu, Y., et al., *Numerical investigation of geometry parameters for design of high performance ejectors*. Applied Thermal Engineering, 2009. **29**(5): p. 898-905.
48. Varga, S., A.C. Oliveira, and B. Diaconu, *Influence of geometrical factors on steam ejector performance—a numerical assessment*. International journal of refrigeration, 2009. **32**(7): p. 1694-1701.
49. Varga, S., A.C. Oliveira, and B. Diaconu, *Numerical assessment of steam ejector efficiencies using CFD*. international journal of refrigeration, 2009. **32**(6): p. 1203-1211.
50. Ji, M., et al., *CFD investigation on the flow structure inside thermo vapor compressor*. Energy, 2010. **35**(6): p. 2694-2702.
51. Opgenorth, M.J., et al., *Maximizing pressure recovery using lobed nozzles in a supersonic ejector*. Applied Thermal Engineering, 2012. **37**: p. 396-402.
52. Yang, X., X. Long, and X. Yao, *Numerical investigation on the mixing process in a steam ejector with different nozzle structures*. International Journal of Thermal Sciences, 2012. **56**: p. 95-106.
53. Ruangtrakoon, N., et al., *CFD simulation on the effect of primary nozzle geometries for a steam ejector in refrigeration cycle*. International Journal of Thermal Sciences, 2013. **63**: p. 133-145.
54. Lin, C., et al., *Numerical investigation of geometry parameters for pressure recovery of an adjustable ejector in multi-evaporator refrigeration system*. Applied Thermal Engineering, 2013. **61**(2): p. 649-656.
55. Yang, Y. and S. Shen, *Numerical simulation on non-equilibrium spontaneous condensation in supersonic steam flow*. International communications in heat and mass transfer, 2009. **36**(9): p. 902-907.
56. Wang, X.-D., et al., *Numerical analysis of spontaneously condensing phenomena in nozzle of steam-jet vacuum pump*. Vacuum, 2012. **86**(7): p. 861-866.
57. Grazzini, G., A. Milazzo, and S. Piazzini, *Prediction of condensation in steam ejector for a refrigeration system*. International Journal of Refrigeration, 2011. **34**(7): p. 1641-1648.
58. Sharifi, N., M. Boroomand, and R. Kouhikamali, *Wet steam flow energy analysis within thermo-compressors*. Energy, 2012. **47**(1): p. 609-619.
59. Sharifi, N., M. Boroomand, and M. Sharifi, *Numerical assessment of steam nucleation on thermodynamic performance of steam ejectors*. Applied Thermal Engineering, 2013. **52**(2): p. 449-459.
60. Wang, X.-D., et al., *The spontaneously condensing phenomena in a steam-jet pump and its influence on the numerical simulation accuracy*. International Journal of Heat and Mass Transfer, 2012. **55**(17): p. 4682-4687.
61. Zheng, H., et al., *Computational fluid dynamics simulation of the supersonic steam ejector. Part 1: Comparative study of different equations of state*. Proceedings of the Institution of Mechanical Engineers, Part C: Journal of Mechanical Engineering Science, 2012. **226**(3): p. 709-714.

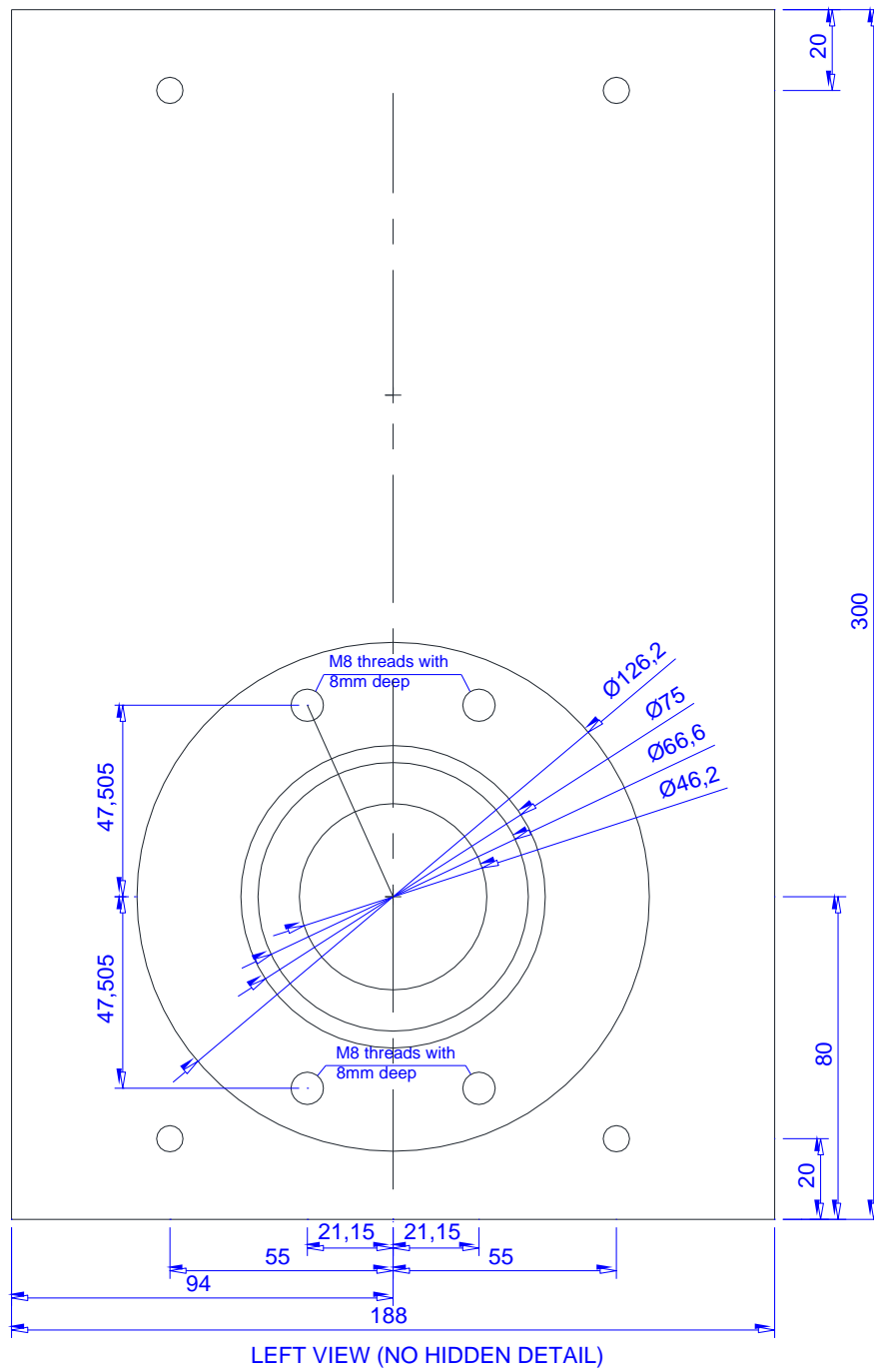
62. Cai, L. and M. He, *A numerical study on the supersonic steam ejector use in steam turbine system*. Mathematical Problems in Engineering, 2013. **2013**.
63. Wang, X., et al., *Numerical study of primary steam superheating effects on steam ejector flow and its pumping performance*. Energy, 2014. **78**: p. 205-211.
64. Moore, M., et al., *Predicting the fog drop size in wet steam turbines*. Wet steam, 1973. **4**: p. 101-109.
65. Bakhtar, F. and K. Zidi, *Nucleation phenomena in flowing high-pressure steam: experimental results*. Proceedings of the Institution of Mechanical Engineers, Part A: Journal of Power and Energy, 1989. **203**(3): p. 195-200.
66. Bakhtar, F. and K. Zidi, *Nucleation phenomena in flowing high-pressure steam Part 2: Theoretical analysis*. Proceedings of the Institution of Mechanical Engineers, Part A: Journal of Power and Energy, 1990. **204**(4): p. 233-242.
67. Young, J., *Spontaneous condensation of steam in supersonic nozzles*. Physicochemical Hydrodynamics (PCH), 1982. **3**: p. 57-82.
68. Young, J., *An equation of state for steam for turbomachinery and other flow calculations*. Journal of Engineering for Gas Turbines and Power, 1988. **110**(1): p. 1-7.
69. Young, J., *The fundamental equations of gas-droplet multiphase flow*. International journal of multiphase flow, 1995. **21**(2): p. 175-191.
70. Young, J., *Two-dimensional, nonequilibrium, wet-steam calculations for nozzles and turbine cascades*. Journal of Turbomachinery, 1992. **114**(3): p. 569-579.
71. Bakhtar, F. and M.M. Tochai, *An investigation of two-dimensional flows of nucleating and wet steam by the time-marching method*. International Journal of Heat and Fluid Flow, 1980. **2**(1): p. 5-18.
72. White, A. and J. Young, *Time-marching method for the prediction of two-dimensional, unsteadyflows of condensing steam*. Journal of Propulsion and Power, 1993. **9**(4): p. 579-587.
73. Gerber, A., *Two-phase Eulerian/Lagrangian model for nucleating steam flow*. Journal of Fluids Engineering, 2002. **124**(2): p. 465-475.
74. Kermani, M. and A. Gerber, *A general formula for the evaluation of thermodynamic and aerodynamic losses in nucleating steam flow*. International journal of heat and mass transfer, 2003. **46**(17): p. 3265-3278.
75. Moore, M.J. and C. Sieverding, *Two-phase steam flow in turbines and separators: theory, instrumentation, engineering*. 1976.
76. Yamamoto, S., et al. *Numerical and experimental investigations of unsteady 3-D wet-steam flows through two-stage stator-rotor cascade channels*. in *ASME Turbo Expo 2010: Power for Land, Sea, and Air*. 2010. American Society of Mechanical Engineers.
77. Yamamoto, S., et al. *Parallel computation of condensate flows through 2-d and 3-d multistage turbine cascades*. in *Proc. International Gas Turbine Congress*. 2007.
78. Yamamoto, S., et al. *Parallel-implicit computation of three-dimensional multistage stator-rotor cascade flows with condensation*. in *18th AIAA Computational Fluid Dynamics Conference*. 2007.
79. Starzmann, J., et al. *On kinematic relaxation and deposition of water droplets in the last stages of low pressure steam turbines*. in *ASME Turbo Expo 2013: Turbine Technical Conference and Exposition*. 2013. American Society of Mechanical Engineers.
80. Starzmann, J.r., et al. *Modelling and validation of wet steam flow in a low pressure steam turbine*. in *ASME 2011 Turbo Expo: Turbine Technical Conference and Exposition*. 2011. American Society of Mechanical Engineers.
81. Brown, G.L. and A. Roshko, *On density effects and large structure in turbulent mixing layers*. Journal of Fluid Mechanics, 1974. **64**(04): p. 775-816.
82. Dimotakis, P.E., *Two-dimensional shear-layer entrainment*. AIAA journal, 1986. **24**(11): p. 1791-1796.

83. Dimotakis, P., *Turbulent free shear layer mixing and combustion*. High Speed Flight Propulsion Systems, 1991. **137**: p. 383-455.
84. Bogdanoff, D., *Compressibility effects in turbulent shear layers*. AIAA journal, 1983. **21**(6): p. 926-927.
85. Papamoschou, D. and A. Roshko, *The compressible turbulent shear layer: an experimental study*. Journal of Fluid Mechanics, 1988. **197**: p. 453-477.
86. Elliott, G. and M. Samimy, *Compressibility effects in free shear layers*. Physics of Fluids A: Fluid Dynamics (1989-1993), 1990. **2**(7): p. 1231-1240.
87. Samimy, M. and G. Elliott, *Effects of compressibility on the characteristics of free shear layers*. AIAA journal, 1990. **28**(3): p. 439-445.
88. Slessor, M., M. Zhuang, and P. Dimotakis, *Turbulent shear-layer mixing: growth-rate compressibility scaling*. Journal of Fluid Mechanics, 2000. **414**: p. 35-45.
89. Cutler, A. and J. White, *An experimental and CFD study of a supersonic coaxial jet*. 2001.
90. Cutler, A., et al., *Supersonic coaxial jet experiment for CFD code validation*. 1999.
91. Cutler, A.D., et al., *Supersonic coaxial jet experiment for computational fluid dynamics code validation*. AIAA journal, 2006. **44**(3): p. 585-592.
92. Clifton, C.W. and A.D. Cutler, *A Supersonic Argon/Air Coaxial Jet Experiment for Computational Fluid Dynamics Code Validation*. 2007.
93. Al-Doori, G. and D.R. Buttsworth, *Pitot pressure measurements in a supersonic steam jet*. Experimental Thermal and Fluid Science, 2014. **58**: p. 56-61.

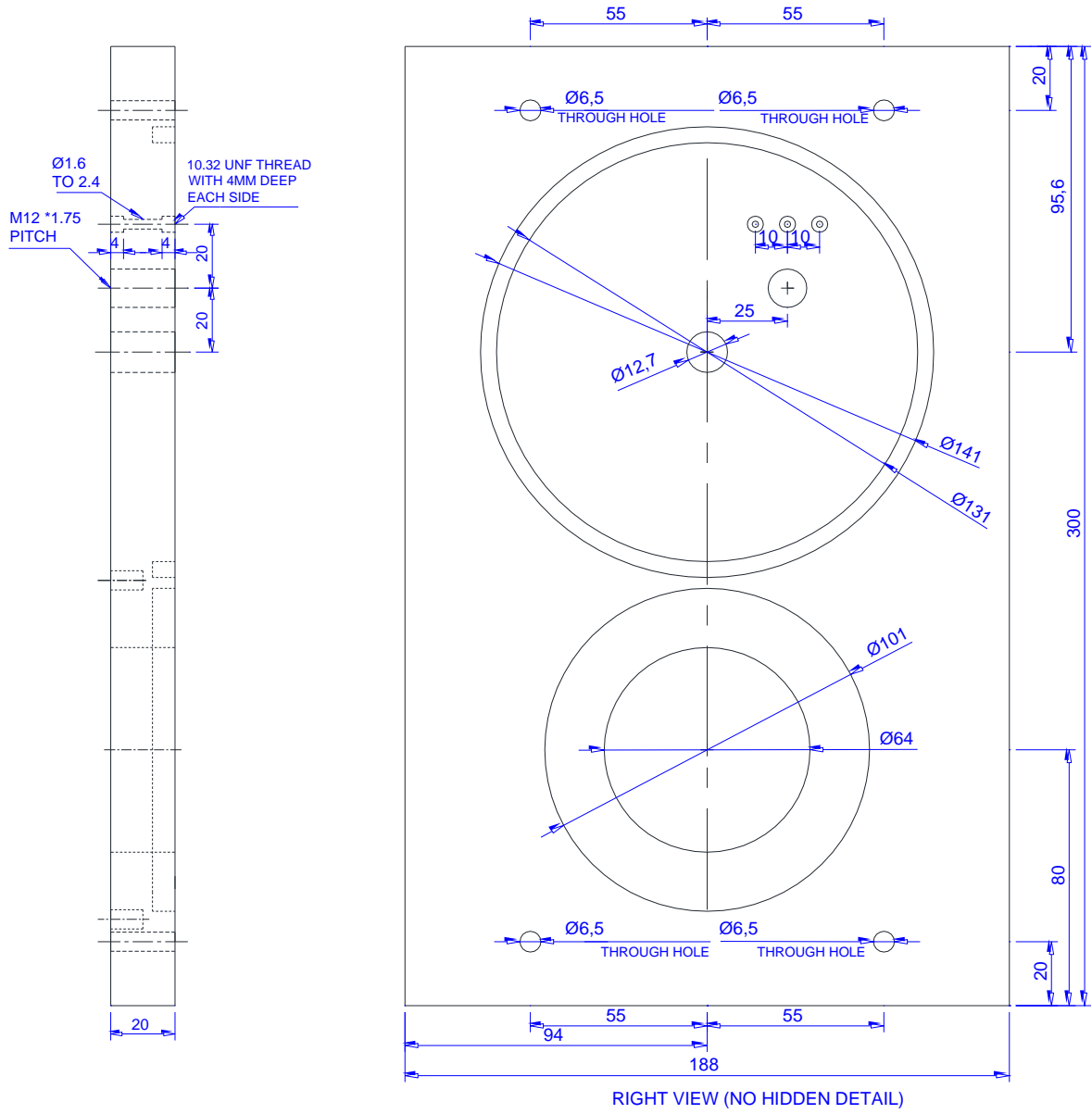
Appendix A

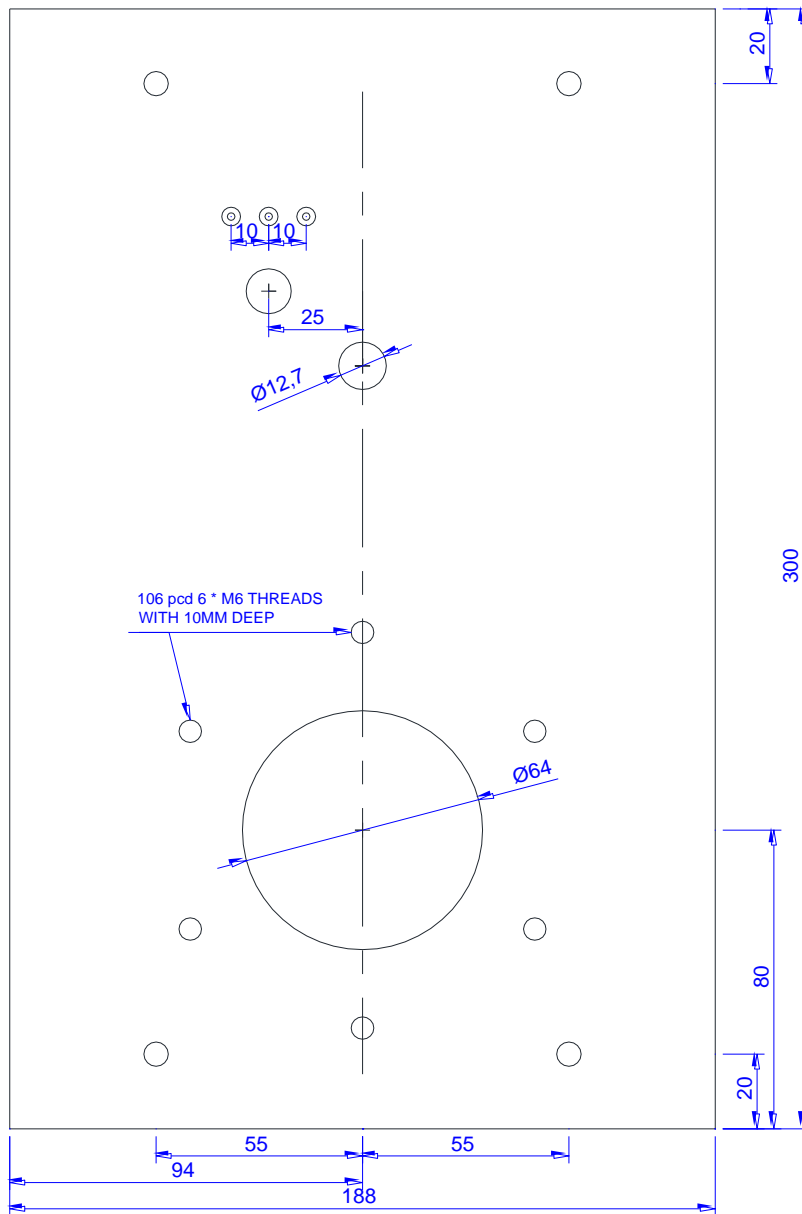
A.1 Nozzle end plate





A.2 Exit end plate





LEFT VIEW (NO HIDDEN DETAIL)

A.3 Probes system

